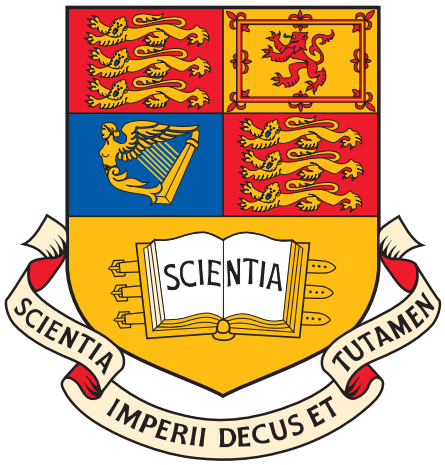
Imperial College London

Generation and Application of Ultrashort Laser Pulses in Attosecond Science

Felix Frank

May 2011



Thesis submitted in partial fulfilment of the requirements for the degree of

Doctor of Philosophy of Imperial College London

Laser Consortium

Quantum Optics and Laser Science Group

Physics Department

Imperial College London

Prince Consort Road, London SW7 2AZ

United Kingdom

Declaration

I declare that the work contained within this thesis is my own unless stated otherwise.

.....

Felix Frank

Abstract

In this thesis, I describe the development of a sub-4 fs few-cycle laser system at Imperial College London used to generate and characterise the first single attosecond (1 as = 10^{-18} s) pulses in the UK.

Phase-stabilised few-cycle laser pulses were generated using a hollow fibre system with a chirped mirror compression setup. The pulse was fully characterised using frequency-resolved optical gating (FROG) and spectral phase interferometry for direct electric field reconstruction in a spatially encoded filter arrangement (SEA-F-SPIDER). A pulse duration of 3.5 fs was measured with an argon filled hollow fibre.

These phase stabilised Infra-Red (IR) pulses were used to generate a continuous spectrum of high harmonics in the Extreme Ultraviolet (XUV) originating from a single half-cycle of the driving field. Using subsequent spectral filtering, a single attosecond pulse was generated. The isolated XUV pulse was characterised using an atomic streaking camera and a pulse duration of ~ 260 as was retrieved using FROG for complete reconstruction of attosecond bursts (FROG-CRAB).

In an experiment conducted at the Rutherford Appleton Laboratory, high harmonics were generated using a two-colour field with an energetic beam at 1300 nm and a weak second harmonic orthogonally polarized to the fundamental. By changing the phase between the two fields, a deep modulation of the harmonic yield is seen and an enhancement of one order of magnitude compared to the single colour field with the same energy is observed.

Acknowledgements

Firstly I have to thank the whole Laser Consortium for being the best and most welcoming group. This made my PhD the great experience it was (if we forget about the Monday morning meetings).

I have to thank John for giving me the opportunity to work with all the attoboys. John is a great supervisor that was always there to support me, has great patience and, at some point, will run the Hyde Park relay in under 20 minutes. I also thank Jon and Roland for giving me advice on physics and cooling chambers, respectively.

As mentioned above, I couldn't have done my PhD without the attoboys. In the last three years Chris has become one of my best friends in- and outside the lab. He taught me how to dance, collect 27 packs of sweets on an airplane, introduced me to a plethora of pranks and sometimes I even wear odd socks. Tobi who has brought Matlab and a new sense of fashion to our group was always there to talk about Fourier transforms and help out with all sorts of things. Jarlath, showed me the Irish efficiency both in the lab and in personal water consumption. And William, the newest addition to the lab, for becoming a true attoboy in such a short time.

I was also lucky to start with the best year of PhD students. Thank you Hugo, for just being great and for never saying no to a bottle of rosé; Leo for good times aligning irises at RAL; Ryan for letting me wear his Gretzky jersey and setting new haircut standards. David (and his Bristol No.1) for sharing your love of real ale and Eva for telling me how to get pregnant faster. Thank you.

I also thank Tom not only for getting everybody involved in social outings but also for always being helpful in the lab. Malte for reminding me of the

existence of great things outside of laser-physics. Amelle for drinking my Tequilas. Ann for being a girl and all the rest of the new (Marco, Richard, Henry, Sid, Stefan[i]) and really new guys (The Uzbek guy, Seb and Leon, Pricey, Nargis, Damien, Simon) that float around and make our tea breaks more interesting.

And let's not forget the old bunch that welcomed me to the group, when I started my PhD. Joe introduced me to the laser and fingertip-free alignment procedures before he abandoned all of us to dig for gold out west. Phil for showing me Opal and being a great friend. Hank for loving computers. Sarah for sharing all the little tricks she had learnt in a decade at the Consortium and Delphine for her violent hugs.

I also thank Peter and Andy for using every dirty scribbling we gave them as a detailed technical drawing. Thank you Bandu for always taking your time to explain and sort out our electronics.

And of course I have to thank my Family -Mama, Laura, Filipp- who supported me all my life. Last but not least, Katharina. She was the one that had to wait for dinner when the laser lab was flooded or the CEP was finally working. Thank you for always being there for me and putting up with all the late nights and work related grumpiness.

Don't forget to read the rest of the thesis, too.

[i] I will think of you many times in the future

Streaking *is the act of running nude through a public place. It is a light-hearted form of exhibitionism and public nudity not intended to shock but, rather, to amuse onlookers.*

`Wikipedia`

Contents

Abstract **3**

Acknowledgements **4**

List of Figures **13**

List of Tables **15**

List of Abbreviations **17**

1 Introduction **21**

2 Theory and Background **27**

2.1 Ultrashort Optical Physics 27

2.1.1 Ultrashort Pulses 28

2.1.2 Dispersion 31

2.1.2.1 Material Dispersion 32

2.1.3 Ultrashort Lasers 35

2.1.3.1 Mode-locking 35

2.1.3.2 SESAM 38

2.1.3.3 KLM in Ti:Sa 40

2.1.4 Nonlinear Optics 41

2.1.4.1 Second Harmonic Generation 42

2.1.4.2 Self Phase Modulation 45

2.1.5 Hollow Fibre 48

2.1.5.1 Modes 48

2.1.5.2 Coupling 50

2.1.6 Dispersion Compensation 52
2.1.6.1 Grating Compressors 53
2.1.6.2 Prism Compressors 54
2.1.6.3 Chirped Mirrors 55
2.1.7 Carrier-Envelope Phase 56
2.1.7.1 Measuring and Controlling CEP 57
2.1.8 Femtosecond Pulse Measurements 61
2.1.8.1 Intensity Autocorrelation 62
2.1.8.2 FROG 65
2.1.8.3 SPIDER 67
2.2 Strong Field Physics 71
2.2.1 Ionisation in a Strong Field 71
2.2.1.1 Ponderomotive Energy 72
2.2.1.2 The Keldysh Parameter 72
2.2.1.3 Multi Photon and Above Threshold ionisation 73
2.2.1.4 Tunnelling Regime 74
2.2.1.5 Over the Barrier Ionisation 76
2.2.2 High Harmonic Generation 76
2.2.2.1 Single Atom Response - The Three-Step Model 78
2.2.2.2 Classical Electron Trajectories 81
2.2.2.3 The Role of Phasematching in HHG 83
2.2.3 Attosecond Pulses 86
2.2.3.1 RABITT 90
2.2.3.2 Atomic Streak Camera 91
3 Waveform Stabilised Few-Cycle Drive Laser 97
3.1 Front-End 97
3.1.1 Chirped Pulse Amplification (CPA) Laser 97

3.1.1.1 Oscillator and Stretcher 98
3.1.1.2 Amplifier 99
3.1.1.3 Compressor 100
3.1.2 Carrier Envelope Phase Stabilisation 102
3.1.2.1 Fast Loop 102
3.1.2.2 Slow Loop 104
3.1.3 Overview 106
3.2 Hollow Fibre Pulse Compression 107
3.2.1 Hollow Core Fibre: Optical Setup 108
3.2.2 Spectral Broadening 109
3.2.3 Conclusion 111
4 Characterisation of High-Intensity Sub-4 fs Laser Pulses 113
4.1 Characterization of Ultrashort Pulses Using FROG 114
4.1.1 Optical Setup For a Single-Shot FROG 115
4.1.1.1 FROG Calibration 115
4.1.2 Dispersion Management 117
4.1.3 FROG Phase-matching Bandwidth 120
4.1.4 FROG Marginals 122
4.1.5 FROG Results 123
4.1.6 Conclusion 125
4.2 Characterisation of Sub-4fs Pulses Using SEA-F-SPIDER . . . 126
4.2.1 The SEA-SPIDER Setup 126
4.2.1.1 Calibration 128
4.2.2 SPIDER Trace 130
4.2.3 Experimental Results 131
4.2.4 Conclusion 133

5 Attosecond Streaking **135**

5.1 Attosecond Source 136

5.1.1 Few-cycle Laser Source 136

5.1.2 High Harmonic Generation Chamber and Target 137

5.1.3 XUV Spectrometer 139

5.1.4 High Harmonic Spectra 140

5.2 Time Of Flight Measurement 144

5.2.1 Time Of Flight Chamber 145

5.2.2 Time-Of-Flight Electron Spectrometer 149

5.2.2.1 TOF calibration 152

5.3 Attosecond Streaking 154

5.3.1 Pulse Contrast Optimisation 154

5.3.2 Attosecond Streaking 157

5.4 Conclusion 162

6 Multi-Colour HHG **165**

6.1 Brief Introduction to Two-Colour HHG and Cut-off Extension 165

6.1.1 Two-colour HHG 166

6.1.2 Extension of the Cut-Off Energy 167

6.2 Experimental Setup and Results 168

6.3 Theoretical Description 172

6.4 Conclusion 175

7 Summary and Conclusion **177**

7.1 Chapter 3 and 4: Generation and Characterisation of Few-cycle Laser Pulses 177

7.2 Chapter 5: Attosecond Streaking 178

7.3 Chapter 6: Multi-Colour HHG 179

Bibliography **181**

List of Figures

1.1 *Woman Jumping, Running Straight High Jump*: Plate 156 from *Animal Locomotion (1887)*, Eadweard J. Muybridge. 22

2.1 The electric field and intensity envelope of a 6 fs pulse centred around $\lambda = 800\,\text{nm}$ 28
2.2 The output of a hollow fibre as an example of a strongly modulated spectrum. 31
2.3 Effect of glass dispersion on a broadband spectrum 34
2.4 Improvements in ultrashort pulse generation 36
2.5 A schematic of the modelocking mechanism 37
2.6 Shape of the pulses depending on the number of locked modes . . . 39
2.7 The principle of Kerr lens modelocking 41
2.8 Frequency shift in self-phase modulation 46
2.9 Spectral broadening due to self-phase modulation 47
2.10 The radial intensity distribution of the four lowest order propagation modes in a gas-filled hollow fibre. 49
2.11 Theoretical transmission for a hollow fibre 50
2.12 Theoretical fibre coupling efficiency 51
2.13 Grating stretcher and compressor 53
2.14 A prism compressor 54
2.15 A Schematic of a Chirped Mirror 56
2.16 The electric field and intensity of a few-cycle pulse centred for two different Carrier Envelope Phase (CEP) values 57
2.17 The ratio of the peak intensities for the CEP values of $\phi_0 = 0$ and $\pi/2$ over the pulse length. 58
2.18 A diagram of a modelocked oscillator in the time and spectral domain showing the evolution of the CEP slip. 59
2.19 A schematic of a typical f-to-$2f$-interferometer setup for measuring the CEP slip of an oscillator. 61
2.20 Single shot autocorrelation setup 62
2.21 Comparison of SHG-, SD and PG-FROG beam geometries 64
2.22 A schematic of a standard SPIDER setup 69
2.23 ATI spectra for different intensities and pulse durations 75

2.24 The three-step model . . . 77
2.25 Electron Trajectories . . . 81
2.26 Long and Short Electron Trajectories . . . 82
2.27 HHG phase matching maps . . . 85
2.28 A schematic of amplitude gating . . . 88
2.29 Experimental RABITT trace . . . 89
2.30 A scematic of the atomic streaking camera . . . 91
2.31 Streaking simulations . . . 94

3.1 A schematic of the oscillator and stretcher . . . 98
3.2 A schematic of the amplification stage . . . 100
3.3 A schematic of the Femtolaser prism compressor . . . 101
3.4 CPA pulse measurement . . . 101
3.5 PCF broadened oscillator spectrum . . . 102
3.6 The optical layout of the collinear f-to-$2f$ interferometer . . . 103
3.7 A typical measurement of the CEP . . . 105
3.8 Beam profile measurement . . . 106
3.9 Schematic of the differentially pumped hollow fibre setup . . . 109
3.10 Group delay dispersion and reflectivity for the UI chirped mirrors. 110
3.11 Pulse broadening in the hollow fibre . . . 111

4.1 FROG setup . . . 114
4.2 A typical temporal calibration for the FROG setup. . . . 116
4.3 A typical spectral calibration for the FROG setup . . . 117
4.4 FROG calibration testing . . . 118
4.5 Dispersion and reflection curves for Ag- and Al- mirrors . . . 119
4.6 Dispersion and reflection properties of the FROG beamsplitter . . 119
4.7 SHG efficiency for two BBO crystals . . . 121
4.8 FROG marginal correction . . . 122
4.9 FROG Results . . . 124
4.10 SEA-F-SPIDER setup . . . 127
4.11 A typical spectral calibration for our SPIDER setup . . . 128
4.12 Shear Calibration . . . 129
4.13 SEA-F-SPIDER trace . . . 130
4.14 Spatially resolved reconstruction of a few-cycle laser pulse . . . 132
4.15 1D SPIDER reconstruction . . . 134

5.1 The IR spectrum before entering the HHG chamber. . . . 137
5.2 HHG Beamline . . . 138
5.3 A schematic of the pulsed gas jet. . . . 139
5.4 Flat-field Spectrometer . . . 140
5.5 Flat-field Spectral Calibration . . . 141
5.6 High harmonic CEP scan . . . 142
5.7 High harmonic spectrum for CEP = 0 . . . 143

5.8 Side-peak intensity of a cosine-pulse over pulse-duration 144
5.9 Time-of-flight chamber 145
5.10 Transmission and reflectivity curves for a 200 nm thick Zr foil and a MoSi mirror. 146
5.11 Needle scan along x- and z-direction 147
5.12 Temporal and spatial overlap measurement. 148
5.13 Schematic of the time-of-flight electron spectrometer. 150
5.14 The time of flight for electrons as a function of their initial kinetic energy for two different voltages. 151
5.15 TOF length calibration. 153
5.16 Pulse contrast measurement illustration. 155
5.17 Experimental streaking CEP-scan. 156
5.18 Attosecond pulse contrast measurement 157
5.19 Unstreaked photoelectron spectrum in neon. 158
5.20 Experimentally obtained streaking spectrogram. 159
5.21 Temporal profile of the attosecond pulse 160
5.22 Attosecond pulse retrieval 161
5.23 Fourier filtering and background correction of the electron spectra. 162

6.1 Two-colour high harmonic setup. 169
6.2 Two-colour fields 170
6.3 Experimental harmonic spectra from a two-colour orthogonally polarised field 171
6.4 High harmonic yield as a function of the two-colour phase delay. . 172
6.5 Two-colour SFA calculations 173
6.6 Quantum orbit calculation for high harmonic yield in an orthogonally-polarised two-colour field. 174
6.7 Harmonic order as a function of travelling time. 175

List of Tables

2.1 The temporal intensity profiles for the most commonly used pulse shapes and their time-bandwidth product (TBP) 30
2.2 The Sellmeier coefficients up to the second order for the materials plotted in Figure 2.3 (a) taken from the Schott optical data spreadsheet [1]. For Figure 2.3, coefficients up to the third order were used. 33
2.3 Examples of the required spectral FWHM bandwidth for different pulse widths. The temporal shape is assumed to be a Gaussian pulse and the width is given by the FWHM. 38
2.4 Nonlinear optical phenomena and their corresponding nonlinear susceptibility 43
2.5 Centre wavelength $\lambda = 800\,\text{nm}$, Grating compressor with 600 lines/mm, AOI= 15°, L_g =5 cm. Prism compressor with Brewster angle, minimum deviation for SF18 and distance tip-to-tip 10 cm, AOI = 59.61°, prism angle: 60.78° 55

5.1 The relative potentials of the electrostatic lens system, where V is the voltage applied to the drift tube. 150

List of Abbreviations

ADK Ammosov, Delone and Krainov ionisation theory [2]

AOM Acousto-Optic Modulator

APT Attosecond Pulse Train

ATI Above Threshold Ionisation

BBO Beta Barium Borate

CCD Charge-Coupled Device

CEP Carrier Envelope Phase

CPA Chirped Pulse Amplification

FOD Fourth Order Dispersion

FROG Frequency-Resolved Optical Gating

FROG-CRAB FROG for the Complete Reconstruction of Attosecond Bursts

FWHM Full-Width at Half Maximum

GDD Group Delay Dispersion

GVD Group Velocity Dispersion

HHG High-Harmonic Generation

IR Infra-Red

MCP Microchannel Plate

MoSi Molybdenum-Silicon

MPI Multi Photon Ionisation

NIR Near Infra-Red

OTBI Over the Barrier Ionisation

PCF Photonic Crystal Fibre

PG-FROG Polarisation Gated FROG

RABBITT Reconstruction of Attosecond Beating by Interference of Two-photon Transitions

SAP Single Attosecond Pulse

SD-FROG Self-Diffraction FROG

SEA-SPIDER SPIDER in a Spatially Encoded Arrangement

SEA-F-SPIDER SPIDER in a Spatially Encoded Filter Arrangement

SFA Strong-Field Approximation

SHG Second-Harmonic Generation

SPIDER Spectral Phase Interferometry for Direct Electric Field Reconstruction

TDC Time to Digital Converter

TOD Third Order Dispersion

TOF Time-of-flight Spectrometer

UV Ultraviolet

XUV Extreme Ultraviolet

Chapter 1

Introduction

The measurement of fast dynamics calls for probing methods that are faster than the rate of change of the measured object. The human brain merges images that are changing at a rate faster than 24 Hz (the standard film rate) which is equivalent to a temporal resolution of $t_{\mathrm{res}} \gtrsim 40\,\mathrm{ms}$. To resolve processes that are faster than this different technologies have to be used. Eadweard Muybridge was a pioneer in the early years of photography and well known for his image of a race horse with all its hooves off the ground. But he also made other time resolved image series, one of which is shown in Figure 1.1

The timescales we are able to access today are of course much shorter than the human eye can resolve. As part of the Attosecond Technology project, we are interested in the fundamental processes of chemistry, biology and materials that are governed by the dynamics of electrons. The timescales of the electronic motion is on the order of attoseconds as can be estimated by the orbit time of the electron in the hydrogen ground state: $T_{\mathrm{orbit}} = 150\,\mathrm{as}$. One attosecond is a billionth of a billionth of a second, an incredibly short time. In other words, if one attosecond would be one second, than one second



Figure 1.1: *Woman Jumping, Running Straight High Jump*: Plate 156 from *Animal Locomotion (1887)*, Eadweard J. Muybridge.

would be more than two times the age of the universe (the time elapsed since the Big Bang is estimated to be 13.7 billion years).

In this thesis, the generation and characterisation of some of the shortest light pulses in the world is described. Attosecond science has evolved rapidly over the last couple of years. The first sub-femtosecond pulses (650 as) were measured in the early 2000s [3]. Now, we are approaching the atomic unit of time, i.e. $T_{\text{orbit}}/2\pi = 24\,\text{as}$, with the shortest isolated attosecond pulses measured being as short as 80 as [4]. These isolated pulses in combination with attosecond metrology [5] were recently used to measure a delay of 21 as in photoionisation from the 2p orbitals of neon with respect to the 2s orbital [6].

Attosecond light pulses are generated using extremely short bursts of Extreme Ultraviolet (XUV) derived from high harmonic generation (HHG) [7, 8]. This method has been pushed forward by the generation of wave-form controlled high-intensity laser pulses with an extremely short pulse duration. The duration of these laser pulses is only a few cycles of the optical period ($T = 2.7\,\text{fs}$ at 800 nm) [9]. When such an intense laser pulse, exceeding $10^{14}\,\text{W/cm}^2$, interacts with an atom, an electron can tunnel ionise and is

subsequently accelerated by the electric field of the laser. At recombination with its parent ion, high energy XUV photons are generated [10, 11], that can be used to produce attosecond pules.

The high harmonic generation process is a useful tool not only for the generation of ultrashort pulses, but it can also be used to deliver high energy photons from a table-top system to a broad scientific community. The use of longer wavelength driving fields increases the maximum energy from high harmonics [11] but at the same time decreases the efficiency of the process. On the other hand, using a two-colour field, one gains access to additional parameters to steer the electron in the continuum. This has been shown to enhance the generation of high harmonics [12, 13] and in conjunction with the use of longer wavelengths is a promising route to compact high flux sources of high energy photons.

Author's Contribution to the Work

I have played a major role in all the aspects of the experimental work detailed in this thesis. As part of a team with Dr. Christoper Arrell and Dr. Tobias Witting and more recently William Okell, I have been involved in the operation and development of a commercial phase-stabilised Femtolasers system. I was the principal contributor of the optimisation and incorporation of a hollow-fibre system that produces 3.5 fs pulses. I have built a FROG apparatus capable of measuring few-cycle laser pulses and developed the necessary tools to calibrate the system and correct for systematic errors in the measurement.

Together with Dr. Tobias Witting, I was closely involved in the setting up of a SEA-F-SPIDER to spatially characterise the output of our hollow

fibre system. This work has been published in optics letters and I played a main role in writing up the manuscript.

As part of a team, I have used the few-cycle laser source to generate harmonics. The harmonics were used in collaboration with a team from Oxford for the frequency-resolved wavefront characterization of high harmonics, which is not discussed here.

The harmonics were also used to generate and characterise the first single attosecond pulse in the UK. I was involved in all aspects of the attosecond streaking measurements and am able to run the attosecond streaking experiment independently. I was the principal contributor for the calibration and simulation of the time-of-flight electron spectrometer and played a major role in the most recent measurements of single attosecond pulses. I have used a FROG-CRAB algorithm written by Dr. Tobias Witting for the complete characterisation of said attosecond pulses.

In collaboration with Leonardo Brugnera, I have set up a two-colour high harmonic experiment at the Central Laser Facility at Rutherford Appleton Laboratory. I have analysed and written up the experimental results, while the theoretical calculations have been done by Leonardo Brugnera in collaboration with David Hoffmann and Dr. Ricardo Torres.

The following papers have resulted from work I have been involved in:

Publications

Characterization of high-intensity sub-4-fs laser pulses using spatially encoded spectral shearing interferometry T. Witting, F. Frank, C. A. Arrell, W. A. Okell, J. P. Marangos and J. W. G. Tisch, *Optics Letters* **36**(9), 1680–1682 (2011).

Enhancement of high harmonics generated by field steering of electrons in a two-color orthogonally polarized laser field L. Brugnera, F. Frank, D. J. Hoffmann, R.Torres, T. Siegel, J. G. Underwood, E. Springate, C. Froud, E. I. C. Turcu, J. W. G. Tisch and J. P. Marangos, *Optics Letters* **35**(23), 3994–3996 (2010).

Trajectory selection in high harmonic generation by controlling the phase between orthogonal two-color fields L. Brugnera, D. J. Hoffmann, T. Siegel, A. Zaïr, F. Frank, R. Torres, J. W. G. Tisch and J. P. Marangos, *Physical Review Letters* submitted.

Lateral shearing interferometry of high-harmonic wavefronts D. R. Austin, T. Witting, C. Arrell, F. Frank, A. S. Wyatt, J. P. Marangos, J. W. G. Tisch and I. A. Walmsley, *Optics Letters* **36**(10), 1746–1748 (2011)

Technology for Attosecond Science F. Frank, C. Arrell, T. Witting, W. Okell, E. Skopalov, J. McKenna, R. A. Smith, J. P. Marangos and J. W. G. Tisch, *Progress in Quantum Electronics* in preparation

Organisation of Thesis

In Chapter 2 I present the theory and background to the work described in the later chapters of this thesis. Specifically, I will describe the main concepts of ultrashort optical physics and strong field physics. Chapter 3 is concerned with the generation of a phase-stabilised few-cycle laser system that was used for the generation of single attosecond pulses. Chapter 4 describes the complete characterisation of the few-cycle pulse. A FROG and a SPIDER setup was used to measure a sub-4 fs pulse. In chapter 5 the generation and characterisation of a single attosecond pulse with an atomic streaking camera is discussed. The final experimental chapter, Chapter 6, is

about high harmonic generation from an orthogonally polarised two-colour field from an mid-IR laser source. Finally, Chapter 7 summarises the work conducted during my PhD and gives a brief outlook on future experiments.

Chapter 2

Theory and Background

2.1 Ultrashort Optical Physics

In this section I will describe the physics of ultrashort optical pulses, beginning with a mathematical description of ultrashort pulses. I will then describe the dispersive effects of material on short pulses. Next, methods to generate short laser pulses are described and the most important nonlinear effects relevant for the work described in this thesis, Second-Harmonic Generation (SHG) and self-phase modulation, are discussed in some detail. The mathematical description of propagation in and coupling into a hollow-core fibre are then introduced before describing methods of material dispersion compensation. The measurement and control of the Carrier Envelope Phase (CEP), a very important measure in few-cycle pulses, is discussed, before going into more detail of the measurement of these ultrashort optical pulses.

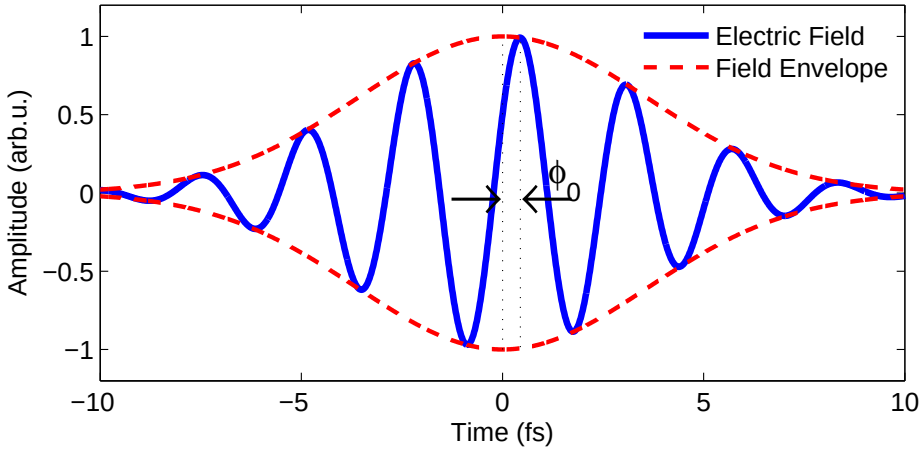


Figure 2.1: The electric field of a 6 fs pulse centred around λ =800 nm with an arbitrarily set CEP of $\phi_0 = \pi/3$. The FWHM of the field envelope is $\sqrt{2}$ larger than the FWHM of the intensity envelope

2.1.1 Description of Ultrashort Optical Pulses

The electric field of an ultrashort, linearly polarised optical pulse travelling in z-direction can be described as follows:

$$E(z,t) = A(z,t)e^{i(\omega_0 t - k_0 z + \phi(t))} = A(z,t)e^{i\varphi(z,t)}, \tag{2.1}$$

where $A(z,t)$ is the slowly varying envelope of the wavepacket (see section 2.1.4.1), ω_0 the carrier frequency and $k_0 = n(\omega_0)\frac{\omega_0}{c}$ the wavenumber. The temporal phase, $\phi(t)$, is best described in a Taylor expansion around $t = 0$:

$$\phi(t) = \sum_{n=0}^{\infty} \frac{1}{n!} \frac{\mathrm{d}^n \phi(t)}{\mathrm{d}t^n}\bigg|_{t=0} t^n = \sum_{n=0}^{\infty} \frac{1}{n!} \phi_n(t)\, t^n \,, \tag{2.2}$$

where $\phi_n(t) = \frac{\mathrm{d}^n \phi(t)}{\mathrm{d}t^n}\Big|_{t=0} t^n$. The offset between the maximum of the envelope and the field, given by ϕ_0, is the CEP, a measure that becomes very important when talking about the instantaneous intensity of a field, $I(t) \propto |E(t)|^2$,

in the few cycle limit (see subsection 2.1.7). In the oscillating part of Equation 2.1, the temporal phase $\phi(z,t)$, defines the variation of the carrier frequency in time. The instantaneous angular frequency, $\omega(z,t)$, can then be written as the time derivative:

$$\omega(z,t) = \frac{\partial\varphi(z,t)}{\partial t}. \tag{2.3}$$

In ultrashort optics, pulses consist of a large bandwidth of different wavelengths. It is therefore often easier to switch from the temporal domain to the spectral domain, when describing an optical pulse and its dispersion (described in the next section). This is simply done by using Fourier theory. A pulse in the spectral domain can be written as:

$$\widetilde{E}(z,\omega) = A(z,\omega)e^{i\phi(z,\omega)}, \tag{2.4}$$

where $A(z,\omega)$ and $\phi(z,\omega)$ are are the spectral amplitude and phase, respectively. Equation 2.1 and Equation 2.4 are linked by a simple Fourier transformation:

$$E(z,t) = \frac{1}{\sqrt{2\pi}}\int \widetilde{E}(z,\omega)e^{-i\omega t}d\omega, \tag{2.5}$$

$$\widetilde{E}(z,\omega) = \frac{1}{\sqrt{2\pi}}\int E(z,t)e^{i\omega t}dt. \tag{2.6}$$

Since time and frequency are Fourier pairs, a large bandwidth of frequencies is required in order to generate a short pulse. A time-bandwidth product (TBP) can be calculated for different pulse shapes, by using Equation 2.5 and Equation 2.6. The TBP is defined as:

$$\text{TBP} = \Delta\nu\Delta t, \tag{2.7}$$

where $\Delta\nu$ and Δt are the Full-Width at Half Maximum (FWHM) of the spectral and the temporal distributions. A number of TBPs for different

Table 2.1: The temporal intensity profiles for the most commonly used pulse shapes and their time-bandwidth product (TBP)

Pulse Shape	Temporal Intensity Profile	TBP
Gaussian	$e^{-\frac{(4\ln 2)t^2}{\Delta t^2}}$	$\frac{\ln(4)}{\pi} \approx 0.441$
Sech^2	$\text{sech}^2\left(\frac{2\ln(1+\sqrt{2})t}{\Delta t}\right)$	$\left(\frac{2\sinh^{-1}(1)}{\pi}\right)^2 \approx 0.315$
Square	1 for $\lvert t\rvert < \Delta t/2$ 0 for all other t	0.886

pulse shapes are given in Table 2.1. One should be cautious when using the FWHM to gain insight into the shortest possible pulse. Especially for strongly modulated spectra, the FWHM can be misleading. It is then best to do a Fourier transformation and calculate the transform limited pulse length by assuming a flat phase over the spectrum, i.e. take $E(\omega) = A(\omega)e^{i\phi(\omega)} = A(\omega)$ and then Fourier transform this equation to get the transform limited temporal shape. I demonstrate this in Figure 2.2 by calculating the transform limited pulse corresponding to a typical broadened spectrum at the output of our hollow fibre (see section 3.2). It shows, that the FWHM measure of the spectrum is not a good measure in few-cycle optics, where the pulse spectra are heavily modulated.

The spectral phase, $\phi(z, \omega)$, plays an important role in obtaining the shortest pulse duration. Therefore variations in phase for different frequencies need to be minimized, as they lead to a reshaping of the temporal pulse envelope. This proves to be a complicated task for ultrashort pulses. Even when propagating in air, these broadband pulses will broaden temporally and special

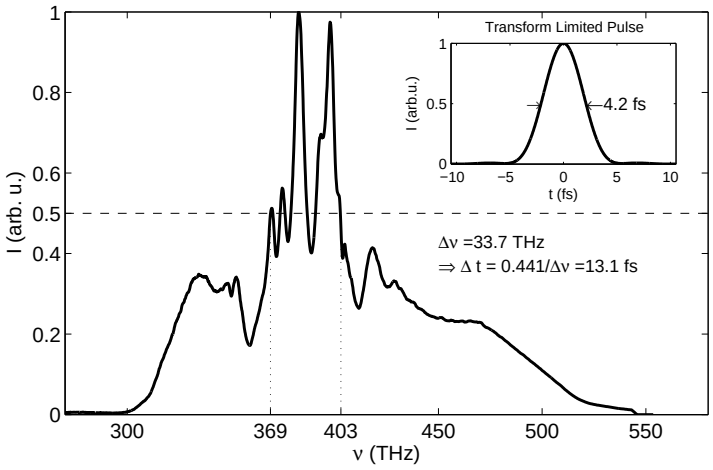


Figure 2.2: The output of a hollow fibre as an example of a strongly modulated spectrum, corresponding to a Fourier transform limited pulse duration of 4.2 fs. The pulse duration calculated from the FWHM of the spectrum ($\Delta\nu = 33.7\,\mathrm{THz}$) is 13.1 fs.

care has to be taken to compensate for this dispersion. For example, a 5 fs transform-limited pulse centred at $\lambda = 800\,\mathrm{nm}$ will be stretched to 12.5 fs in just 1 m of air.

2.1.2 Dispersion

First I will examine the spectral phase from Equation 2.4 by Taylor expanding it (similar to Equation 2.2) around the centre frequency ω_0:

$$\phi(\omega) = \sum_{n=0}^{\infty} \frac{1}{n!} \frac{\mathrm{d}^n \phi(\omega)}{\mathrm{d}\omega^n}\bigg|_{\omega_0} (\omega - \omega_0)^n = \sum_{n=0}^{\infty} \varphi_n (\omega - \omega_0)^n, \tag{2.8}$$

where we have defined $\varphi_n = \frac{1}{n!} \frac{\mathrm{d}^n \phi(\omega)}{\mathrm{d}\omega^n}\Big|_{\omega_0}$. The first term φ_0 is the CEP as mentioned earlier (see also subsection 2.1.7). The next term is the group delay, $\frac{d\phi}{d\omega}\big|_{\omega_0}$, closely related to the group velocity defined in Equation 2.10. The CEP shifts the phase and, according to Equation 2.1, does not affect the

envelope of the pulse. Neither does the second term. The group delay shifts the centre of the envelope, as is discussed in more detail elsewhere [14]. The subsequent terms, on the other hand, are important in obtaining the shortest pulse duration, i.e. the shortest temporal envelope. The most dominant of these terms is the group delay dispersion (GDD), $\frac{d^2\phi}{d\omega^2}\Big|_{\omega_0}$. Most materials introduce a positive dispersion, GDD > 0, where the short wavelengths will be delayed with respect to the longer wavelengths. The opposite case, $\frac{d^2\phi}{d\omega^2}\Big|_{\omega_0} < 0$, is referred to as anomalous or negative dispersion. Any pulse undergoing dispersion is then said to be *chirped*, meaning its instantaneous frequency is time dependent.

The larger the bandwidth the more important are the higher orders of Equation 2.8 and in practice third order dispersion (TOD) is also taken into consideration when producing ultrashort pulses in the few-cycle regime [15].

2.1.2.1 Material Dispersion

When an optical pulse travels through a medium, the electronic response of the medium is different for each frequency. This is called dispersion and is shown in the wavelength dependence of the refractive index $n(\lambda)$. The accumulated phase for an optical pulse propagating a distance L in a material is given by:

$$\phi_{\mathrm{mat}}(\omega) = k(\omega)L = \frac{\omega\ n(\omega)}{c}L \tag{2.9}$$

and from this we can calculate the evolution of the temporal envelope. This can be seen, when looking at the group velocity, $v_g = \frac{d\omega}{dk}$, of a pulse. Since the wavenumber varies with frequency, so will the group velocity:

$$v_g = \frac{\mathrm{d}\omega}{\mathrm{d}k} = \left(\frac{\mathrm{d}k}{\mathrm{d}\omega}\right)^{-1} = \left(\frac{\mathrm{d}}{\mathrm{d}\omega}\left(\omega\ n(\omega)/c\right)\right)^{-1}. \tag{2.10}$$

Table 2.2: The Sellmeier coefficients up to the second order for the materials plotted in Figure 2.3 (a) taken from the Schott optical data spreadsheet [1]. For Figure 2.3, coefficients up to the third order were used.

Material	B_1	B_2	C_1 in µm^2	C_2 in µm^2
FS	0.69616630	0.40794260	0.0046791482	0.013512063
K7	1.1273555	0.124412303	0.00720341707	0.0269835916
F2	1.34533359	0.209073176	0.00997743871	0.0470450767
SF10	1.61625977	0.259229334	0.0127534559	0.0581983954

This shows that there is no well defined group velocity for a pulse. The fact that each spectral component has its own group velocity is called group velocity dispersion (GVD) and $k'' = \frac{\mathrm{d}^2 k}{\mathrm{d}\omega^2}\Big|_{\omega_0}$ is a measure for this quantity, with $\frac{\mathrm{fs}^2}{\mathrm{m}}$ as its unit.

The wavelength dependence of the refractive index can be expressed in the form of a Sellmeier equation:

$$n^2(\lambda) = 1 + \sum_i \frac{B_i \lambda^2}{\lambda^2 - C_i}, \tag{2.11}$$

where B_i and C_i are the Sellmeier coefficients.

The group velocity dispersion and third order dispersion in terms of the refractive index are given as:

$$\mathrm{GVD} = \frac{\lambda^3}{2\pi c^2} \frac{\mathrm{d}^2 n}{\mathrm{d}\lambda^2}, \tag{2.12}$$

$$\mathrm{TOD} = -\frac{\lambda^2}{4\pi^2 c^3} \left(3\lambda^2 \frac{\mathrm{d}^2 n}{\mathrm{d}\lambda^2} + \lambda^3 \frac{\mathrm{d}^3 n}{\mathrm{d}\lambda^3} \right). \tag{2.13}$$

When a pulse propagates through dispersive material, phase is accumulated and the shape of the pulse will alter. Mathematically this is described by calculating the accumulated phase, $\phi_{\mathrm{mat}}(\omega)$, and multiplying the spectral

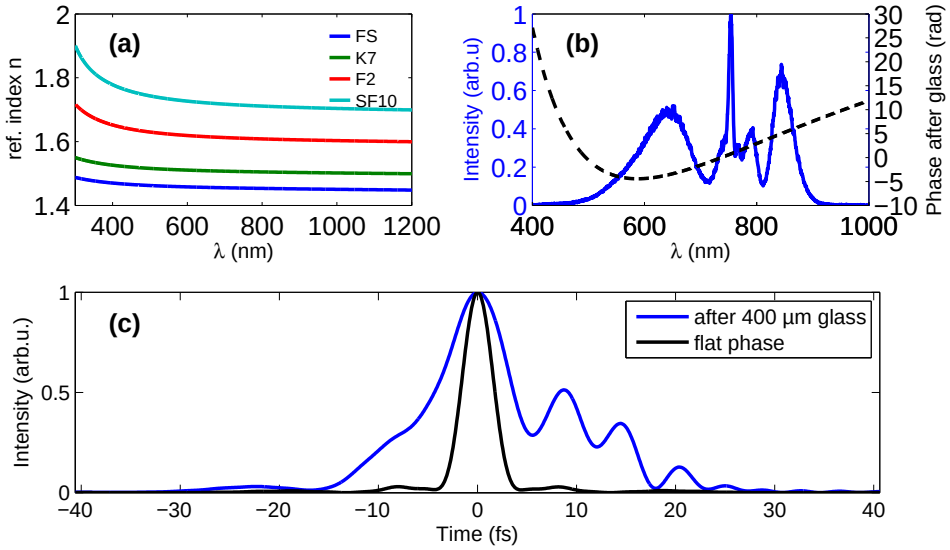


Figure 2.3: (a) Dispersion curves for different types of glass calculated from the Sellmeier coefficients.
(b) Typical measured spectrum (blue) for a hollow-fibre output and the calculated phase (black) accumulated from 400 µm of fused silica (with subtraction of the linear phase).
(c) The temporal profile calculated from the spectrum in b) with a flat phase (black) and with the phase shown in b) (blue). The pulse gets stretched from $\Delta t = 3.5\,\text{fs}$ in the transform limited case to Δt =13.5 fs after propagation through the glass, where Δt is the FWHM.

amplitude by $e^{i\phi(\omega)}$. In addition to the phase accumulation, the frequency-dependent transmission of the material, $T(\omega)$, can also taken into account.. Inverse Fourier transformation then gives the temporal shape of the pulse:

$$E(t) \xrightarrow{\mathcal{F}} A(\omega)e^{i\phi(\omega)} \xrightarrow{\text{material}} A(\omega) \times T(\omega)e^{i[\phi(\omega)+\phi_{\text{mat}}(\omega)]} \xrightarrow{\mathcal{F}^{-1}} E'(t)$$

In Figure 2.3 I have calculated the accumulated phase and resulting temporal stretching of a short pulse when propagating through 400 µm of fused silica.

2.1.3 Ultrashort Lasers

Ultrafast lasers have dramatically improved over the last decades. Laser pulse generation started as early as 1962 by McClung *et al.*, only two years after the first demonstration of a laser [16]. De Maria *et al.* produced the first pulses using a passively mode-locked Nd:glass laser, generating picosecond pulses [17]. Figure 2.4 shows the evolution of ultrafast lasers up to the present day. In the early times usually dye lasers were used to achieve ultrashort pulses. With the discovery of the broad gain bandwidth medium Ti:Sapphire [18] and the development of Kerr-lens mode-locking (KLM) [19, 20], a new era started that is producing pulses as short as a few cycles of the fundamental wavelength [9]. The next step towards shorter pulses came with the use of high harmonic generation (HHG - see subsection 2.2.2). Here, broadband Extreme Ultraviolet (XUV) pulses can be produced and due to the shorter wavelength, pulses as short as 80 as have been generated [4].

2.1.3.1 Mode-locking

Short pulses are generated by Q-switching [16, 21] or mode-locking [15, 17, 22], but only the latter is suitable for femtosecond pulses. Modelocking refers to pulse formation by constructive interference when many longitudinal modes oscillate in phase in a laser resonator. All of the longitudinal modes satisfy the standing wave condition $m\lambda = 2L$, where m is a positive integer and L the length of the cavity. The frequency separation is determined by adding half a wavelength ($m \rightarrow m + 1$) and is given by:

$$\Delta\nu = \frac{c}{2L}. \tag{2.14}$$

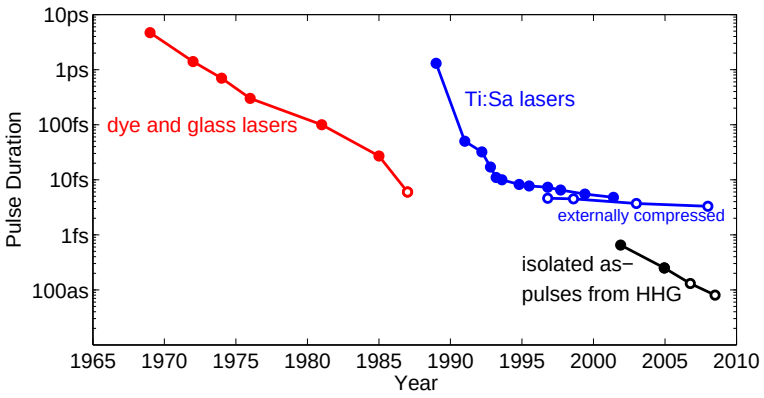


Figure 2.4: Improvements in ultrashort pulse generation. Until the late 1980's dye lasers were used, reaching pulse lengths as short as 27 fs (even 6 fs with external pulse compression). The discovery of Ti:Sapphire as a laser medium gave new alternatives to reach even shorter pulse widths down to almost a single cycle [9]. By using HHG much shorter wavelengths can be generated and the pulse durations reach a new domain, namely the attosecond domain. Only single, isolated as-pulses are shown in this graph. Filled symbols indicate results directly achieved from a laser and open symbols are achieved with additional external broadening and/or compression

If the phase of each mode is locked, $\Phi_{m+1} - \Phi_m = \alpha = \text{const}$, the output is a pulse train. For $\alpha = 0$ and $N = 2M + 1$ modes, the superposition can be written as:

$$\vec{E}(t) = \sum_{m=-M}^{M} \vec{E}_0 e^{2\pi i(\nu_0 + m\Delta\nu)t}, \tag{2.15}$$

where ν_0 is the centre frequency. The intensity can than be written as[i] [23, 24]:

$$I(t) \propto |E(t)|^2 \propto \left(\frac{\sin\left[(2N+1)(\pi\ \Delta\nu\ t)\right]}{\sin(\pi\ \Delta\nu\ t)} \right)^2. \tag{2.16}$$

[i] using the identity: $\sum_{n=-(N-1)/2}^{(N-1)/2} e^{iny} = \frac{\sin(Ny/2)}{\sin(y/2)}$

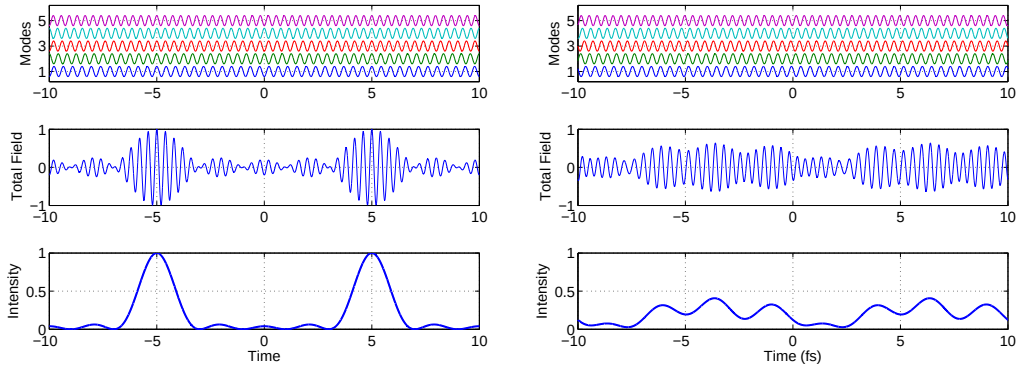


Figure 2.5: A schematic of the modelocking mechanism. **Left:** Five modes are locked in phase and added up. The intensity gets localized at positions where all the modes have a maximum and deconstructively interfere elsewhere. **Right:** Ten modes with a random phase. Here, the intensity distribution is random and no pulse is formed.
Top: each mode shown separately. **Middle:** the resulting field. **Bottom:** the resulting intensity

In Figure 2.5 I have calculated the intensity for seven locked modes. At $t = 0$ and $t = T = \frac{2L}{c}$ the superposition of those modes leads to a maximum. The maxima get more pronounced the more modes are involved and the temporal width can be estimated as $\tau_N = \frac{T}{N}$. The total number of modes that are supported by any laser medium is determined by the gain bandwidth $\Delta\nu_g$ and the frequency separation $c/2L$. Assuming sufficiently strong pumping the total number of longitudinal modes is given by $N_{\text{tot}} = \frac{\Delta\nu_g}{c/2L}$ and thus the shortest pulse duration one can expect is:

$$\tau_{min} \approx \frac{1}{\Delta\nu_g}. \tag{2.17}$$

As one can see, this equation is very similar to the minimal pulse duration given in Equation 2.7. The minimum bandwidth assuming a Gaussian pulse

shape and using $\Delta\nu = \frac{c}{\lambda^2}\Delta\lambda$ are given in Table 2.3.

Furthermore, if the intensity of the modes is modulated by a Gaussian

Table 2.3: Examples of the required spectral FWHM bandwidth for different pulse widths. The temporal shape is assumed to be a Gaussian pulse and the width is given by the FWHM.

τ	$\lambda = 800$ nm	$\lambda = 1054$ nm	$\lambda = 1500$ nm
500 fs	1.8 nm	3.1 nm	6.4 nm
100 fs	10 nm	16 nm	30 nm
30 fs	30 nm	50 nm	100 nm
10 fs	90 nm	160 nm	310 nm
		bandwidth $\Delta\lambda$	

profile as indicated in Figure 2.6, the side-maxima vanish. This situation very well describes the situation of a typical laser medium like Ti:Sapphire or Nd:glass.

A number of techniques are available to lock modes in an oscillator in order to get a short pulse. There is acoustic loss modulation, based on the diffraction of light by sound waves (Brillouin-scattering) [25]. Another way is using an electro-optical effect, where the refractive index is linear to an applied electric field. This method modulates the phase rather than the amplitude [23, 24]. Yet another and the most commonly used way is using a saturable absorber.

2.1.3.2 SESAM

Semiconductor saturable absorbers (SESAM) came up in the early 1990s and have significantly improved ever since [22]. The basic principle behind it is the occupation of final states (in the conduction band) or depletion of the

initial states (in the valence band) by photon transitions. If all the final states are occupied, no more photons can be absorbed and the absorption is saturated. Due to the advances in semiconductor engineering and growth technologies, they can be designed for a variety of applications. Their integration in mirrors make them very easy to handle. They have been used for picosecond to femtosecond pulses, Q-switching and CW-mode locking. The challenging part in the design is to keep the non-saturable losses to a minimum to maintain an efficient laser. In addition the bandwidth of the SESAM should not restrict the gain bandwidth of the laser medium to guarantee short pulses [26]. An inherently easier way to accomplish a saturable absorber, without the use of semiconductors, is the exploitation of the Kerr effect in a nonlinear medium.

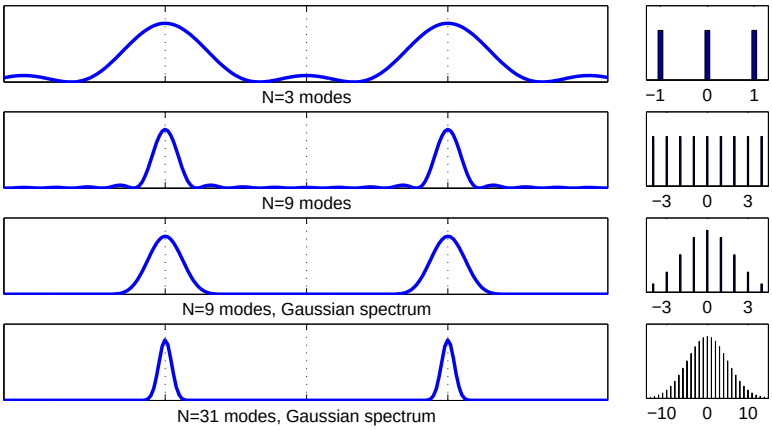


Figure 2.6: Shape of the pulses depending on the number of locked modes. The side-maxima vanish, when the modes are modulated by a Gaussian. The widths of the Gaussian spectra are: $\sigma_9 = 2$ and $\sigma_{31} = 5$, respectively.

2.1.3.3 Kerr Lens Mode-Locking in Ti:Sa

Kerr lens modelocking was first discovered in 1990. The group of Ishida *et al.* and Sibbett's group both presented fs-pulses that could not be described with the common mode-locking theories [19, 20]. There was no visible saturable absorber present in Sibbett's lasers, which led to the term 'magic mode-locking'. It did not take long for the first explanations of this phenomenon and many papers on this matter have been published shortly afterwards [27–31]. It was found that the high intensities in the laser cavity lead to nonlinear effects in the laser crystal. One of them being the 'Kerr effect'[ii], which is responsible for an intensity dependent refractive index:

$$n(r,t) = n_1 + n_2 I(r,t). \tag{2.18}$$

Here the optical beam itself is strong enough to introduce such a nonlinearity. In combination with a Gaussian shaped pulse, this leads to a higher (lower) refractive index in the middle (on the flanks) of the pulse. Just like in a normal lens, the optical path is now longer at the centre of the pulse, resulting in a focused beam. This alone does not make a saturable absorber. In order to favour the high intensity an aperture is build into the resonator as seen in Figure 2.7. The CW-mode will be partially blocked by the aperture, i.e. its loss will be high, while a pulse with higher intensity is not affected by the aperture. Instead of using a hard aperture in the cavity, most fs-oscillators use a so-called soft-aperture, where the pump geometry acts as an aperture. The Kerr-lens focused beam has a larger overlap with the pump beam and therefore a higher average gain than the low-intensity beam, giving rise to the same pulse forming mechanisms.

Because a high intensity is needed to make a considerable change in the

[ii] named after the Scottish physicist John Kerr (1824-1907)

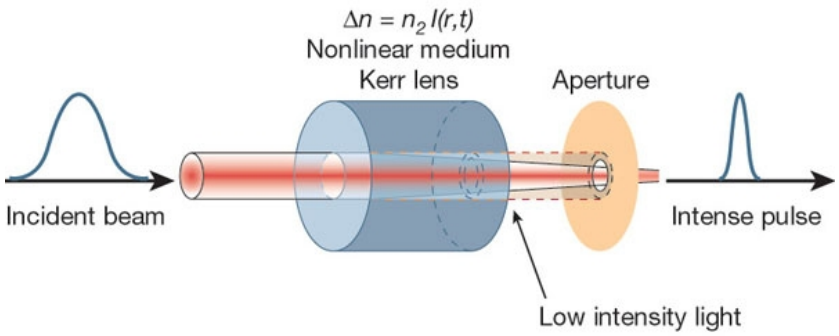


Figure 2.7: The principle of Kerr lens modelocking. The nonlinear refractive index n_2 in an intracavity material (usually the gain medium) focuses the intense beam. Low intensities are blocked by an aperture. [22]

mode size, KLM lasers are usually not self-starting. A brief perturbation, like vibrating one of the intra-cavity mirrors, is often used. This gives rise to some intensity fluctuations that will than start the pulse forming process. Another disadvantage is that KLM works best close to the stability limit of the cavity. A correct alignment is therefore critical and sub micrometer accuracy is needed to establish ultrashort pulses.

2.1.4 Nonlinear Optics

Nonlinear optical phenomena occur when light is strong enough to induce a nonlinear response in a medium, i.e. a nonlinear response to the electric field of the light. This can happen, when the electronic response is not linear with the electric field because the intensities are too high [32]. Typically only lasers can have intensities that are high enough to induce significant nonlinear effects in a material and often pulsed lasers with very high instantaneous intensities are used to exploit nonlinear effects.

2.1.4.1 Second Harmonic Generation

The first demonstration of a nonlinear effect in a laser field, second harmonic generation, was not long after the laser was invented. Optical frequency doubling was first demonstrated by Franken *et al.* in 1961 [33]. Here, the electronic response scales not linear but quadratic with the light field, leading to the generation of a light field with twice the frequency. This can be described by looking at the wave equation (Equation 2.19) and taking a Taylor expansion of the induced polarisation $\vec{P}$ (Equation 2.20).

Wave Equation The wave equation for an optical field is given by:

$$\nabla^2 \vec{E} - \frac{1}{c^2}\frac{\partial^2}{\partial t^2}\vec{E} = \mu_0 \frac{\partial^2}{\partial t^2}\vec{P}, \tag{2.19}$$

where $\vec{E}$ is the real electric field, c is the vacuum speed of light, μ_0 the magnetic permeability and $\vec{P}$ the real induced polarisation. The polarisation is the dipole moment per unit volume that arises from the distortion of the electron cloud, due to an external field. For weak external fields, the distortion can be approximated to be linear with the electric field and is described by the complex refractive index. But for higher fields this no longer holds true and nonlinear effects have to be taken into consideration. Assuming the polarisation only depends on the instantaneous field it can be written as a Taylor series in powers of the electric field:

$$\vec{P} = \varepsilon_0 \left[\chi^{(1)}\vec{E} + \chi^{(2)}\vec{E}^2 + \chi^{(3)}\vec{E}^3 + \cdots \right], \tag{2.20}$$

where $\chi^{(n)}$ is the n^{th} order nonlinear susceptibility (in general a tensor). Table 2.4 summarizes some nonlinear optical effects and the corresponding order of χ.

Table 2.4: Nonlinear optical phenomena and their corresponding nonlinear susceptibility

nonlinear effect	susceptibility
Second harmonic generation	$\chi^{(2)}$
Sum and difference frequency generation	$\chi^{(2)}$
Parametric amplification	$\chi^{(2)}$
Self-phase modulation	$\chi^{(3)}$
Kerr-lensing	$\chi^{(3)}$
Four-wave mixing	$\chi^{(3)}$
Self diffraction	$\chi^{(3)}$

The Slowly Varying Envelope Approximation To simplify the wave equation two approximations can be made. The first approximation is called the slowly varying envelope approximation, which states that the change of the envelope is much less then the rate of change of the underlying carrier wave. Therefore the second derivatives of of the wave equation in time and space can be neglected:

$$\text{(I)}: \frac{\partial^2 E}{\partial t^2} \ll \omega_0 \frac{\partial E}{\partial t} \quad \text{and} \quad \text{(II)}: \frac{\partial^2 E}{\partial z^2} \ll k_0 \frac{\partial E}{\partial z}. \tag{2.21}$$

Secondly, the non-depleted pump approximation is used here, stating that little energy is transferred from the fundamental and thus its intensity considered constant over the length of the nonlinear medium. With these assumptions Equation 2.19 can be written as:

$$\frac{\partial E}{\partial z} = -i \frac{\mu_0 \omega_0^2}{2k} P \exp\left(i \Delta k z\right), \tag{2.22}$$

where we also assume that the wave travels along the z-direction. If the fundamental wave and the generated wave are travelling at different phase

velocities, the energy cannot be transferred efficiently, actually, energy from the induced wave can go back into the fundamental wave. This is described by the phase-mismatch:

$$\Delta k = k_0 - k_P, \tag{2.23}$$

where k_P is the wavevector of the induced field. Equation 2.22 can easily be integrated and the field after propagating through a nonlinear crystal of length L is given by:

$$E(L,t) = -i\frac{\mu_0\omega_0^2}{k_0} PL \ \exp(i\Delta kL/2)\ \mathrm{sinc}(\Delta kL/2) \tag{2.24}$$

from which we get the intensity of the induced field:

$$I(L,t) = \frac{c\mu_0\omega_0^2}{4}\,|P|^2\,L^2\,\mathrm{sinc}^2(\Delta kL/2), \tag{2.25}$$

From Equation 2.25 we see that the intensity of the induced field is proportional to L^2, λ^{-2} and is peaked around $\Delta k = 0$. For collinear second harmonic generation, the intensity is also proportional to the square of the fundamental intensity and the phase-matching condition can be written as:

$$n(\omega_1) = n(2\omega_1). \tag{2.26}$$

Since all media are dispersive, i.e. the refractive index varies with wavelength, this condition is usually not met. One way of bypassing dispersion is by using a birefringent crystal, where the refractive index is different for different axes. The phase-matched wavelength region can be tuned by cutting a birefringent crystal at a specific angle, such that the resulting refractive index (the projection along the two-axes) meets Equation 2.26. The refractive index for a birefringent crystal cut at an angle θ can be calculated as:

$$n_e(\theta) = \frac{n_e\ n_o}{\sqrt{n_o^2\sin^2\theta + n_e^2\cos^2\theta}}, \tag{2.27}$$

where $n_{e,o}$ are the refractive indices of the ordinary and extraordinary axes. For broadband phase-matching, it not possible to keep Δk small over the whole spectral range. But, by keeping the interaction length short, the second harmonic and the fundamental don't have 'time' to drift apart, leading to second harmonic generation over a broad spectrum. This is described by L in the argument of the sinc-function in Equation 2.25. For ultrabroadband pulses, spanning more than 200 nm in the Near Infra-Red (NIR), thin crystals, typically a few tens of microns long, are used.

2.1.4.2 Self Phase Modulation

The effect of a nonlinear refractive index n_2 in space, as discussed earlier (see Figure 2.7), also has an effect in the time and spectral domain. The temporal distribution of the pulse leads to a time-dependent refractive index. Thus the temporal phase changes with time and the instantaneous frequency, $\omega(t) = \mathrm{d}\phi/\mathrm{d}t$ becomes time dependent (i.e. *chirped*). The phase term after going through a nonlinear medium with length L is given by (using Equation 2.18):

$$\phi = \omega_0 t - \frac{2\pi}{\lambda_0} n(I,t)L = \phi_{\text{lin}} - \frac{2\pi}{\lambda_0} n_2 I(t)L, \tag{2.28}$$

where ϕ_{lin} is the phase given for a linear medium with $n_2 = 0$. This leads to an instantaneous frequency of:

$$\omega(t) = \frac{\mathrm{d}\phi}{\mathrm{d}t} = \omega_0 - \frac{\omega_0 L}{c}\frac{d}{dt} n(I,t) = \omega_0 - \frac{\omega_0 L}{c} n_2 \frac{d}{dt} I(t). \tag{2.29}$$

The shift in frequency is proportional to the length of the medium and the rate of change of the pulse intensity. A pulse will thus show a red-shift at the rising edge of the pulse and a blue-shift for the falling edge $\rightarrow$, i.e. the pulse will be chirped. Note that, since a Gaussian beam profile is most intense in the centre, the central part of the pulse will be spectrally broadened more

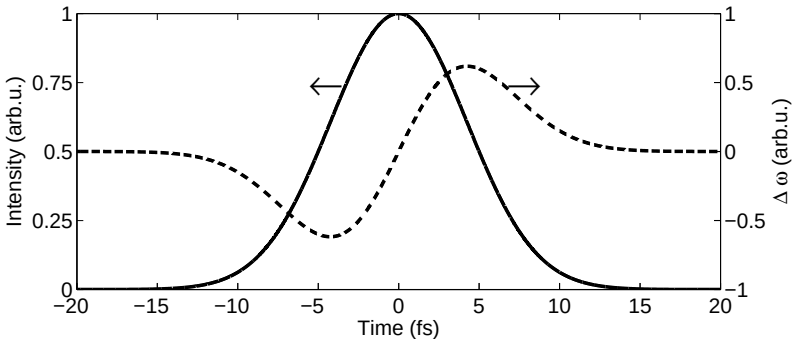


Figure 2.8: The frequency shift induced by self-phase modulation for a Gaussian pulse. The leading-edge is red- and the trailing edge blue-shifted.

than the outer part after travelling through the medium. The evolution of the spectral broadening can be calculated by taking the input pulse in the temporal domain, adding the phase factor from Equation 2.28 and Fourier-transforming it to the spectral domain:

$$E(t) \xrightarrow{\text{SPM}} E(t) \times \exp\left(i\frac{2\pi}{\lambda_0} n_2 I(t) L\right) \xrightarrow{\mathcal{F}} A(\omega) e^{i\phi(\omega)}.$$

Since it only changes the phase in the temporal domain, the pulse duration is not altered. Nevertheless, in a normal dispersive medium, where the 'red' portions of the pulse are faster, than the 'blue' ones, the pulse will become longer, as the front of the pulse is faster, than the trailing edge. Therefore, after propagating through the nonlinear medium, the pulse has to be compressed again. The frequency shift, $\Delta\omega = \omega(t) - \omega_0$, for a Gaussian pulse due to the self-phase modulation is shown in Figure 2.8. This shift is approximately linear around the centre of the pulse ($t = 0$), indicating a constant group delay dispersion. Because the spectrum is now broader than before, the pulse can be compressed to a pulse duration shorter than before simply by introducing negative dispersion.

The damage threshold for the nonlinear medium ($\sim 10^{13}\,\mathrm{Wcm}^{-2}$ [34]) puts

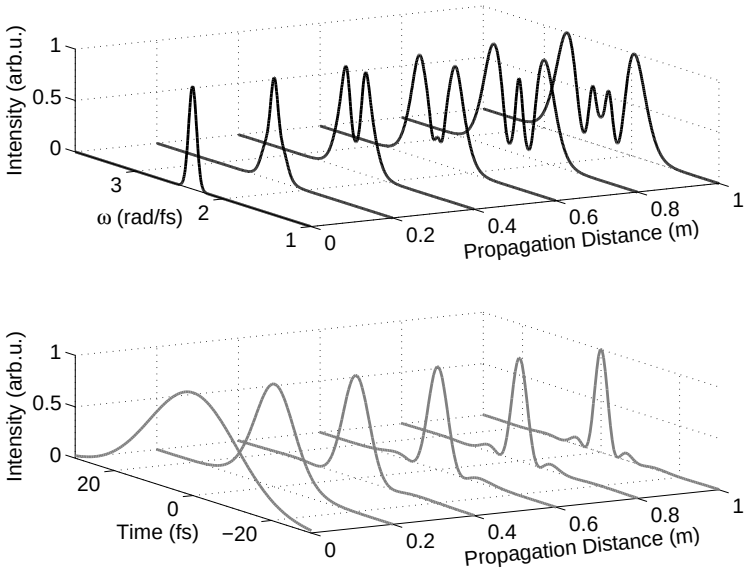


Figure 2.9: Top: Spectral broadening due to self-phase modulation (SPM) inside a nonlinear medium for different propagation lengths. **Bottom:** The resulting transform-limited pulse. Note: The transform-limited duration can only be obtained by removing the phase induced by SPM. Without chirp-compensation, the pulse-duration actually does not change.

a limit on the peak intensity, preventing the use of single mode fibres [35, 36] and photonic crystal fibres [37, 38]. In addition other nonlinear effects, such as self-focusing, make self-phase modulation hard to control in solid material. For high powers, hollow-core fibres filled with gases are typically used [39]. They allow for higher powers since the nonlinear medium is a gas, which cannot be damaged, as well as long and intense interaction regions due to wave-guiding. Depending on the laser power, gas species and pressure used, ionisation effects can still play a role, especially at the entrance of the hollow fibre. By using a differentially pumped setup, where the front gas pressure is kept to a minimum and the pressure rises along the fibre, the ionisation

effects become less severe and higher pressures can be used leading to more spectral broadening [39].

2.1.5 Hollow Fibre

The use of hollow-core fibres as waveguides for long distance optical transmission was first studied by Marcatili and Schmeltzer at Bell Labs in 1964 [40]. Since the transmission degrades rapidly over long distances (10s of meters), this idea was quickly put aside. Nevertheless, the transmission of a hollow fibre over the order of 1 m is acceptably high ($> 50\%$) for use in high-power laser systems. Hollow fibres have since been used for spectral broadening and short pulse generation [41] or efficient high harmonic generation [42]. Propagating a small beam over a large distance increases the nonlinear effects substantially compared to the Rayleigh range for a beam focused without a waveguide.

2.1.5.1 Modes

Wave propagation along a hollow fibre can be thought of in terms of grazing incidence reflections. There are three different types of modes that are supported by a hollow fibre with the internal diameter much larger than the propagating wavelength: transverse circular electric (transverse circular magnetic) modes with their electric (magnetic) field component tangential to the guide and the magnetic (electric) components axial as well as radial, and hybrid modes (EH_{pm}), where all components are present, but axial components are so small that they can be treated as transverse modes [43]. For fibre diameters large compared to the laser wavelength, hybrid modes can be treated as linear polarised and thus efficiently couple to the incoming beam. Therefore, in the case of a fused silica hollow fibre filled with gas, the only

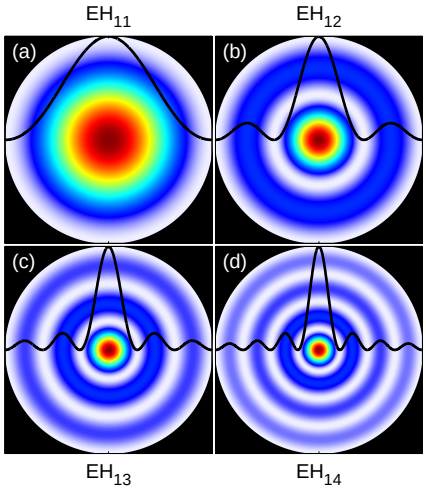


Figure 2.10: The radial intensity distribution of the four lowest order propagation modes in a gas-filled hollow fibre.

modes that can efficiently couple into the fibre and thus have the lowest attenuation are the low order hybrid modes [44, 45]. The intensity profile of these modes is given by [46]:

$$I_m(r) = I_m(0) J_0^2 \left(u_{1m}\, r/a\right), \tag{2.30}$$

where J_0 is the zeroth order Bessel function of the first kind, a the inner radius of the hollow fibre and u_{1m} is the m^{th} root of J_0. The intensity distribution for the first four hybrid modes is shown in Figure 2.10.

The attenuation along the fibre is different for each of these modes and is described by the imaginary part of the propagation constant α_m. The attenuation after propagating along z is then given by [47]:

$$I_m(r, z) = I_m(r, 0)\, \mathrm{e}^{-\alpha_m z}, \tag{2.31}$$

with the propagation constant given by:

$$\alpha_m = \left(\frac{u_{1m}}{2\pi}\right)^2 \frac{\lambda^2}{2a^3} \frac{\nu^2 + 1}{\sqrt{\nu^2 - 1}}, \tag{2.32}$$

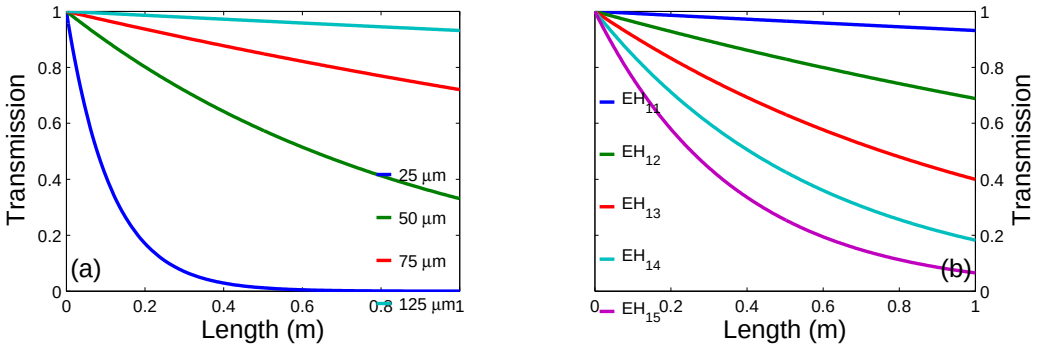


Figure 2.11: Theoretical transmission for a hollow fibre as a function of fibre length. (a) Transmission of the fundamental mode, EH_{11}, at $\lambda = 800\,\text{nm}$ for different fibre diameters.
(b) Transmission for different modes with a fixed radius, $a = 125\ \mu\text{m}$, as a function of hollow fibre length.

where ν is the ratio between the refractive indices of the fused silica and the gas in the hollow fibre. The $1/a^3$ dependenca of α_m shows that the losses can be dramatically decreased by increasing the radius of the hollow fibre. This is shown in Figure 2.11. But for the purpose of spectral-broadening through self-phase modulation, the guided intensity ($\propto 1/a^2$) is critical and therefore a compromise between intensity and losses has to be found. Equation 2.32 also shows that the attenuation is larger for higher order modes, favouring the propagation of the EH_{11} mode.

2.1.5.2 Coupling

In addition to the attenuation along the fibre, the coupling into the hollow fibre is crucial for ensuring efficient transmission. The laser mode has to be matched to the excited mode in the hollow fibre. The power coupled into the fibre-modes, P_m, can be calculated in a similar way to coupling into an

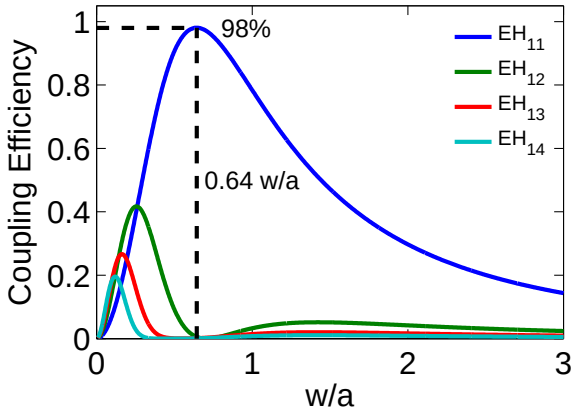


Figure 2.12: Theoretical coupling efficiency of a Gaussian beam into the first four hybrid modes as a function of the normalized beam waist w/a, where w is the radial width of the optical intensity at $1/e^2$ and a is the radius of the hollow fibre. Note that the overall transmission of the fibre will be less due to propagation effects.

optical fibre [48]:

$$P_m = \int\int \vec{E}_\mathrm{i} \times \vec{H}_\mathrm{f} \cdot \vec{e_z}\, \mathrm{d}S, \tag{2.33}$$

where $\vec{E}_\mathrm{i}$ is the incident electric field, $\vec{H}_\mathrm{f}$ the magnetic field of the excited fibre mode, z the direction of the fibre and $\mathrm{d}S$ the elementary fibre transverse section. Assuming a Gaussian incident electric field linearly polarised along x:

$$\vec{E}_\mathrm{i} = E_0 \exp(-r^2/w^2)\vec{e_x}$$

and coupling into the hybrid modes EH_{1m} this integral can be solved. For the electric field of a hybrid mode polarised in x-direction, the magnetic field is given by (see also Equation 2.30):

$$\vec{H} = H_0 J_0\left(u_{1m}\right) \vec{e_y}.$$

The coupling efficiency for the different modes, $\eta_m = P_m/P_m^{\text{in}}$, can then be calculated by [49]:

$$\eta_m = \frac{4\left[rJ_0\left(u_{1m}\right)\exp\left(-r^2/w^2\right)\mathrm{d}r\right]^2}{\omega^2\int_0^a rJ_0^2\left(u_{1m}\right)\mathrm{d}r}. \tag{2.34}$$

In Figure 2.12 I have calculated the coupling of a Gaussian beam into the first four hybrid modes. Maximum coupling into EH_{11} is achieved for a Gaussian beam with a waist:

$$\boxed{w_{\text{max},1/e^2} = 0.64\ a}, \tag{2.35}$$

where the radius of the waist is given by the width at $1/e^2$ and a is the radius of the fibre. For this beam size, 98% is coupled into the fundamental mode, $\sim 1\%$ is lost in the coupling and less than 1% is coupled into all of the higher order modes. This, in addition to the attenuation of higher order modes as seen in Figure 2.11, leads to a very good mode discrimination and therefore a very clean beam profile after propagation through a hollow fibre.

2.1.6 Dispersion Compensation

As discussed in subsection 2.1.2, short optical pulses change their temporal profile due to group velocity dispersion, when going through material. Every laser has intra-cavity components and the pulse undergoes positive dispersion typically in the gain medium and when going through the output coupler. For ultrashort pulses the air-path itself introduces significant dispersion. Therefore, we need optical setups to reverse dispersion effects, namely setups that introduce negative dispersion. But this is not only important for intra-cavity compensation. In chirped pulse amplification there is a need to stretch and re-compress an optical pulse in order to keep the pulse intensity

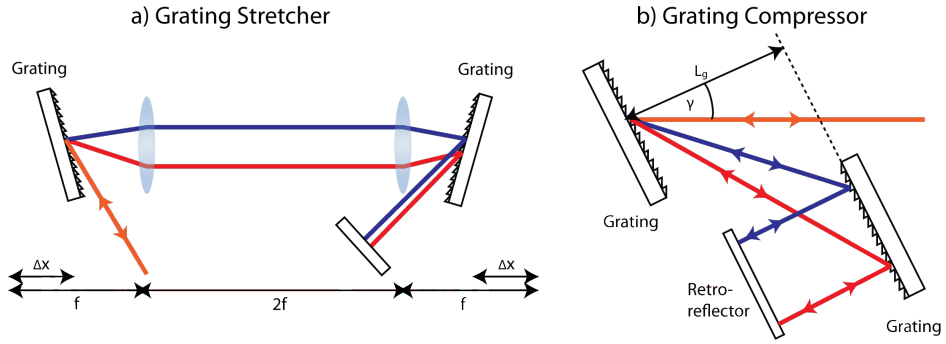


Figure 2.13: Schematic diagrams of (a) a pulse stretcher and (b) a pulse compressor.

low during the amplification step [50], hence measures are needed that can also stretch the pulse using positive dispersion.

Dispersion compensation is usually done by spectrally dispersing the beam and altering the optical path for each wavelength by using prisms or gratings. Another way is using specially designed dielectric mirrors, called chirped mirrors, in which the red part of the spectrum gets reflected at a deeper surface then the blue part [51].

2.1.6.1 Grating Compressors

In 1969 it was shown by Treacy that two identical parallel gratings can be used to introduce a negative dispersion [52]. In Figure 2.13 b) it is straight forward to see, that in this setup the optical path is longer for long wavelengths. The phase of the grating compressor for a single pass can then be calculated to be [53]:

$$\phi_g(\omega) = \frac{2\omega L_g}{c}\left[1 - \left(\frac{2\pi c}{\omega d} - \sin\gamma\right)^2\right]^{1/2}, \tag{2.36}$$

where d is the grating period and L_g and γ are defined in Figure 2.13 b. Usually a mirror is put at the end of the compressor and the beam is retro-

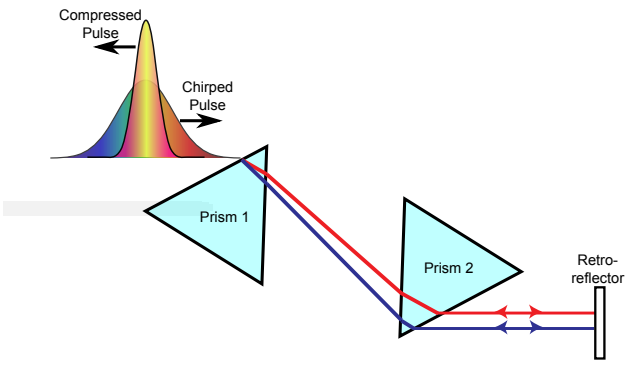


Figure 2.14: A prism pair setup to compensate for group velocity disperison. The blue part of the spectrum is refracted more than the red part. This means that the overall optical path length is longer for the red part resulting in a negative dispersion.

reflected for a second pass to compensate for the spatial chirp, i.e. the spatial walk-off for different wavelengths. With a similar optical setup one can also introduce the exact opposite dispersion, making it a perfectly matched stretcher for a CPA laser. One way of doing this is shown in Figure 2.13 a). Here, the first and the second gratings are anti-parallel and at a distance $s < f$ away from the first and second lens, respectively. The two identical lenses themselves are separated by $2f$. Therefore the second grating is located before the imaging plane, leading to a longer optical path for the blue part of the spectrum and therefore a positive chirp.

2.1.6.2 Prism Compressors

The use of prism pairs for dispersion compensation was first introduced in the mid-eighties [54, 55]. An arrangement is shown in Figure 2.14. Here the beam gets spectrally dispersed in the first prism, leading to different paths for different wavelengths. The optical path P depends on the input angle and the separation l between the prisms. A prism compressor with SF18 prisms,

Table 2.5: Centre wavelength $\lambda = 800\,\text{nm}$, Grating compressor with 600 lines/mm, AOI= 15°, L_g =5 cm. Prism compressor with Brewster angle, minimum deviation for SF18 and distance tip-to-tip 10 cm, AOI = 59.61°, prism angle: 60.78°

Optical Element	GVD [fs^2]	TOD [fs^3]	FOD [fs^4]
Grating Compressor	-1751	836	-419
Prism Compressor	-837	-684	-237
Fused Silica (1cm)	362	275	-115
BK7 (1cm)	223	54	-4.6
SF18 (1cm)	772	161	10.0
Sapphire (1cm)	291	71	-6.7
Air (1m)	10.6	1.7	0.05

a separation of $l = 10\,\text{cm}$ and pulse at a centre wavelength $\lambda_0 = 800\,\text{nm}$ will introduce a negative dispersion of $-837\,\text{fs}^2$ (see Table 2.5 for more details).

Compared to gratings, prism compressors, when used in a Brewster geometry, allow for better power transmission compared to diffractive gratings. On the other hand, the production of larger prism pairs (larger than a few centimetres) gets exponentially more expensive, their use is limited to CPA systems with energies around 1 mJ due to nonlinear effects in the glass prisms.

2.1.6.3 Chirped Mirrors

Chirped mirrors are dielectric mirrors which are used to compensate material dispersion [51]. Essentially all few-cycle pulses from ultra-broadband systems in the NIR are compressed using chirped mirrors. They can be designed to have a very large bandwidth and are straightforward to use. Chirped mirrors

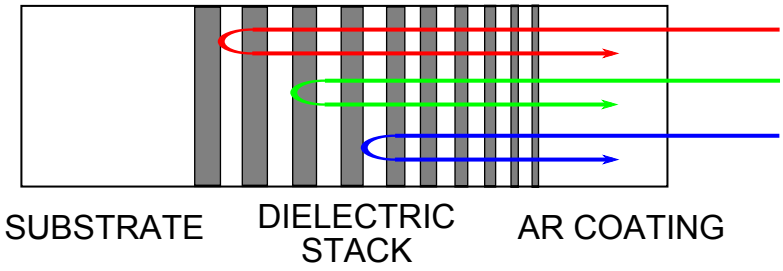


Figure 2.15: A schematic of a double-chirped mirror.

consist of different layer thicknesses such that the Bragg wavelength changes as a function of penetration depth. Thus different wavelengths travel different lengths within the substrate and the pulse is chirped. This picture results in chirped mirrors that show a strong oscillatory behaviour in their group delay. These oscillations are due to an interference of the partial reflection of the first layer with the reflection of the back of the mirror, thus creating an effective Gires-Tournois interferomter. This effect can be eliminated by the use of double chirped mirrors [56] which have *chirped* high-index layers, i.e. the thickness of the high index layers is steadily increased from layer to layer. In addition an anti-reflective coating on the front of the mirrors further reduces this effect.

In practice, doubly chirped mirrors still show some oscillations. These can be compensated for by using pairs of chirped mirrors such that the overall group-delay is flat over the whole desired spectrum. Additional fine-tuning is provided by tweaking the angle-of-incidence.

2.1.7 Carrier-Envelope Phase

The CEP is defined as the offset between the optical phase of the pulse-carrier with respect to the maximum of the pulse-envelope (defined as ϕ_0 in Equation 2.1). In the few-cycle regime, i.e. when the envelope of the

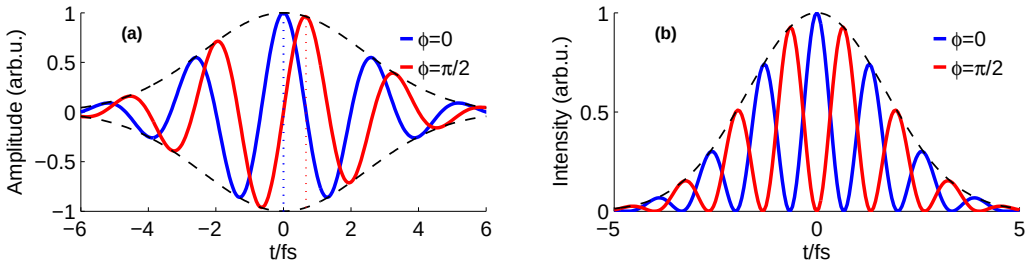


Figure 2.16: The electric field (a) and intensity (b) of a $\tau_{\mathrm{FWHM}} = 2.7\,\mathrm{fs}$ pulse centred at 800 nm for two different CEP values, namely $\phi_0 = 0$ (blue) and $\phi_0 = \pi/2$ (red). One can see that the maximal instantaneous intensity is different in each case.

pulse is of the duration of only a few optical cycles, this parameter is very important. Here, the waveform of the instantaneous electric field is strongly dependent on the CEP. In Figure 2.16 the electric field and intensity for a few-cycle pulse for two different CEP values is shown. The case of $\phi_0 = 0$, often referred to as a *cosine*-pulse, has one distinct maximum in the electric field that has the same value as the maximum of the electric field envelope. The $\phi_0 = \pi/2$ case is called a *sine*-pulse and there are two equal peaks in the electric field which are smaller than the peak of the envelope and are of opposite direction.

This difference in peak amplitude is most pronounced when comparing *cosine*- with *sine*-pulses and gets less and less for longer pulse durations. They can differ by as much as 15% for a few-cylcle (2.7 fs) pulse but only by $< 0.5\%$ in the many-cycle regime ($\gtrsim 20\,\mathrm{fs}$ pulse), as shown in Figure 2.17.

2.1.7.1 Measuring and Controlling CEP

The CEP of a mode-locked oscillator arises from a difference of the group- and phase-velocities within the cavity. To understand how this phase evolves

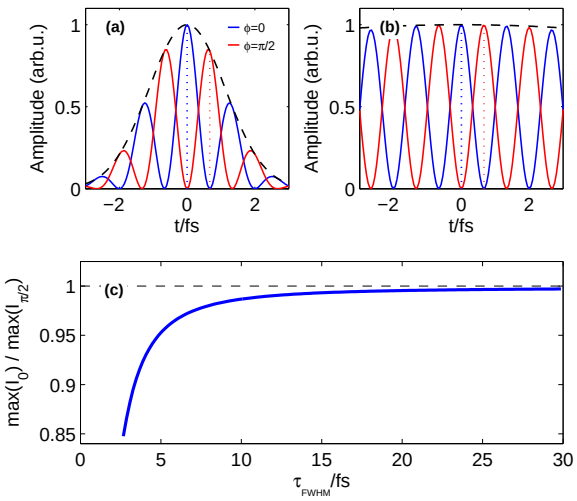


Figure 2.17: The instantaneous intensity of a few-cycle pulse (a) with a FWHM duration of 2.7 fs and a many-cycle pulse with a duration of 25 fs (b) are shown with a CEP of $\phi_0 = 0$ (blue) and $\phi_0 = \pi/2$ (red). The ratio of the peak intensities is shown in (c). This ratio quickly converges to 1 for many-cycle pulses.

and how one can measure it, it is important to understand the connection of the time-domain with the spectral-domain description.

Since the electric field of a pulsed laser is periodic in time, with a period $T = 1/f_{\mathrm{rep}}$, the spectrum consists of a comb of discrete frequencies, each spaced by the repetition rate f_{rep}. They can therefore be written as:

$$f_n = n f_{rep} + f_0, \tag{2.37}$$

where n is a large number and f_0 is the comb offset that arises from a pulse-to-pulse phase-shift $\Delta\phi$, also called CEP slip. These two measures are connected by the following relation [57]:

$$f_0 = \frac{1}{2\pi} f_{\mathrm{rep}} \Delta\phi. \tag{2.38}$$

A difference in phase- and group-velocity inside the laser cavity causes the

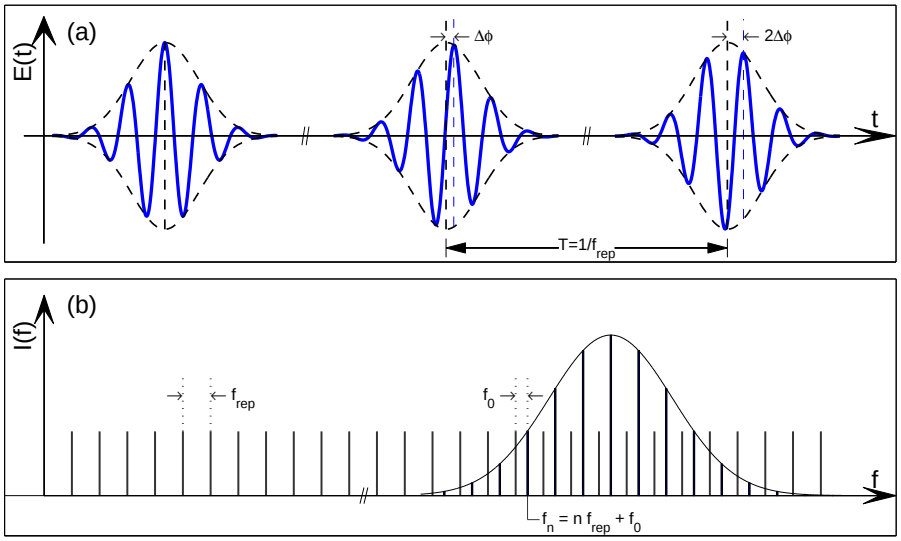


Figure 2.18: A modelocked oscillator in the time (a) and spectral (b) domain. (a) The CEP of consecutive pulses changes as the carrier slips under the envelope due to differences in group- and phase-velocity. (b) The frequency comb is spaced by f_{rep} and the entire comb is offset from zero by $f_0 = f_{\mathrm{rep}}\Delta\phi/2\pi$.

pulse-to-pulse phase-shift for consecutive pulses. The carrier therefore slips under the envelope during one roundtrip and each pulse can have a different CEP. Keeping this in mind, $\Delta\phi$ can be rewritten in terms of dispersion as:

$$\Delta\phi = \left(\frac{1}{v_g} - \frac{1}{v_p}\right) L_c\, \omega_c \mod 2\pi, \tag{2.39}$$

where v_g and v_p are the mean group- and phase-velocities inside the cavity, L_c the cavity length and ω_c the carrier-frequency. Figure 2.18 summarises the relations of the time and spectral domain and show how the CEP evolves for consecutive pulses.

The CEP value in a Chirped Pulse Amplification (CPA) system can be locked. By locking the shift to a multiple of the laser repetition, $f_0 = f_{\mathrm{rep}}/n$, it is assured that every n^{th} pulse in the train has the exact same CEP value. Although in principle, f_0 could be measured by comparing one of the combs

frequency lines to an external frequency like an atomic transition, in practice it is much easier to use a self-referencing method. This is usually done with an f-to-$2f$ interferometer [58, 59]. Here, an octave spanning bandwidth is needed in order to compare the blue part of the spectrum with the second harmonic of the red part. This will lead to a beat note between the fundamental and the frequency-doubled comb lines, leading to:

$$f_{\text{beat}} = 2f_n - f_{2n} = 2(nf_{\text{rep}} + f_0) - (2nf_{\text{rep}} + f_0) = f_0 \tag{2.40}$$

where f_n is the fundamental and f_{2n} the second harmonic beam. Since the output of an oscillator is usually not octave-spanning, the spectrum needs to be broadened first. This can be done by creating a supercontinuum with the use of of a photonic-crystal fibre (PCF) or, if there is enough power, via white-light generation in a bulk material [60, 61].

One implementation is shown in Figure 2.19. Here the oscillator pulse is first broadened in a PCF and then a dichroic mirror splits the long and short wavelength part of the spectrum. The long part gets frequency doubled in a crystal that is cut to phase-match the long wavelength edge of the spectrum. The short wavelengths can be delayed in time by a pair of prisms and both arms are collinearly recombined afterwards. A grating spectrally disperses the beam in order to overlay the second harmonic signal with the corresponding frequency of the spectrally broadened short wavelength arm. The beat frequency is picked up by a fast avalanche diode and can be maximized by equalising the power in each beam with the $\lambda/2$ plates. Another diode picks up the repetition rate of the oscillator to be able to lock the phase-slip, $\Delta\phi$, such that every n^{th} pulse has the same CEP as has been first demonstrated in the early 2000s [62, 63].

With the methods discussed before, the absolute CEP cannot be measured, but only locked arbitrarily and then changed by a known amount

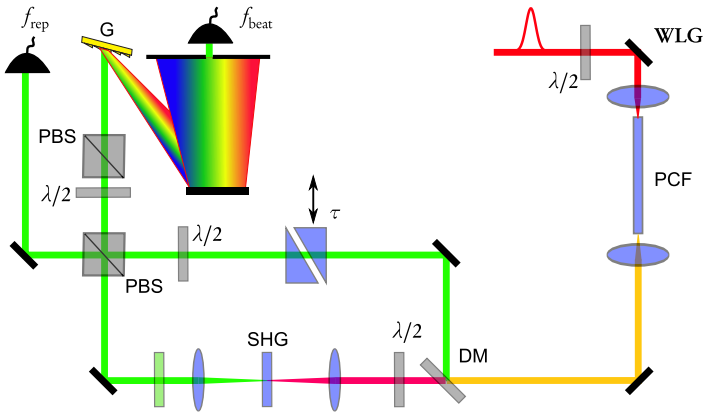


Figure 2.19: A schematic of a typical f-to-2f-interferometer setup for measuring the CEP slip of an oscillator. The input pulse is spectrally broadened to an octave spanning spectrum in a PCF and split into a long and short wavelength arm by a dichroic mirror (DM). The longer wavelengths get frequency doubled in a crystal (SHG) and then co-linearly recombined with the short wavelengths by a polarising beam splitter (PBS). The grating (G) disperses the spectra and the beat signal is detected by an avalanche photodiode.

afterwards. To directly measure the absolute CEP of a laser pulse, different methods have to be used that exploit strong-field phenomena sensitive to CEP. There have been various methods that achieve an absolute measure of the CEP, like Stereo-ATI [64–66], photoemission from metals [67], terahertz-emission [68] and half-cycle cutoffs in high-harmonic generation [69].

2.1.8 Femtosecond Pulse Measurements

With light pulses approaching durations of a few femtoseconds in the NIR it is getting more and more challenging to measure them. Even the fastest electronic detectors are not fast enough to measure pulses in the femtosecond regime. The only thing that is fast or rather short enough is the pulse itself or another pulse shorter or of the same duration as the pulse to measure. In

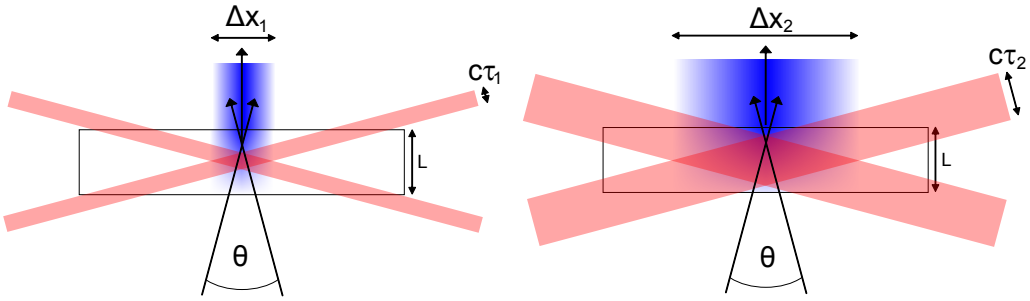


Figure 2.20: Single shot autocorrelation principle for a short (left) and a long (right) pulse. The width of the pulse is mapped onto the spatial coordinate and a pulse length can be deduced by calibrating the relationship between t and x. Figure adapted from [70]

this section I will present methods that can characterize pulses especially in the few-cycle regime. First I will present autocorrelation. Here the pulse is crossed with itself and a nonlinear response is measured. Secondly FROG, another more precise method, is discussed. Here one spectrally resolves the autocorrelation signal and can then reconstruct the pulse with an iterative algorithm. Lastly I will discuss SPIDER, a method based on spectral interferometry between two spectrally-sheared pulses.

2.1.8.1 Intensity Autocorrelation

Autocorrelation is one of the oldest techniques for short pulse measurements [71]. Here a beam is split into two identical beam replicas. They are then combined in a nonlinear medium, usually a nonlinear crystal with sufficient transparency and phase-matching bandwidth to allow second-harmonic generation of the full laser bandwidth. The autocorrelation signal, i.e. the intensity of the second harmonic beam, is given by:

$$I_{\mathrm{AC}}(\tau) = \int_{-\infty}^{\infty} I(t)\, I(t-\tau)\, \mathrm{d}t, \tag{2.41}$$

where τ is the time delay between the two beams. When the time delay between the two replicas is such that they overlap at the crystal, light with twice the frequency is emitted in the center direction. After measuring the FWHM of the autocorrelation a deconvolution factor has to be applied for specific pulse shapes. For a sech-shaped pulse the autocorrelation width Δt_{AC} and the real pulse width Δt are related by: $\Delta t = \Delta t_{\mathrm{AC}}$ / 1.55. For a Gaussian pulse $\Delta t = \Delta t_{\mathrm{AC}}/1.41$.

A time delay can either be achieved by a delay stage or, for single shot measurements, the two beams are crossed at an angle θ as is shown in Figure 2.20. The time delay is then mapped into a spatial coordinate x by:

$$x = \frac{c\,\tau}{2\,\sin(\theta/2)}, \tag{2.42}$$

where τ again is the time delay between the two pulses and θ is the crossing angle of the two beams. Especially for high repetition rate lasers, a single shot geometry is easier to implement then a delay stage, since no scanning of the delay is required during the measurement. In a single shot setup, a delay stage is only used to calibrate the time axis, but does not need to be moved during the measurement.

As can be seen from Equation 2.41, with an autocorrelation measurement one only gets information about the intensity and not the phase, which for ultrashort pulses ($< 15\,\mathrm{fs}$) usually is not sufficient, since the phase can significantly change the shape of the pulse. Other methods such as SPIDER or FROG offer a full phase retrieval of the pulse and are therefore commonly used for the measurement of ultrashort laser pulses, especially in the few-cycle regime.

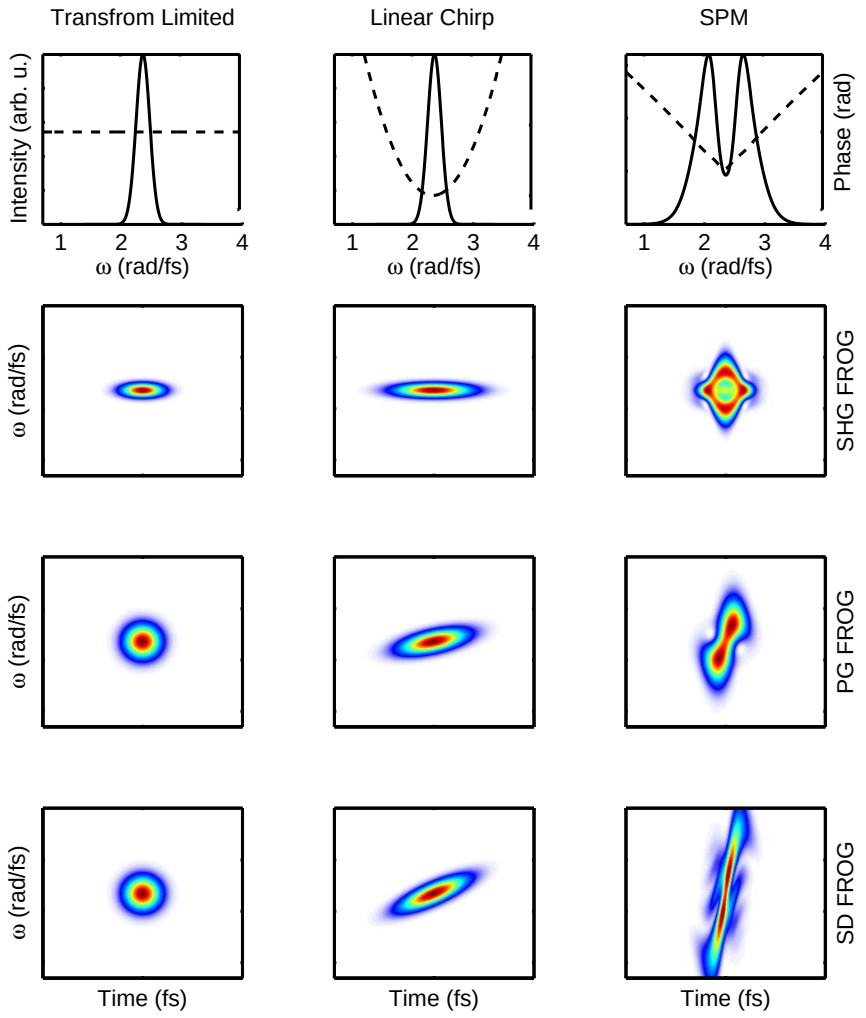


Figure 2.21: FROG traces for different beam geometries and common pulse distortions. Both PG- and SD-FROG show the sign of the linear chirp, whereas the SHG-FROG only stretches the trace in the time domain. It also shows that SD-FROG is more sensitive to a chirp, in fact the slope for a linearly chirped pulse is twice the slope of the PG-FROG trace [72].

Left column: laser pulse centred at 800 nm and a pulse duration of 10 fs.

Middle column: same pulse as left column but linearly chirped by 60 fs^2.

Right column: same pulse as left column but self-phase modulated*

$* : \phi_{\mathrm{SPM}} = \frac{\omega}{c} \left|E(t)\right|^2 / \left|E_{\max}\right|^2 \; n_2 \; L = \mathbf{4} \; \left|E(t)\right|^2 / \left|E_{\max}\right|^2$

2.1.8.2 FROG

Frequency-Resolved Optical Gating (FROG) is a common technique used to characterise optical pulses and can even be used to measure sub-femtosecond pulses [73]. A FROG measurement is essentially a spectrally-resolved autocorrelation measurement. There are many different beam geometries that exploit a nonlinear effect to achieve an autocorrelation and then use a two dimensional spectrometer to look at the spectrum for different time delays [74–76].

The FROG signal recorded is given by [76]:

$$I_{\mathrm{FROG}}(\omega,\tau) = \left| \int_{-\infty}^{\infty} E(t)\; g(t-\tau) e^{-\mathrm{i}\omega t}\, \mathrm{d}t \right|^2, \tag{2.43}$$

where $g(t-\tau)$ is a gate function that is specific for different FROG geometries. For a Polarisation Gated FROG (PG-FROG) the gate function is given by $|E(t-\tau)|^2$, yielding:

$$I_{\mathrm{FROG}}(\omega,\tau) = \left| \int_{-\infty}^{\infty} E(t)\; |E(t-\tau)|^2\, e^{-\mathrm{i}\omega t}\, \mathrm{d}t \right|^2. \tag{2.44}$$

The gate function here is real and therefore does not add any phase information to the signal. Therefore the trace is quite intuitive in contrast to the most commonly used geometry to characterize few-cycle pulses, a SHG-FROG [76]. Just like in the SHG-autocorrelation setup discussed in the previous section, in SHG-FROG two replicas of the pulse to be measured are combined in a frequency-doubling crystal. The autocorrelation signal is then spectrally resolved as a function of the time delay between the two pulses to create a so-called FROG-trace. The setup of our SHG-FROG is shown in Figure 4.1. In a SHG-FROG the gate function is given by $E(t-\tau)$ leading to an overall signal of [77]:

$$I_{\mathrm{FROG}}(\omega,\tau) = \left| \int_{-\infty}^{\infty} E(t)\; E(t-\tau) e^{-\mathrm{i}\omega t}\, \mathrm{d}t \right|^2. \tag{2.45}$$

The phase contribution of the gate leads to more unintuitive traces. In addition, from Equation 2.45 it can be seen that the SHG-FROG trace is symmetric in time leading to ambiguities in the pulse retrieval algorithm. Therefore, for example it is not possible to distinguish a post-pulse from a pre-pulse. In practice it is quite easy to resolve these ambiguities e.g. by adding a known amount of GDD, like a thin piece of glass, into the beam and taking a second measurement. Another problem with the SHG-FROG measurements is the retrieval algorithm. Since the trace is rather unintuitive, and it can not be directly inverted into a pulse profile an iterative algorithm has to be used and real-time measurements of the pulse are not possible. The main advantages of SHG-FROG are the very broad bandwidth that can be supported by thin crystals and its sensitivity. The single-shot geometry is easily setup and there is less of a background problem as the probed replica of the pulse are not co-propagating with the signal beam and the spectrometer differentiates between the fundamental and second harmonic beam. Some traces for different beam geometries for a range of phase distortions are shown in Figure 2.21

Great care has to be taken in finding a nonlinear crystal with a broad enough phase-matching bandwidth. In our FROG setup we use a 5 µm thin BBO crystal cut at 43° to allow for a broad phase-matching from 500-1000 nm (see section 4.1). But not only the crystal has a specific bandwidth and therefore a spectral response. In most cases, the mirrors used after the SHG crystal as well as the two-dimensional spectrometer do not have a constant wavelength response.

There are possible consistency checks in a FROG measurement. First, the spectral marginal of the FROG trace, which is the projection onto the wavelength axis, can indicate problems in the bandwidth response. By ob-

taining an independent spectral measure one can calculate the marginal and compare it with the FROG trace. The spectral marginal is given by [72]:

$$S(\omega) = \int_{-\infty}^{\infty} I(\omega)\ I(\omega' - \omega)\mathrm{d}\omega'. \tag{2.46}$$

A wavelength dependent correction factor can then be applied to match the measured marginal to the calculated one and therefore analytically correct for a non-flat spectral response [78, 79].

2.1.8.3 SPIDER

Another way of measuring the amplitude and phase of ultrashort pulses is using spectral phase interferometry for direct electric field reconstruction (SPIDER) [80]. This technique is based on spectral interferometry (SI) between two spectrally-sheared pulses. In the standard SPIDER setup shown in Figure 2.22, the pulse is reflected by an etalon, producing two identical pulses that are delayed with respect to each other by a time τ. The transmitted pulse, called the ancilla, is usually stretched either by a grating-stretcher or a block of glass by an amount mainly determined by the second order phase $\phi^{(2)}$ (see Equation 2.8). All three pulses are then combined onto a nonlinear crystal where the delayed replica upconvert with different parts of the stretched pulse. Due to the large stretching of the ancilla and the short duration of the pulses to be measured, this upconversion can be thought of as upconversion with two different monochromatic frequencies. The resulting spectra are therefore spectrally sheared by Ω. The amount of the shear depends on the chirp and time delay: $\Omega = \tau/\phi^{(2)}$. The two upconverted beams

are then interfered with each other to yield an interferogram given by [80]:

$$S(\omega) = \left|E(\omega+\omega_0) + E(\omega+\Omega+\omega_0)\, e^{i\omega\tau}\right|^2 \tag{2.47}$$

$$= \left|E(\omega_1)\right|^2 + \left|E(\omega_2)\right|^2 + 2\,|E(\omega_1)|\,|E(\omega_2)|\,\cos\left(\delta\phi(\omega)+\omega\tau\right), \tag{2.48}$$

where $\omega_1 = \omega + \omega_0$ is the first upconverted frequency, $\omega_2 = \omega + \Omega + \omega_0$ the second upconverted frequency and $\delta\phi(\omega) = 1/\Omega(\phi(\omega+\Omega+\omega_0) - \phi(\omega+\omega_0))$ the phase difference between those two fields. The first two term of this equation are simply the individual upconverted spectra. The phase information is contained in the cosine modulation of the third term. The phase difference can be reconstructed using Fourier-transform spectral interferometry (FTSI) [81]. This can be seen by using $A_{\mathrm{dc}}(\omega) = |E(\omega_1)|^2 + |E(\omega_2)|^2$ and $A_{\mathrm{ac}}(\omega)e^{i\omega\tau} = |E(\omega_1)||E(\omega_2)|e^{i\delta\phi(\omega)}$ and rewriting Equation 2.48 as:

$$S(\omega) = A_{\mathrm{dc}}(\omega) + A_{\mathrm{ac}}(\omega)e^{i\omega\tau} + c.c. \tag{2.49}$$

Fourier transforming this yields:

$$S(t) = A_{\mathrm{dc}}(t) + A_{\mathrm{ac}}(t-\tau) + A^*_{\mathrm{ac}}(t+\tau). \tag{2.50}$$

Hence, there are three peaks in the Fourier domain (if the SPIDER is set up correctly with a time delay large enough to lead to distinct peaks). The phase information is contained in the ac-peaks. Filtering around $t = \tau$ and applying an inverse Fourier transformation reconstructs the total phase, $\delta\phi(\omega) + \omega\tau$, of the last term in Equation 2.48. The linear term $\omega\tau$ and the frequency shift (from upconversion) are then removed to yield the phase-difference $\delta\phi(\omega) = 1/\Omega(\phi(\omega+\Omega+\omega_0) - \phi(\omega+\omega_0))$.

The most straightforward procedure to reconstruct $\phi(\omega)$ from $\delta\phi$ is phase concatenation. Assuming that the temporal field is nonzero only for a duration $T = 2\pi/\Omega$, the spectral field is uniquely defined by its values at regularly

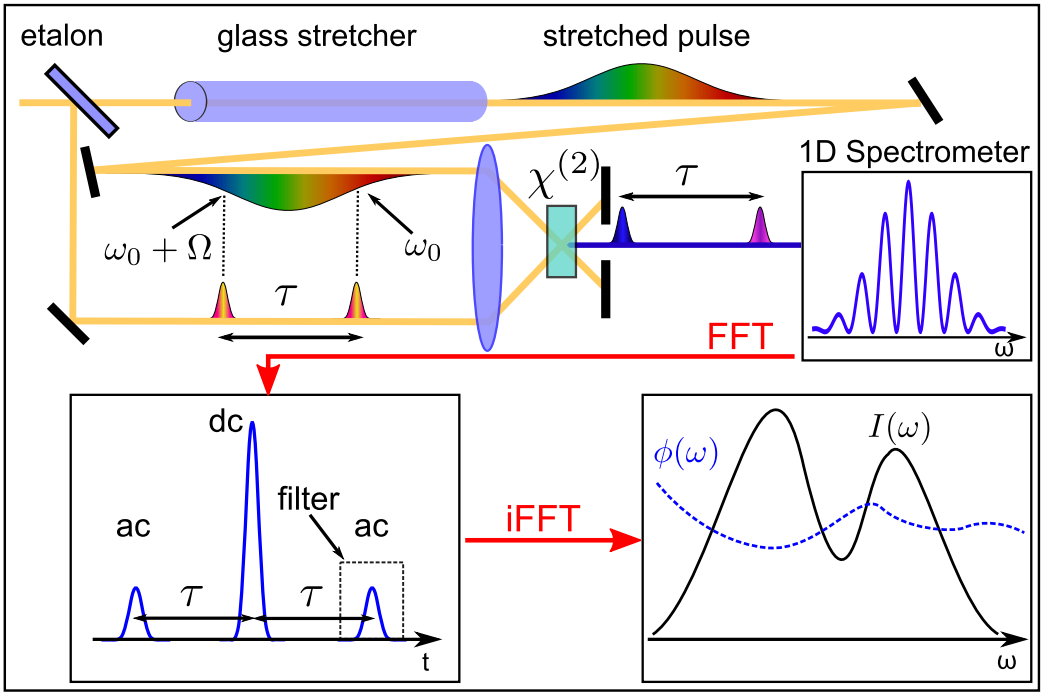


Figure 2.22: A schematic of a standard SPIDER setup. The input pulse is reflected by the front and back surface of an etalon, creating two pulses that are delayed. The transmitted pulse is stretched by a glass block and all three pulses are than overlapped in a nonlinear crystal. Due to the time delay, the short pulses overlap with different spectral parts of the stretched pulse leading to two time delayed pulses that are spectrally sheared. The measured spectrum is then Fourier transformed and filtered such that only one ac-peak remains. The inverse Fourier transform of this peak then yields the phase difference from which the phase can be reconstructed. See text for more detail.

spaced frequencies, $\omega_n = \omega_0 + n\Omega$. Setting $\phi(\omega_0) = 0$, the phase at each frequency ω_n can then be reconstructed:

$$\phi(\omega_n) = \sum_{j=0}^{n-1} \frac{1}{\Omega} \, \delta\phi(w_n) \tag{2.51}$$

and in connection with the spectral amplitude this determines the pulse in

the spectral and temporal domain.

There are some advantages in using a SPIDER compared to autocorrelation or FROG to measure an ultrashort pulse. The one-dimensional encoding of the phase in combination with the direct and rapid reconstruction algorithm makes it well-suited for online-monitoring and optimisation of the pulse [82]. In addition, the phase-matching conditions are less stringent than in SHG-FROG or auto-correlation because of the monochromatic ancilla beam and the use of type-II phasematching. Furthermore, since the phase is encoded in the modulation of the spectral fringes, the spectral response of the instrument is not an issue. Of course this all comes at the price of a more complex calibration for τ, ω_0 and Ω, and the need for very high spectral resolution. An appropriate stretcher for the chirped ancilla has to be built and due to the lower intensity of the stretched pulse the signal intensity is usually lower than in FROG or auto-correlation.

The phase-matching and spectral response advantages of SPIDER make it a perfect tool for ultrabroad and therefore ultrashort optical pulses. A slightly different setup than the one shown in Figure 2.22 is used for few-cycle pulses, called zero-additional phase SPIDER (ZAP-SPIDER). The etalon is the main problem for short pulses because of the constant time delay, τ, and the dispersion it introduces. In a ZAP-SPIDER two ancilla beams produced by a beam-splitter are used and overlapped at the nonlinear crystal with the test pulse with a controllable time delay. The test pulse is reflected from a beamsplitter at the SPIDER entrance with zero additional phase. At the nonlinear crystal, two signal beams are created with different directions and overlapped in a spectrometer. In our lab, we use a spatially-encoded SPIDER (SEA-SPIDER), that has a similar setup as a ZAP-SPIDER but uses a 2-dimensional spatially-resolving spectrometer (see section 4.2). It can map

the pulse shape spatially by re-imaging the crystal onto the spectrometer. In addition, we are using narrow tunable filters to prepare the ancillae for better calibration and control over the shear [83]. This arrangement can also be used for multiple-shearing spectral interferometry, which is especially suited to retrieve complex pulses with deep spectral holes [84].

2.2 Strong Field Physics

2.2.1 Ionisation in a Strong Field

Even with the single photon energy of a NIR laser being less than the ionisation potential of an atom, ionisation can still occur. At intensities above $\sim 10^{13}$ W/cm^2 different mechanisms occur that can release electrons. Here, the field strength present at the atom is strong enough to influence the atomic potential. This regime is called strong field physics and can be described by comparing the laser field with the electric field at the first Bohr orbit in hydrogen, given by the following relation:

$$E_{\text{Bohr}} = \frac{e}{4\pi\epsilon_0 a_0^2}, \tag{2.52}$$

where ϵ_0 is the free space permittivity, $a_0 = 5.3\times10^{-11}$ m the Bohr radius and e the electron charge. This leads to an electric field of $E_{\text{Bohr}} \approx 5\times10^{11}$ V/m. Using $I_{\text{peak}} = 1/2\, c\, \epsilon_0\, E_0^2$, the equivalent peak intensity to match E_{Bohr} is $I = 3.5\times10^{16}$ W/cm^2. Multi-photon processes in addition to distortion of the binding potential start at intensities roughly 100 times less than this.

In the following, I will shortly talk about two important quantities of strong field physics, the ponderomotive energy and the Keldysh parameter. I will then introduce three mechanisms of ionisation of atoms in strong fields. Depending on the intensity of the laser and the binding strength of the atomic

potential, there are different processes involved:

- Multi-photon ionisation (10^{12} – 10^{13} W/cm^2)
- Tunnel ionisation (10^{14} – 10^{15} W/cm^2)
- Over the barrier ionisation ($> 10^{15}$ W/cm^2)

2.2.1.1 Ponderomotive Energy

The ponderomotive energy is the cycle averaged kinetic energy a free charged particle gains in an oscillating electric field (like that of an electromagnetic wave). It is regularly used in strong field physics and will play a major part in the coming sections. The cycle averaged energy can be determined from the force F a charged particle experiences in an oscillating field $E_0 \cos(\omega t)$. This is given by:

$$F = \left|\vec{F}\right| = qE_0 \cos(\omega t) \Rightarrow \frac{1}{2}mv^2 = \frac{q^2 E_0^2}{2m\omega^2} \sin^2(\omega t),$$

where q is the charge and m the mass of the particle. The ponderomotive energy for an electron is the average over one cycle:

$$U_{\mathrm{P}}[\mathrm{eV}] = \left\langle \frac{1}{2} m_e v^2 \right\rangle = \frac{e\left|E_0\right|^2}{4m_e\omega^2} \approx 9 \times 10^{-14} I\lambda^2, \tag{2.53}$$

where m_e is the electron mass, I the intensity in W/cm^2 and λ the laser wavelength in µm.

2.2.1.2 The Keldysh Parameter

the Keldysh parameter can be used to distinguish the different ionisation regimes (Multi Photon Ionisation (MPI), Tunnel ionisation, Over the Barrier Ionisation (OTBI)) as a function of atomic species, laser wavelength and intensity. It is the ratio of the time it takes to tunnel through the barrier

T_{tunnel} and the oscillation period of the laser field T_{laser}, and is given by [85]:

$$\gamma = \frac{T_{\text{tunnel}}}{T_{\text{laser}}} = \sqrt{\frac{I_{\text{p}}}{2U_{\text{p}}}}. \tag{2.54}$$

By calculating γ one can find out the dominant process for the given intensity at a specific ionisation potential I_{p} and wavelength λ. For $\gamma \gg 1$, the tunnelling time is much larger than the oscillation period. Therefore it is much more likely to absorb multiple photons than tunnel. For $\gamma \ll 1$ the time needed to tunnel is much smaller than T_{laser} resulting in much higher probability of tunnelling than multi photon absorption. For $\gamma \approx 1$ there is a mixture of Above Threshold Ionisation (ATI) and tunnelling.

2.2.1.3 Multi Photon and Above Threshold ionisation

Multi photon ionisation and above threshold ionisation happen when the laser intensity is in a regime where it can still be treated as a perturbation to the binding potential. This is valid for intensities from $\sim 10^{13} - 10^{14}$ W/cm^2. Here, the electron gains enough energy to be ionised by successive absorption of single photons, through transitions via virtual states. Therefore the photon flux has to be sufficient such that every photon can be absorbed in less time then the virtual state lifetime. The ionisation rate from MPI is given by [86]:

$$R_N = \sigma_N I^N, \tag{2.55}$$

where σ_N is the generalised cross-section for the N^{th} order process and I the laser intensity. By increasing the intensity the non-perturbative side of this manifests in above-threshold ionisation. Here, the ionised electron continues to absorb more photons than the minimum number required for ionisation. The ATI electron spectra (Figure 2.23) show distinctive peaks separated by

the photon energy of the fundamental laser field. Its rate can be described similar to MPI as:

$$R_N = \sigma_{N+S} I^{N+S}, \tag{2.56}$$

where S is the number of additional photons absorbed. For higher energy electrons ($> 2\,U_p$) this description is incomplete. After an exponential decay the ATI spectrum shows a plateau region followed by a cutoff at $\sim\ 10\,U_\mathrm{p}$, reminiscent of the High-Harmonic Generation (HHG) structure (see subsection 2.2.2). And indeed, the physical link between HHG and ATI is described by the rescattering model [10, 11, 87, 88], where the electron can evolve and gain energy in the laser field. This leads to a maximum energy, depending on the phase at the time of ionisation, of $2\,U_\mathrm{p}$ and $\sim 10\,U_\mathrm{p}$ for direct and rescattered electrons respectively. This is different to MPI, where the phase does not play a role.

ATI spectra in the few-cycle regime are different again. The distinctive peak character 'washes out' due to the spatio-temporal intensity distribution. For ultrashort pulses there is a red-shift of the peaks attributed to the ponderomotive energy increasing the ionisation potential during the presence of the laser pulse [89]. Since U_p is intensity dependent the inner part of the beam will have a larger red-shift, than the outer part. The higher yield in the centre is compensated for by the larger volume of the lower intensity part. If the U_p is larger than the single photon energy, no ATI-peak structure will be present. Figure 2.23 shows ATI spectra for different intensities and different pulse lengths.

2.2.1.4 Tunnelling Regime

For even higher intensities, the electric field is disturbing the binding potential and, depending on the phase of the laser field, can significantly lower

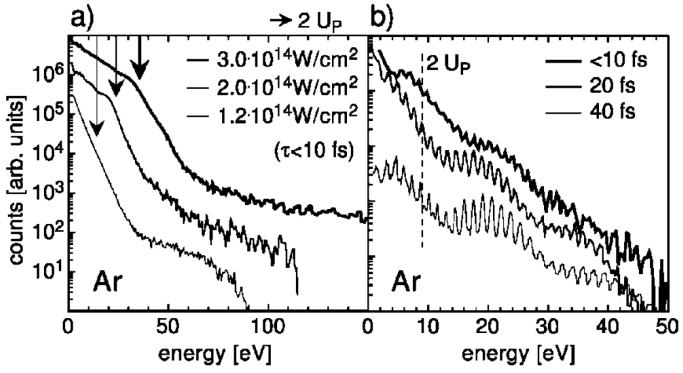


Figure 2.23: (a) ATI spectra of argon at three different intensities. (b) ATI spectra of Argon for different pulse durations at the same intensity ($0.8 \times 10^{14}\,\mathrm{Wcm}^{-2}$. The clear ATI-peak structure reduces as the pulse duration is decreased. Taken from [90]

the height of the barrier the electron sees. With a lower barrier, the electron has a higher probability of tunnel ionising. The ionisation rates for atomic tunnelling can be calculated using ADK theory (Ammosov, Delone and Krainov [2]) and more recent modifications [91]. Since the barrier is suppressed by the electric field of the laser, the tunnelling time of the electron has to be less than half of the optical cycle, because the field reverses its direction and will therefore raise the barrier again. This is the case for $\gamma \ll 1$, and here the barrier can be treated as a static field.

Recent discussions suggest that tunnelling is also present for $\gamma \gtrsim 1$. The physical mechanism behind this lies in a combination of "vertical heating" (MPI) while the electrons are moving under the barrier. For higher energies, the barrier will be narrower and, thus, the electron can escape easier [92].

2.2.1.5 Over the Barrier Ionisation

For even higher intensities ($\gtrsim 10^{15}$ W/cm^2), the binding potential gets more and more distorted until eventually the barrier is completely removed and the electron is unbound. This is known as over the barrier ionisation (OTBI). The critical intensity can be calculated as [86]:

$$I_{\mathrm{OTBI}}\,[\mathrm{W/cm^2}] = \frac{\pi^2 c\varepsilon^3 I_{\mathrm{p}}^4}{2Z^2 e^6} = 4\times 10^9\,(I_{\mathrm{p}}[\mathrm{eV}])^4\,Z^2 \tag{2.57}$$

where Z is the final charge state of the ion and I_{p} the ionisation potential. So for Ne $\rightarrow$ Ne$^+$ by OTBI, $I_{\mathrm{p}} = 21.56$ eV and $Z = 1$, the critical intensity is $I_{\mathrm{OTBI}} = 8.7\times 10^{14}$ W/cm^2.

2.2.2 High Harmonic Generation

The generation of very high odd multiples of the frequency of an intense laser pulse is referred to as high harmonic generation (HHG). It is a highly nonlinear process and is usually produced by focusing an intense laser pulse onto an atomic gas target [7], but HHG can also occur in molecules [93–96] or atomic clusters [97, 98] and much research has been done since the first demonstration [7, 99–101].

The interaction of the laser with the medium leads to the creation of new frequencies with a very distinct spectrum. It consists of lines that are separated by twice the frequency of the fundamental beam where only odd numbers are present:

$$\omega_q = q\omega_0 = (2n+1)\omega_0 \quad n = 1, 2, 3, ... \tag{2.58}$$

where q is the harmonic order and ω_0 the laser frequency. The conversion efficiency decreases rapidly in the first few orders, followed by a plateau, where all the harmonics have about the same intensity before a cut-off region,

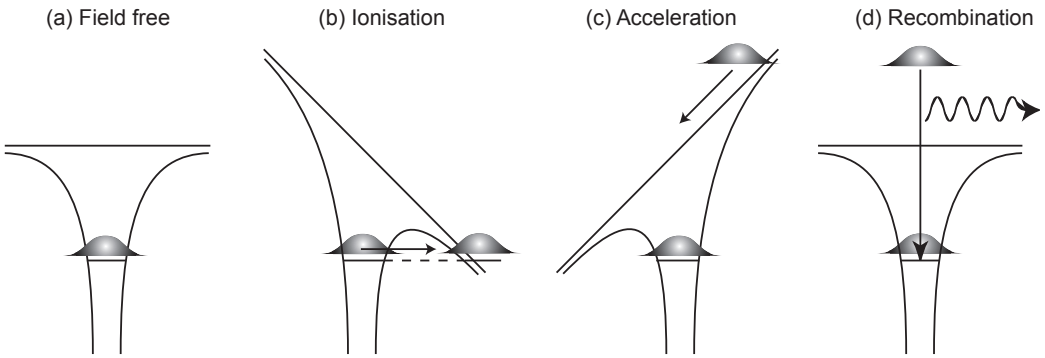


Figure 2.24: The three-step model for high harmonic generation. **(a)** The field free state, i.e. an electron in an atomic potential. **(b)** The atomic potential gets distorted and the electron can tunnel ionise. **(c)** The electron is accelerated in the laser field and gains energy. **(d)** When the oscillating laser field changes sign, the electron can return to the core and recombine with the parent ion. During this process, a photon is released with an energy corresponding to the kinetic energy of the electron. Figure adapted from [103]

where it decreases again. Instead of using a perturbative approach as is used e.g. for second harmonic generation, the presence of the plateau highlights that the HHG process is non-perturbative.

The spectrum can be described by a semi-classical approach using the three step model first described by Kulander [10] and Corkum [11]. A fully quantum mechanical model in Strong-Field Approximation (SFA) was introduced by Lewenstein *et al.* shortly afterwards [102].

The full HHG spectrum can be described by considering both the single atom response and the macroscopic response (the coherent superposition of individual fields).

2.2.2.1 Single Atom Response - The Three-Step Model

The three step model describes HHG in a semi-classical approach and was first described by Kulander [10] and Corkum [11] in 1993. This relatively simple model describes many of the spectral features discussed before. The three steps are as follows:

1. The potential of the atom or molecule is distorted by the laser field. This allows the electron to tunnel ionise at a time t_0. It is assumed that the electron has no initial kinetic energy.

2. The free electron gets accelerated by the laser field. When the field changes sign the electron gets driven back to the vicinity of the parent ion.

3. If the electron gets close to the parent ion, there is a probability of recollision. If the electron recollides it can radiatively recombine to emit a photon with the energy $\hbar\omega = E_{\mathrm{kin}} + I_{\mathrm{p}}$, where E_{kin} is the kinetic energy gained in the laser field and I_{p} is the ionisation potential.

Considering that the maximum energy an electron can gain at the first return in an oscillating field is 3.17 U_{p} (see Figure 2.26), the cut-off energy can be calculated to be:

$$\hbar\omega_{\mathrm{c}} = I_{\mathrm{p}} + 3.17\, U_{\mathrm{p}}, \tag{2.59}$$

where ω_{c} is the cut-off frequency and I_{p} the ionisation potential of the target medium. The maximum kinetic energy is gained if the electron ionises at $\omega t_{\mathrm{i}} = 17°$, assuming a cosine-waveform. Within a proper quantum description, it must be understood that this process is probabilistic. The first step (tunneling) is most likely when the intensity is the highest, so when the fundamental field has a maximum. This leads to a periodicity of half the period

of the fundamental field. Also, the electron should be treated as a quantum wave packet and not like a classical particle. The initial wave function, i.e. the ground state, is set into the continuum where it evolves and finally there is a transition back to the ground state associated with the emission of a photon.

The three-step model in the form of the SFA treats the atomic potential as a perturbation and uses the exact field. In the SFA it is assumed that the bound electron is not influenced by the external field and the electron in the continuum is not influenced by the ionic potential and can therefore be treated as a plane wave. The SFA approach is justified by considering that the ionisation process is dominant around the peak of the laser field and the electrons motion at time of birth is dominated by the laser field. When the oscillating laser field goes through a zero, the electron is already far away from the influence of the core and at time of recollision the electron has gained so much kinetic energy that the time it spends under the influence of the ionic potential is so short that the approximation is still reasonable.

I outline the SFA model starting from the time dependent Schrödinger equation:

$$i|\dot{\Psi}\rangle = \left[\hat{H}_0 + \hat{V}(t)\right]|\Psi\rangle \tag{2.60}$$

where $\hat{H}_0$ is the field-free Hamiltonian and $\hat{V}(t)$ is the interaction with the laser field. This equation is separated into a field free (homogeneous) part and inhomogeneous part including the laser field interaction $\hat{V}(t)$. Solving the homogeneous part is trivial:

$$|\Psi^0\rangle = e^{-i\hat{H}_0 t}|\Psi(t=0)\rangle \tag{2.61}$$

where Ψ^0 is the solution for the field free case. The transition amplitude for the inhomogeneous part can be solved with the S-matrix formalism by

projecting the solution onto a final state $|\Psi_f\rangle$[iii]. This leads to an exact solution for the transition amplitude [92, 102]:

$$a_{fi}(t,t_i) = -1 \int_{t_i}^{t} \mathrm{d}t' \langle \Psi_f | e^{-i\int^{t'} \hat{H}(t'')\mathrm{d}t''} \hat{V}(t') e^{i\hat{H}_0 t'} | \Psi(t=0) \rangle. \tag{2.62}$$

The equation above is called the direct S-matrix amplitude and describes the probability from going from an initial state $|\Psi(t=0)\rangle$ to the final state $|\Psi_f\rangle$. The SFA simplifies this propagator to the well known Volkov propagator [85]:

$$e^{-i\int_t^{t'} \hat{H}(t'')\mathrm{d}t''} |\mathbf{p}(t')\rangle = e^{-1\int_t^{t'} E(t'')\mathrm{d}t''} |\mathbf{p}(t)\rangle \tag{2.63}$$

where the kinetic momentum $\mathbf{p}(t)$ is given by the following equation:

$$\mathbf{p}(t) = \mathbf{p}(t') - \mathbf{A}(t') + \mathbf{A}(t) \tag{2.64}$$

and where $\mathbf{A}(t)$ is the vector potential of the electric field. Using the assumptions from above the amplitude of finding an electron in state $|\mathbf{p}\rangle$ after propagation time t can be written as:

$$a_{\mathbf{p}}(t) = -i \int_{t_i}^{t} \mathrm{d}t' e^{-i\int_{t'}^{t} E(t'')\mathrm{d}t'' + iI_p(t-t_0)} \langle \mathbf{p} + \mathbf{A}(t') - \mathbf{A}(t) | \hat{V}(t') | g \rangle \tag{2.65}$$

To apply this to high harmonic generation we are interested in the Fourier components of the dipole moment. By using the wave function obtained from above:

$$\Psi(t) = \int \mathrm{d}\mathbf{p} |\mathbf{p}\rangle a_{\mathbf{p}} \tag{2.66}$$

and the dipole moment can be calculated as:

$$\mathbf{d}(t) = -i \int_{t_i}^{t} \mathrm{d}t' \int \mathrm{d}\mathbf{p} e^{-i\int_{t'}^{t} E(t'')\mathrm{d}t'' + iI_p(t-t_0)} \langle \mathbf{p} + \mathbf{A}(t') - \mathbf{A}(t) | \hat{V}(t') | g \rangle \langle g | \mathbf{d} | \mathbf{p} \rangle. \tag{2.67}$$

From the Fourier transform of this dipole moment the high harmonic spectrum can be calculated. The complete derivation is beyond the scope of this thesis, the interested reader should refer to [102, 104].

[iii] By assuming that $|\Psi_f\rangle$ was not initially populated the field-free part yields zero.

2.2.2.2 Classical Electron Trajectories

The classical trajectories give some insight into the dynamics of HHG and yield some meaningful results. Consider an electron that is liberated from the atom at a time t_0 and has zero initial kinetic energy, $v(t_0) = 0$. The equation of motion can easily be solved and is given by the ordinary differential equation:

$$\frac{\mathrm{d}^2x}{\mathrm{d}t^2} = \frac{e}{m_e} E_0 \cos(\omega t + \phi), \tag{2.68}$$

where e and m_e are the electron charge and mass respectively. With the initial conditions:

$$\text{(i)}: x(t_0) = 0,$$
$$\text{(ii)}: \ \mathrm{d}x/\mathrm{d}t|_{t=t_0} = 0.$$

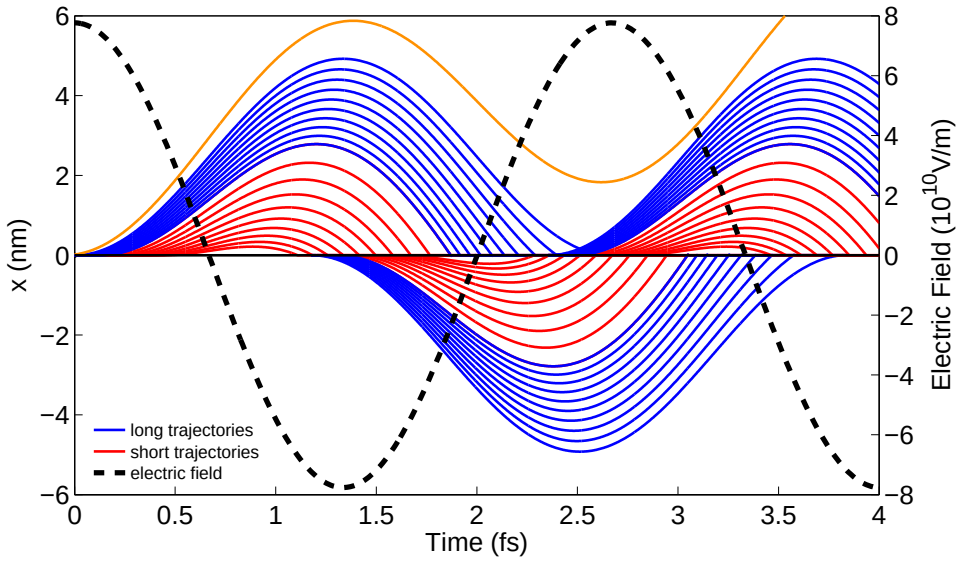


Figure 2.25: Calculated electron trajectories for an 800 nm field with an intensity of $8 \times 10^{14}\,\mathrm{W/cm^2}$. Short and long trajectories are coloured red and blue respectively. The dashed line shows the electric field. Orange trajectory: one non-recolliding electron ionised at $t = -0.05$ fs

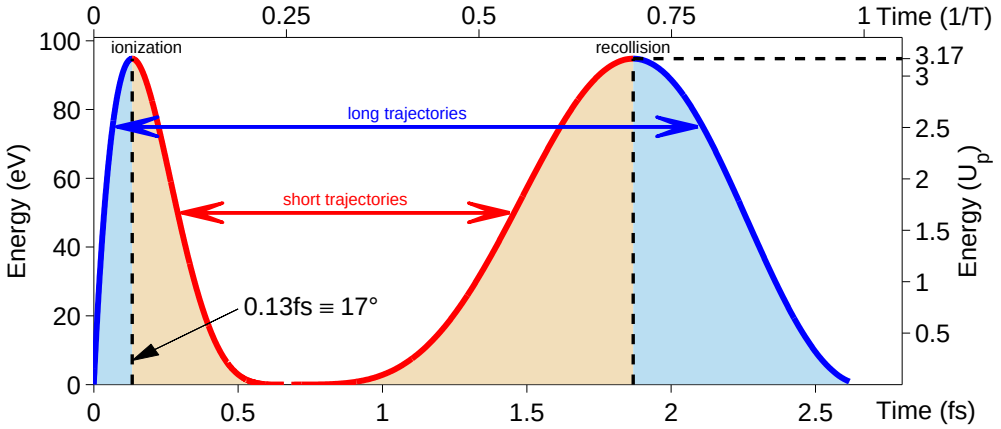


Figure 2.26: Electron kinetic energy against both ionisation and recollision time for electrons in a laser field with wavelength 800 nm and intensity of $8 \times 10^{14}\,\mathrm{W/cm^2}$. The red lines correspond to the short trajectories, whilst the blue lines correspond to the long trajectories. The division is made about the time with highest electron energy.

The solutions to $x(t)$ and $v(t)$ are given by:

$$\frac{\mathrm{d}x}{\mathrm{d}t} = \frac{eE_0}{m_e\omega}\big[\sin(\omega t) - \sin(\omega t_0)\big], \tag{2.69}$$

$$x(t) = -\frac{eE_0}{m_e\omega^2}\big[\cos(\omega t) - \cos(\omega t_0) - \omega(t - t_0)\sin(\omega t)\big] \tag{2.70}$$

and the kinetic energy E_{kin} can then be calculated to be:

$$E_{\mathrm{kin}}(t) = \frac{1}{2}m_e v^2(t) = 2\,U_{\mathrm{p}}\big[\sin(\omega t) - \sin(\omega t_0)\big]^2, \tag{2.71}$$

where $U_{\mathrm{p}} = e\,|E_0|^2\,/4m_e\omega^2$ is the ponderomotive energy. The harmonic energy is then given as $E_{\mathrm{XUV}} = I_{\mathrm{p}} + E_{\mathrm{kin}}(t_{\mathrm{f}})$, where t_{f} is the recollision time..

Not every electron released recollides with the parent ion (see orange trajectory in Figure 2.25). Only for some ionisation times the electron will recollide at a later time and recollision time and therefore recollision energy has to be solved numerically. Figure 2.26 shows the energies corresponding to the ionisation and recollision times.

The electron accumulating the maximum energy $E_{\max} = 3.17\ U_{\mathrm{p}}$ in the accelerating laser field is released at:

$$(\omega\ t_{\mathrm{i}})_{E_{\max}} = 17^{\circ}.$$

This point is also a division between two different types of trajectories, the long and the short trajectories. There is a clear distinction between trajectories before and after this time. Short trajectories are ionised after the long trajectories but recollide before them. Another observation is the difference in the relation between recollision time and harmonic energy. Short trajectories gain more energy the later they recollide (= negative chirp) whereas it is the opposite for long trajectories (= positive chirp). This chirp is often referred to as the 'atto-chirp'.

2.2.2.3 The Role of Phasematching in HHG

So far I have only considered the single atom response and the emission from a single atom. The overall XUV field generated is the coherent sum of many atoms involved in the process. In order to constructively interfere the HHG field must be in phase over the interaction length. So just like in second harmonic generation (Equation 2.23) we write the phase-mismatch as:

$$\Delta\vec{k} = \vec{k_q}(r,z) - q\vec{k_1}(r,z) \tag{2.72}$$

where q is the harmonic order and $\vec{k_1}$ is the wave vector of the fundamental field. For $\Delta k \neq 0$ one can define a coherence length over which the harmonic field can grow. The smaller the mismatch, the longer the coherence length and therefore the more efficient the harmonic generation:

$$L_{\mathrm{coh}} = \pi/|\Delta\vec{k}|. \tag{2.73}$$

Δk has contributions from a number of sources. The major contributions to $\Delta\vec{k}$ are the geometrical phase from the focusing of the laser beam, $\vec{k}_{\mathrm{geo}}(r,z)$, and the atomic phase resulting from the phase of the dipole radiation, $\vec{k}_{\mathrm{dip}}(r,z)$. The overall phase mismatch is given by [105]:

$$k_{\mathrm{q}}(r,z) = k_{\mathrm{q}} - \left|\vec{k}_{\mathrm{dip}}(r,z) + q\left(\vec{k}_{\mathrm{geo}}(r,z) + \vec{k_1}\right)\right|, \tag{2.74}$$

where $k_{\mathrm{q}} = \omega_{\mathrm{q}}/c$ is the wave vector of the high harmonic field.

The geometrical phase picked up by going through the focus is called the Gouy phase and for a Gaussian pulse is given as [106]:

$$\phi_{\mathrm{geo}}(r,z) = -\tan^{-1}\left(\frac{2z}{b}\right) + \frac{2k_1 r^2 z}{b^2 + 4z^2}, \tag{2.75}$$

where b is the confocal parameter. For $r = 0$ the Gouy phase flips from $\pi/2$ to $-\pi/2$, therefore the beam acquires a total phase of π when going through the focus. Hence, the wave fronts of the beam will advance faster when being focused then without going through a focus.

The atomic phase has its origin in the phase of the dipole moment acquired by the electron when going through the continuum. From Equation 2.67 the atomic phase is given as:

$$\phi_{\mathrm{dip}}(t',t) = -\int_{t'}^{t} S(t'')\mathrm{d}t'', \tag{2.76}$$

where $S(t)$ is the classical action defined as the difference of the kinetic and potential energy. It is therefore dependent on the intensity and the time spent by the electron in the continuum. In the long-pulse limit it can be approximated by [107]:

$$\phi_{\mathrm{dip}}(t',t) = \alpha_j U_{\mathrm{p}}/\omega_1, \tag{2.77}$$

where j stands for a specific trajectory, defined by time of release and recollision, α_j is a proportionality constant that is proportional to the time

spent in the continuum and U_p is the ponderomotive energy. This is a good approximation even down to three cycle laser pulses [108].

Putting Equation 2.75 and 2.77 into Equation 2.74 using $k = \nabla\phi$, leads to an overall wave vector mis-match along the propagation axis of:

$$\Delta k_\mathrm{q}(r=0,z) = \alpha_j \frac{\mathrm{d}}{\mathrm{d}z}(U_\mathrm{p}/\omega_1) + q\,\frac{2}{b(1+(2z/b)^2)}. \tag{2.78}$$

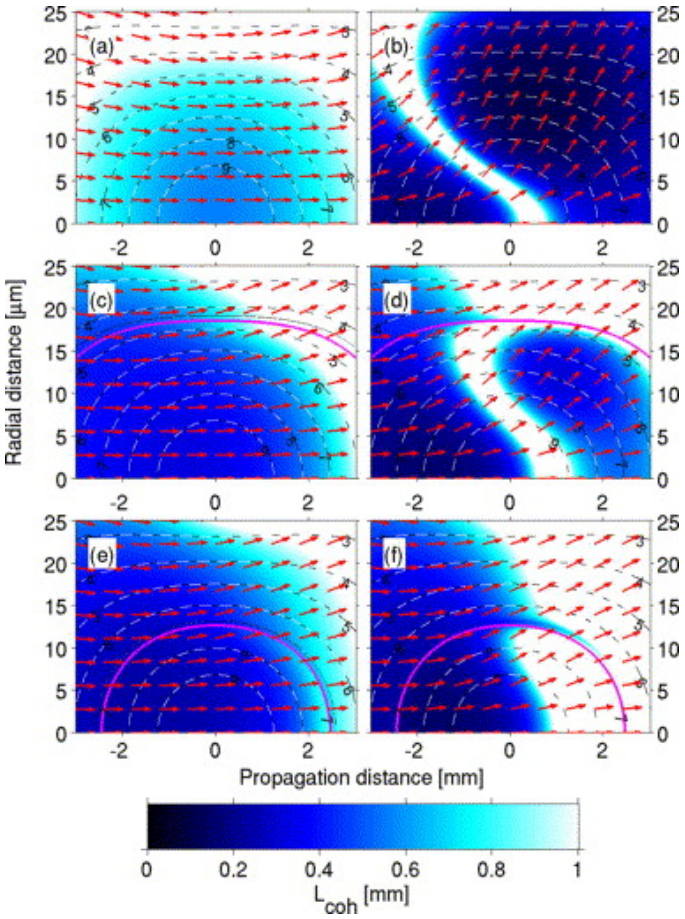


Figure 2.27: Phase matching maps for short (left) and long(right) trajectories for the 21st (a,b), 35th (c,d) and 45th (e,f) harmonic in neon, driven by a 750 nm, $4 \times 10^{14}\,\mathrm{W/cm^2}$ laser pulse with a confocal parameter of 7 mm. The (red) arrows indicate the direction of the best phase-matching. The solid (purple) lines mark the cutoff position. Taken from [106]

Since the second term in this equation is always positive, to get a Δk_{q} close to zero the phase contributed by the dipole has to be negative. Therefore, to phase-match efficiently the target has to be placed after the focus, where the intensity is decreasing with z.

A more complete treatment of phasematching for few-cycle pulses is shown in Figure 2.27 [106]. Here pulse broadening during propagation due to dispersion from the ionised medium, geometrical phase as well as the dipole phase are taken into account. It shows that the harmonic generation from short trajectories is mainly phase-matched downstream with a low divergence in contrast to the best phase-matching conditions for long trajectories shown in (b) and (d). Here the best phase-matching conditions are before the laser focus (at $z = 0$) and the divergence is larger, leading to more divergent harmonics.

2.2.3 Attosecond Pulses

The generation of attosecond (10^{-18} s) pulses requires a central frequency that is higher than any laser medium can support. From the time bandwidth equation (Equation 2.7) the central wavelength of a pulse with a duration of 100 as needs to be below 30 nm and have a bandwidth larger than 13 eV ($\equiv$ 10 nm). Therefore in order to utilise lasers for attosecond pulse generation, a method to convert the coherent laser beam to higher frequencies is needed. The most successful route for this has been the use of high harmonics (HHG) which has been discussed in the previous section. HHG for attosecond pulse generation was first proposed by Farkas and Tooth in 1992 [8]. In HHG the underlying process is already on a sub-femtosecond scale. Going back to the single atom response (subsection 2.2.2), the electrons are ionised every half cycle, where the release time has a corresponding time of return. The spread

of the return times above a certain energy can be less than one femtosecond (see Figure 2.26). Looking at the single atom response more closely, reveals some problems with this simple picture. The harmonics spectrum in the plateau region has two contributions, the short and the long trajectory, from every half-cycle of the laser. Only in the cut-off region, there is only one burst per half-cycle. An unfiltered harmonic burst from a linearly polarised laser beam will therefore not emit an attosecond pulse.

The dominant contributions from the short and long trajectories can be chosen by carefully choosing the right phase-matching geometry (see subsubsection 2.2.2.3). Using only short trajectories, there will only be a single contribution from every half-cycle leading to a train of attosecond pulses separated by a half-period of the laser. This can also be seen when taking the Fourier transform of an HHG spectrum. The separation of each harmonic by twice the frequency of the generating field in the spectral domain, will lead to a train of pulses separated by half the period with a temporal width corresponding to the spectral width of the envelope of all used harmonics [109].

To generate a single attosecond pulse a continuous harmonic spectrum generated by a single half-cycle is needed. So far, two different methods have been proven successful. One technique is referred to as optical-gating, where a time-dependent ellipticity in the driving pulse is used, thereby gating the harmonic emission [111]. This technique has recently measured a single attosecond pulse with a duration of 280 as and could reduce the pulse duration to 130 as by compensating the inherent atto-chirp with a thin aluminium foil [112]. A different variant of optical gating is so called Double-Optical Gating (DOG) proposed by the group of Chang [113], where a small portion of a second harmonic of the fundamental beam helps with issues arising from ionisation depletion in the rising part of the elliptical pulse. This method re-

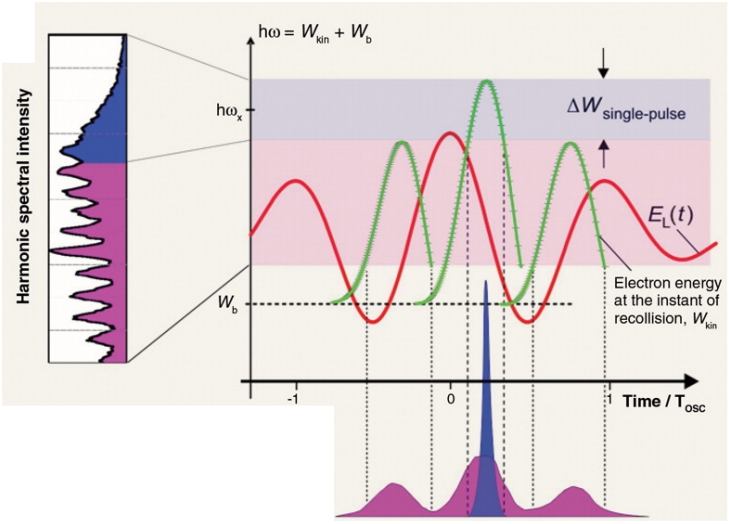


Figure 2.28: A schematic of amplitude gating. Temporal confinement to contributions of only one half-cycle can be achieved by spectral filtering. For a cosine-pulse, the photon energies from the central laser peak are higher than the photon energies from the other peaks. By filtering out only the higher energies the XUV burst is confined to a single attosecond pulse. Figure taken from [110]

cently measured single attosecond pulses with durations of 150 as generated by a 28 fs driving field [114].

A different route to single attosecond pulses is using CEP-stabilized few-cycle pulses in conjunction with spectral filtering. The underlying physics is shown in Figure 2.28. By using a cosine-pulse in the few-cycle limit, the instantaneous intensity from the maximum peak and the neighbouring peaks can differ by more than 70%, therefore the maximal photon energies from the dominant peak are higher, creating a continuum in the cut-off region. After filtering out only the cutoff region, usually done with a thin metal filter and a multilayer XUV mirror, only a single attosecond pulse is left. Therefore the effective gate that limits the XUV bursts to a single half-cycle

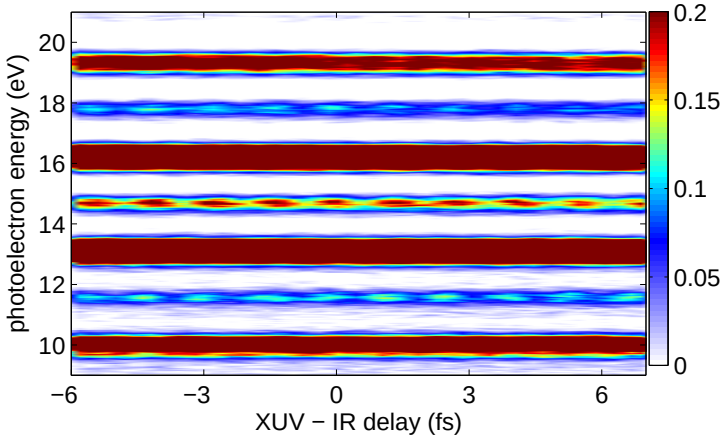


Figure 2.29: Experimental RABITT trace: A two-photon, two-colour photoelectron spectrogram from a Ne target as the delay between the XUV (from argon harmonics) and IR pulses (25 fs) is varied.

is the change in amplitude between successive maxima of the laser intensity. For that reason this technique is also referred to as amplitude-gating. It was first demonstrated by Hentschel et. al. in 2001 [115] and has since been improved [3, 5, 110] to generate the shortest optical pulses, down to 80 as [4].

The generation of these attosecond pulses is only one part of the problem. The characterization is an equally if not more difficult task. There are two key methods currently used for the characterization. The "Reconstruction of Attosecond Beating by Interference of Two-photon Transitions" (RABITT) [109, 116] is typically used for attosecond pulse trains. Isolated attosecond pulses on the other hand are usually measured with an atomic streak camera [5, 117, 118].

2.2.3.1 Reconstruction of Attosecond Beating by Interference of Two-photon Transitions

Reconstruction of Attosecond Beating by Interference of Two-photon Transitions (RABITT) measures the phase between adjacent harmonics by a two-photon two-colour ionisation. The harmonic field is focused onto a gas target with a weak Infra-Red (IR) field present. This generates photo-electrons from harmonics with energies higher than the ionisation potential, I_p, of the target gas. The kinetic energy of the electrons is given by: $E_{e^-} = E_\mathrm{XUV} - I_\mathrm{p}$ and the spectrum will therefore have distinct peaks corresponding to the harmonic spectrum. With a low-intensity IR field present, weak sidebands appear halfway between the odd harmonics. There are two quantum paths that can be the origin of the sidebands: (i) Either absorption of one XUV photon from the q^th harmonic H_q plus one IR photon or (ii) absorption of one XUV photon H_{q+2} with emission of one IR photon. These two contributions will interfere with each other leading to an oscillatory term in the amplitude of the sidebands [119]:

$$S_{q+1} = S_0 \cos\left(2\phi_\mathrm{IR} + \phi_q - \phi_{q+2} + \Delta\phi^\mathrm{at}_{q+1}\right), \tag{2.79}$$

where ϕ_IR and ϕ_q are the phases of the IR and XUV field respectively and ϕ^at_{q+1} is the atomic phase given by Equation 2.76. This phase has only a small effect on the pulse retrieval and can be neglected [120]. When delaying the IR field with respect to the high harmonics, the IR phase can be written as: $\phi_\mathrm{IR} = \omega_0\tau$. The sideband intensity therefore oscillates at twice the laser frequency.

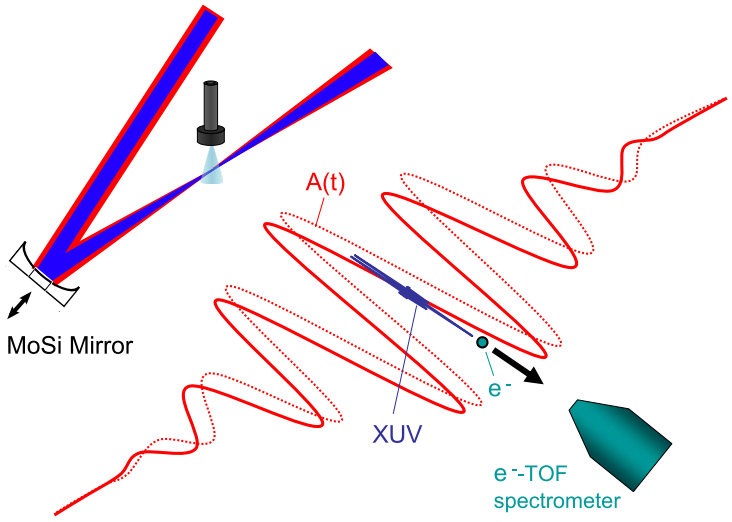


Figure 2.30: A schematic of the atomic streaking camera. Both the IR as well as the XUV-field are focused into an atomic gas target. The XUV ionises the gas and the XUV phase and amplitude get transferred to an electron wavepacket. Depending on the temporal delay between the IR and XUV, the photoelectrons will be streaked up or down in energy along the time-of flight direction.

2.2.3.2 Atomic Streak Camera

A streak camera is used to measure the duration of light pulses by mapping the temporal profile onto a spatial profile. It has been used to measure the duration of picosecond laser pulses [121]. The laser pulse impinges onto a photocathode releasing electrons with the same temporal profile as the laser pulse. These electrons are then deflected by a time-varying electric field and usually detected on a fluorescent screen, where they generate a "streak". The atomic streak camera works under the same principles. Here the photoelectrons are generated by photo-ionisation in a gas and then streaked by the electric field of the generating IR beam. The electron energy is then

measured with an electron time of flight spectrometer.

Closely following the derivation of Quéré [118], the above can be put in a more physical context. The ionisation of an atom by an XUV field alone can be described by the transition amplitude $a_{\mathbf{p}}$ from the ground state to the final state $|\mathbf{p}\rangle$ with momentum $\mathbf{p}$. Using atomic units and assuming that only the outermost electron contributes to the ionisation process, this is given by first order perturbation theory to be [118]:

$$a_{\mathbf{p}} = -i \int_{-\infty}^{\infty} \mathrm{d}t \; \mathbf{d}_{\mathbf{p}} \, \mathbf{E}_{\mathrm{XUV}}(t) \exp\left[i(W + I_{\mathrm{p}})t\right], \tag{2.80}$$

where $W = \mathbf{p}^2/2$ is the energy of the final state , $\mathbf{E}_{\mathrm{XUV}}(t)$ the XUV electric field and $\mathbf{d}_{\mathbf{p}}$ the dipole transition matrix element from the ground state to the final state. Assuming that $\mathbf{d}_{\mathbf{p}}$ is not dependent on the photon energy or phase, this equation shows that the photo-electron spectrum $a_{\mathbf{p}}$ is a replica of the XUV field in both amplitude and phase. So, by measuring the electrons one yields all the information about the XUV pulses too.

The atomic streaking recorder [5] can measure the phase of the XUV by recording a spectrogram with an additional IR streaking field and measuring the electron energy spectrum as a function of the delay, τ, between the two. The transition amplitude, $a_{\mathbf{p}}(\tau)$ in the presence of this dressing field can be written as:

$$a_{\mathbf{p}}(\tau) = -i \int_{-\infty}^{\infty} \mathrm{d}t \; \exp(i\phi(t)) \; \mathbf{d}_{\mathbf{p}} \, \mathbf{E}_{\mathrm{XUV}}(t - \tau) \exp\left[i(W + I_{\mathrm{p}})t\right], \tag{2.81}$$

$$\phi(t) = -\int_{t}^{\infty} \mathrm{d}t' \left(\mathbf{p} \cdot \mathbf{A}(t') + \mathbf{A}^2(t')/2\right), \tag{2.82}$$

where $\mathbf{p}^2(t)/2 = W = \mathbf{p} \cdot \mathbf{A}(t) + \mathbf{A}^2(t)/2$ is the instantaneous momentum and $\mathbf{A}(t)$ the vector potential, related to the electric field by $\mathbf{E}_{\mathrm{L}}(t) = -\partial\mathbf{A}/\partial t$. The spectrogram that is recorded by the atomic streaking recorder is given by the modulus squared of the transition amplitude.

So the main effect of the laser field is the temporal phase, $\phi(t)$, it induces onto the photo-electron wavepacket. The scalar product between the laser and the final momentum, $\mathbf{p} \cdot \mathbf{A}$, shows that transition depends on the detection direction with respect to the polarisation.

This is shown more clearly when using a linearly polarised laser field, $\mathbf{E}_\mathrm{L} = \mathbf{E}_0(t)\ \sin(\omega_\mathrm{L} t)$. Using the slowly-varying envelope approximation, Equation 2.82 can be simplified to be [118]:

$$\begin{aligned} \phi(t) &= \phi_1(t) + \phi_2(t) + \phi_3(t), \\ \phi_1(t) &= -\int_t^\infty \mathrm{d}t\ U_\mathrm{p}(t), \\ \phi_2(t) &= \frac{\sqrt{8WU_\mathrm{p}(t)}}{\omega_\mathrm{L}}\ \cos\theta\ \cos\omega_\mathrm{L} t, \\ \phi_3(t) &= -\frac{U_\mathrm{p}(t)}{2\omega_\mathrm{L}}\ \sin(2\omega_\mathrm{L} t), \end{aligned} \tag{2.83}$$

where $U_\mathrm{p}(t)$ is the ponderomotive energy and θ the angle between the final momentum $\mathbf{p}$ and the laser polarisation direction. The first phase term $\phi_1(t)$ is varying on the timescale of the laser envelope, whereas ϕ_2 and ϕ_3 are oscillating at the laser frequency and its second harmonic. As mentioned above, there is a substantial difference in the detection direction though. Since the final energy, W, is large compared to the ponderomotive energy of the weak IR field, the second phase ϕ_2 is larger than ϕ_3 unless the detection angle is close to $\theta = 90°$, where the cosine term goes to zero. Figure 2.31 shows simulations I have done to show the difference between a detection angle of $\theta = 0°$ and $\theta = 90°$, keeping all the other parameters the same.

Another interesting point is the similarity of the spectrogram with the FROG equation. Comparing Equation 2.81 with Equation 2.43 shows that by scanning the delay, the dressing field can be used as a temporal phase gate $g(t) = e^{i\phi(t)}$. This means a FROG measurement can be done with XUV

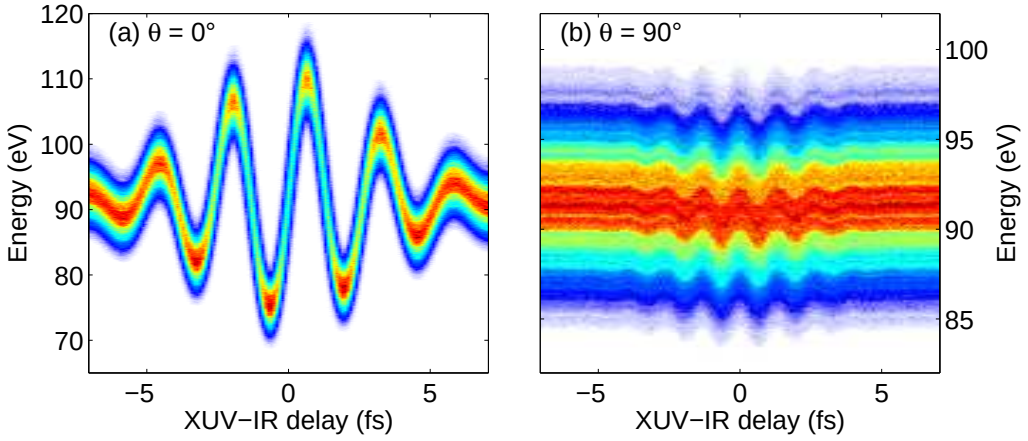


Figure 2.31: Streaking simulations of an 250 as XUV beam centred around 92 eV streaked by an IR field with a duration of 5 fs, an intensity of 10 TW/cm^2 and CEP = 0 for (a) $\theta = 0°$ and (b) $\theta = 90°$.

photo-electron spectroscopy. Frequency-resolved optical gating for complete reconstruction of attosecond bursts (FROG-CRAB) [73] is now the most common technique for the full characterisation of attosecond XUV pules [4, 122].

The atomic streak camera can also be described in a more intuitive semi-classical picture. The trajectory in the continuum is described with classical mechanics and the momentum is then given by:

$$\mathbf{p}(t) = \mathbf{A}(t) + [\mathbf{p}_0 - \mathbf{A}(t_\mathrm{i})]\,, \tag{2.84}$$

where $\mathbf{p}_0$ is the initial momentum with $W_0 = \mathbf{p}_0^2/2m = E_\mathrm{XUV} - I_\mathrm{p}$ and $\mathbf{A}(t)$ the vector potential of the dressing field. The first term on the right oscillates with the laser field, or rather the time derivative of the electric field and eventually goes to zero. The right term is defined by the conditions at the ionisation time. The experimental measure, i.e. the final electron energy, is therefore defined by the vector potential at the time of ionisation and the

initial energy given by the XUV photon minus the ionisation potential. The final kinetic energy for a linearly polarised dressing field in the slowly-varying envelope approximation can then be written as:

$$\begin{aligned} W_{\mathrm{f}} = W_0 - U_{\mathrm{p}}(t_{\mathrm{i}}) + U_{\mathrm{p}}(t_{\mathrm{i}}) \cos 2\omega_{\mathrm{L}} t_{\mathrm{i}} \\ + 4U_{\mathrm{p}}(t_{\mathrm{i}}) \cos^2\theta \ \sin^2 \omega_{\mathrm{L}} t_{\mathrm{i}} \\ + \sqrt{8W_0 U_{\mathrm{p}}(t_{\mathrm{i}})} \cos\theta \ \sin \omega_{\mathrm{L}} t_{\mathrm{i}}, \end{aligned} \tag{2.85}$$

where, as before, θ is the angle between the laser polarisation and the final momentum. This picture, although very intuitive, cannot quantitatively describe the spectral interferences between electrons that were ionised at different times but end up with the same final energy [118]. Nevertheless it is an equivalent description for attosecond pulses that are much shorter than the laser period and provides us with some insight of the physics beneath it. The connection between the two models can be seen when using a linear expansion of phase $\phi(t)$ from equations 2.82 and 2.83. A linear phase modulation will induce a shift in energy, $\delta W = W - W_0 = -\partial\phi/\partial t$, and solving this will lead to the same expression as for the semi-classical description in Equation 2.85.

Chapter 3

Waveform Stabilised Few-Cycle Drive Laser

3.1 Front-End

The laser system is based on a commercially available Titanium:Sapphire (Ti:Sa) single-stage CPA system (Femtopower, Femtolasers GmbH). This system generates pulses with an energy of about 1 mJ, a duration of 30 fs and a spectrum with a FWHM of $\sim$ 50 nm centred around 800 nm with a repetition rate of 1 kHz.

The output of the CPA system can be CEP stabilised. The CEP stabilisation is discussed in subsection 3.1.2 and a brief overview of the system is given in subsection 3.1.3.

3.1.1 CPA Laser

The main parts of the commercial CPA laser are presented here. It consists of four main parts, oscillator, stretcher, amplifier and compressor that are described in the following sections.

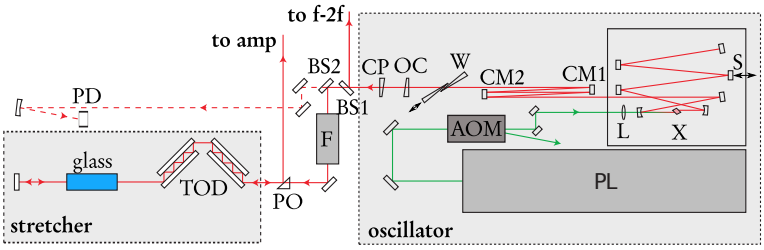


Figure 3.1: A schematic of the oscillator and stretcher. Pl: pump laser, AOM: acousto-optic modulator, L: lens, X: gain medium, S: adjustable focusing mirror, CM1,2: chirped mirror, W: wedges, OC: output coupler, CP: compensation plate, BS1,2: beam splitter, F: Faraday isolator, PO: pick-off prism, TOD: third order dispersion mirrors, PD: photo-diode. Refer to the text for more detail.

3.1.1.1 Oscillator and Stretcher

The Ti:Sa oscillator provides a train of 10 fs pulses at a repetition rate of 78 MHz through softly apertured Kerr-lens mode-locking and the use of intracavity chirped mirrors (CM). It is pumped by a 4 W frequency doubled (532 nm), diode-pumped Nd:YVO_4 laser (Verdi, Coherent). The pump laser (PL) beam passes an acousto-optic modulator (AOM) that is used to control the CEP slip (refer to subsection 2.1.7 and Figure 2.19). The is done by adjusting the intracavity peak power and therefore changing the nonlinear phase shift experienced in the oscillator [123]. In addition to the chirped mirrors, the intra-cavity dispersion is controlled with a pair of wedges (W). The oscillator delivers pulses with an energy of $E_{\mathrm{osc}} \sim 5\,\mathrm{nJ}$ equivalent to $P \sim 400\,\mathrm{mW}$ average power and a spectral bandwidth $\Delta\lambda_{\mathrm{osc}} \approx 100\,\mathrm{nm}$ FWHM. The output is split by a 50/50 beamsplitter (BS), where one half is delivered to the f-to-$2f$ interferometer for CEP detection and the other half is the seed for the amplifier.

The seed is passed through an optical Faraday isolator (FI) to prevent back-reflections from entering the oscillator, which can disrupt mode-locking.. It is then stretched to 10 ps by double-passing a 10 cm long SF57 glass block (GB). There are also multiple bounces (26) on two pairs of chirped mirrors (TOD) with 100 fs^3 per bounce, to pre-compensate the third-order dispersion imposed mainly by the prism-compressor. A schematic of the layout is shown in Figure 3.1.

3.1.1.2 Amplifier

A schematic of the amplification stage is shown in Figure 3.2. The stretched pulse is fed into the multi-pass Ti:Sa amplifier that is pumped by a 12 W frequency-doubled, diode-pumped Nd:YLF laser that is Q-switched at 1 kHz and externally triggered by the oscillator. The pump double passes the amplifier crystal to deposit $\sim 90\%$ of the energy. The crystal is set in a vacuum chamber (C) with Brewster entrance windows (BW) and cooled by a Peltier element to ~ 235 K to reduce thermal lensing.

The full pulse-train passes the amplifier four times before entering a pulse picker to limit amplified spontaneous emission (ASE). The pulse picker consists of a Pockel's cell (PC) a Berek polarisation compensator (BC) to clean up the polarisation and a polarising beam splitter (PBS2) that transmits only the pulse whose polarisation has been rotated by the Pockel's cell. This reduces the repetition rate from the oscillator's 78 MHz to 1 kHz. This pulse is then passed through the amplifier crystal five more times to reach a final energy before the compression stage of 1.2 mJ. The overall gain is therefore roughly 10^6 corresponding to an average gain of 4.5 per pass.

In the process of amplification the spectrum is narrowed due to gain narrowing resulting in a reduction of the spectral FWHM to $\Delta\lambda \approx 40 - 50$ nm.

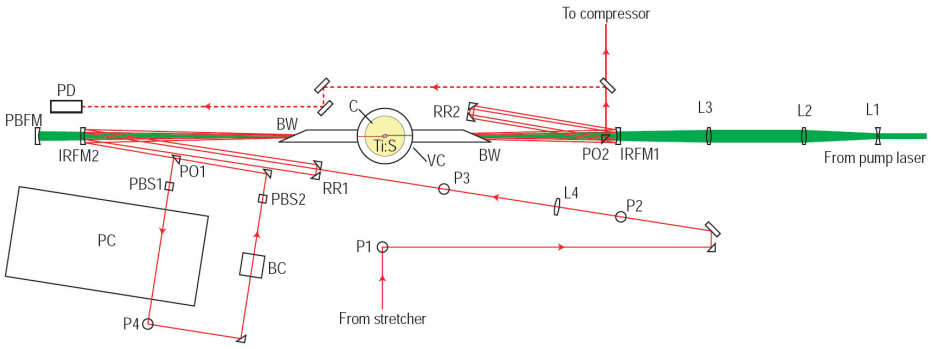


Figure 3.2: A schematic of the amplification stage. L1,2: telescope for pump beam, L3: lens for pump beam focusing, PBFM: pump beam re-focusing mirror, P1-4: periscopes, IRFM1,2: IR focusing mirrors, RR1,2: retro-reflectors, PBS1,2: polarising beam-splitters, PC: Pockel's Cell, BC: Berek polarisation compensator, PO1,2: pick-off mirror, VC: vacuum chamber, BW: Brewster window, Ti:S: titanium sapphire crystal, C: Peltier cooling chamber, PD: photodiode.

This pulse is then compressed in the next stage.

3.1.1.3 Compressor

The stretched pulses are compressed by double-passing a paired double-prism compressor, shown in Figure 3.3. The prisms allow a high throughput of 80%. The use of a prism compressor reduces the slow drifts in CEP that can arise in grating compressors due to pointing instabilities [125]. The drawback of using prism compressors is the increased B-integral that limits the pulse energy to $\sim 1\,\mathrm{mJ}$. Even at these energies some self-steepening can be seen in the blue-part of the spectrum leading to a reduction of the spectral bandwidth and therefore longer pulses [126, 127]. A SPIDER measurement of the compressed output is shown in Figure 3.4. The pulse duration after the compressor is 30 fs, which is about 1.3 times the Fourier transform limit

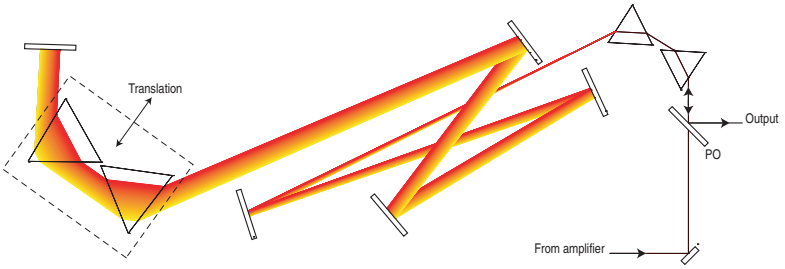


Figure 3.3: A schematic of the Femtolaser prism compressor. It is arranged in a folded, four-prism Proctor-Wise configuration with LaK16A prisms [124]. By using this highly dispersive material, the prism separation can be reduced compared to fused silica prisms. The amount of glass of the second prism pair in the prism compressor can be changed to tune the pulse duration by changing the overall dispersion. Taken from [70]

of 23 fs. This is due to remaining third and fourth order terms that cannot be compensated for. In principle this can be compensated with an adaptive phase shaping method and the pulse duration even reduced by more spectral shaping before the amplification process [128].

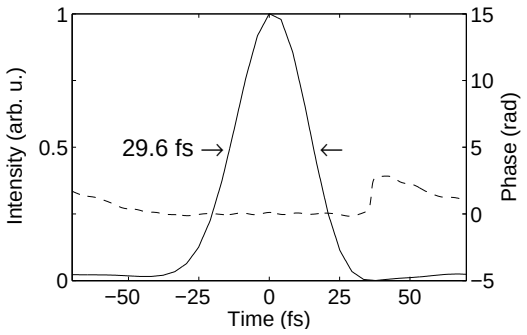


Figure 3.4: SPIDER measurement of the compressed output of the CPA system

3.1.2 Carrier Envelope Phase Stabilisation

There are two stages of control that are required in order to lock the CEP slip such that every pulse has the same CEP [129]. The fast-loop stabilises the slip in the oscillator and the second stage corrects for slow drifts that occur in the stretcher, amplification and compression stage. Both of these stages measure the CEP slip interferometrically with an f-to-$2f$-interferometer and feed back to an acousto-optic modulator (AOM) that modulates the power of the oscillator pump beam.

3.1.2.1 Fast Loop

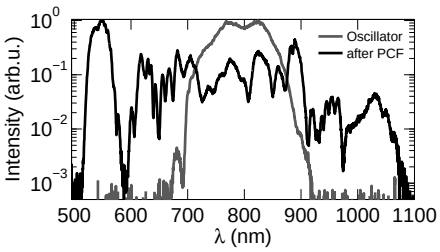


Figure 3.5: Spectrum of the oscillator before and after broadening in the PCF of the CEP fast loop

The fast loop measures the CEP of the oscillator and has already been described with reference to Figure 2.19 in section 2.1.7.1. For the f-to-$2f$ interferometer, the spectrum of the oscillator has to be broadened and this is done by means of a photonic crystal fibre (PCF) as shown in Figure 3.5. This octave spanning spectrum is then split by a dichroic beam splitter and the red part of the spectrum is frequency doubled in a periodically poled lithium niobate crystal (PPLN). Both parts are recombined with a polarising beam splitter and spectrally dispersed with a grating. An avalanche photo diode is used to measure the beat signal of the two green parts of the spectra. Since the repetition rate of the oscillator is much higher than the repetition rate of the amplified output (80 MHz compared to 1 kHz), not every oscillator pulse has to have the same CEP. It is sufficient to lock the CEP slip such that every amplified pulse has the same CEP. In our system, the CEP slip

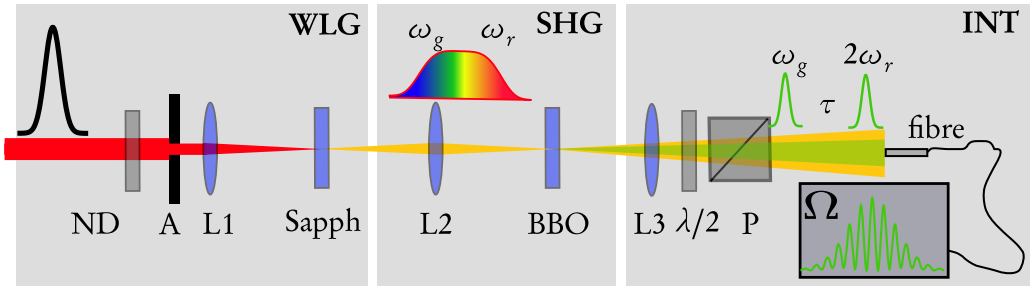


Figure 3.6: The optical layout of the collinear f-to-2f interferometer described in the text. ND: neutral density filter, A: adjustable aperture, L1,23: lens, Sapph: sapphire plate, BBO: second harmonic crystal, $\lambda/2$: half-wave plate, P: polarizer, Ω: spectrometer

is stabilized to $\pi/2$ by locking the beat signal to a quarter of the oscillator repetition rate ($\sim 20\,\mathrm{MHz}$). This will guarantee that every amplified pulse has the same CEP. The locking is done by varying the oscillator pump power by an acousto optic modulator (AOM) as mentioned before. The dynamic range of the AOM is mainly limited by the modelocking stability range of the oscillator. Therefore, for additional coarse adjustments, there are computer controlled intra-cavity wedges. These are used to control the CEP slip when the AOM voltage drifts too far away from the optimal position and allows for active CEP stabilisation over a whole day.

As mentioned above, the CEP slip is locked to a quarter of the repetition rate (see Equation 2.38), therefore every fourth pulse out of the oscillator has the same CEP. The pulse picker of the amplifier is timed such that the difference between consecutive amplified pulses is a multiple of four, and therefore every pulse out of the laser has the same CEP.

3.1.2.2 Slow Loop

Further measures have to be taken to lock the CEP for the entire CPA system. There are slow drifts of the CEP, mainly due to beam pointing fluctuations on a time scale of 1 s or higher [129, 130]. This translates directly to a change in refractive index due to the nonlinear part of the refractive index (see Equation 2.18). Additionally, changes in beam pointing and refractive index changes in air as a result of temperature or air flow, will alter the CEP and have to be corrected. This is again detected with an f-to-$2f$ interferometer, but due to the more intense pulses (overall gain: 10^6) this can be done with a slightly different setup in a collinear geometry, shown in Figure 3.6. A small portion of the beam ($\sim$ 3%) is picked off from a back-reflection of a piece of glass. This is then focussed onto a sapphire (Sapph) plate to generate a super-continuum with an over-octave spanning bandwidth. An adjustable neutral density filter (ND) and an iris (A) before the focusing lens (L1) are used to adjust the intensity at the sapphire plate and generate a stable white light filament. This is then refocused into a Beta Barium Borate crystal (BBO) cut for type-II second harmonic generation (SHG) around 1000 nm. A half-waveplate ($\lambda/2$) in conjunction with a polarising beam splitter (PBS) is used to adjust the relative powers of the fundamental green (ω_g) and the second harmonic ($2\omega_\mathrm{r}$) to optimise the contrast. The time delay τ between the two pulses is achieved simply with the intrinsic dispersion of the system, which adds up to a delay of $\sim$ 300 fs. The interferogram (Ω) is recorded with a spectrometer (Ocean Optics, USB 2000) and the CEP is extracted with Fourier processing techniques [81]. There is some intrinsic phase jitter resulting from the phase noise added in the white-light generation process. It has been shown, that a pulse energy fluctuation of 1% corresponds to a phase shift of $\sim$ 80 mrad [129].

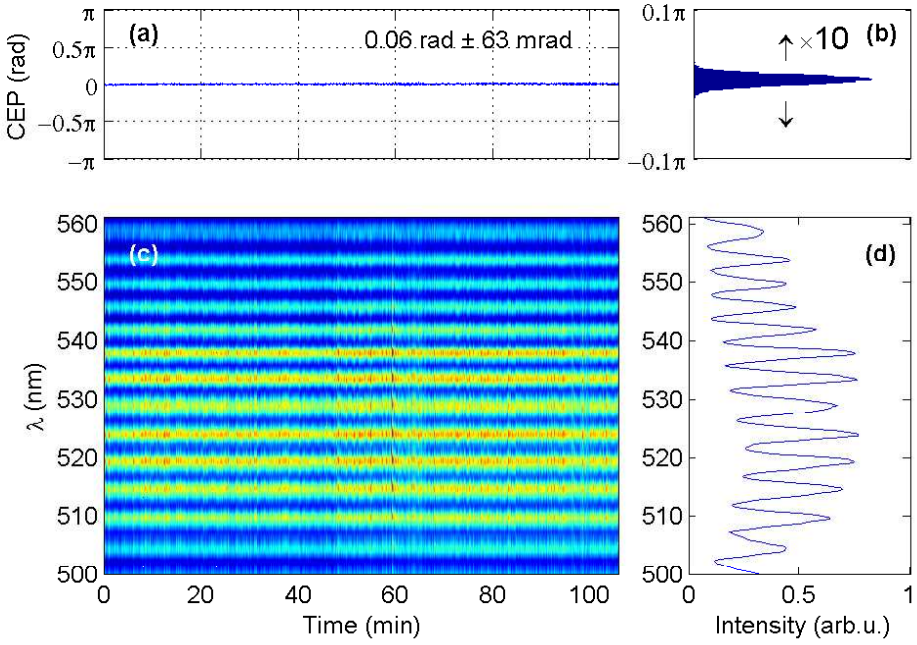


Figure 3.7: A typical measurement of the CEP after the compressor over a period of two hours, which shows the retrieved CEP value (a) showing a mean value of 0.06 rad with a standard deviation of 60 mrad. The histogram of the CEP values magnified by a factor ten with respect to the graph in (a) is shown in (b). (c) the measured interferograms over time and the averaged spectrum (c).

The reconstructed CEP is compared to a user defined value and an error signal is generated from the difference of these two values. The error signal is then used to compensate for the slow drifts of the CEP by applying a dc offset to the AOM that is also used to stabilise the oscillator. Alternatively, the second prism pair inside the compressor can be used to compensate for the slow drift. This turns out to be necessary in case the oscillator lock is not sufficiently stable, i.e. if the feedback signal to the AOM has a large amplitude ($\langle U \rangle_{\mathrm{rms}} > 25\,\mathrm{mV}$). To change the CEP during an experiment, one can

either change the dc offset of the AOM or, for a more stable operation change the CEP by inserting a pair of thin glass wedges before the experiment. This changes the CEP due to the difference in phase- and group-velocity (see Equation 2.39).

The f-to-$2f$ interferogram and the calculated CEP over a period of two hours is shown in Figure 3.7.

3.1.3 Overview

In this section I have presented the front-end laser used in our laboratory. The CPA system is seeded with a femtosecond oscillator that is amplified in a 9-pass Ti:Sapphire amplifier with a total gain of 10^6 . It is subsequently compressed by a four prism compressor.

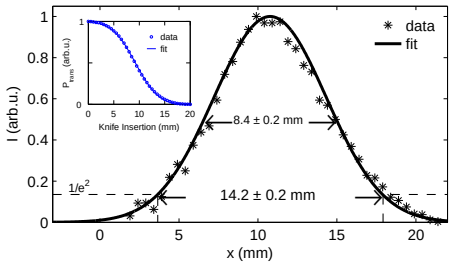


Figure 3.8: Knife insertion beam profile measurement of the Femtolaser drive laser.

It delivers a compressed output of 750 µJ pulses centred at 800 nm with a duration of 30 fs and a repetition rate of 1 kHz. The beam diameter measured at $1/e^2$ out of the compressor is 14 mm with a divergence of $\sim$ 1 mrad and an $M^2 \lesssim 1.2$. The rms pulse to pulse energy fluctuations are $\lesssim$ 1%. The pulses can be reliably CEP stabilised and controlled over several hours.

This beam is now used to generate sub 4 fs few-cycle pulses via hollow-fibre pulse compression as described in the following chapter.

3.2 Hollow Fibre Pulse Compression

In this section I describe the generation of ultrashort optical pulses from the commercial CPA laser described in the previous section. The 30 fs pulse is spectrally broadened in a hollow fibre and subsequently compressed using a chirped mirror setup. I will describe the gas-filled hollow fibre setup and briefly discuss two different operation modes, statically-filled and differentially pumped.

As discussed in subsection 2.1.5, hollow fibre pulse compression relies on the spectral broadening by self-phase modulation (SPM) in a gas-filled hollow fibre. The fibre acts as a dielectric waveguide, allowing for a long interaction length at a high intensity. This method allows the generation of high-power (up to 5 mJ [131]), few-cycle laser pulses [41, 132] at kHz repetition rates.

We use a differentially-pumped hollow fibre setup [39, 133], where the entrance of the fibre is under vacuum and the gas pressure gradually rises along the fibre. This leads to a reduction of ionisation and therefore a reduction of defocusing at the entrance compared to a statically filled hollow fibre. Therefore a good transmission through the fibre can be maintained over a large range of input pressures before defocusing affects the coupling into the fibre or ionisation decreases the stability of the broadening [39, 133, 134]. This allows to tune the pulse duration over a large range (5-30fs) while keeping the pulse duration transform limited, by changing the gas pressure.

The spectral broadening introduced by SPM can be approximated for a Gaussian pulse in the absence of dispersion by [46]:

$$\Delta\omega = \frac{0.86}{T_0} \int_0^L n_2 p(z) \omega_0 / c A_{\text{eff}} P(z) \mathrm{d}z, \tag{3.1}$$

where z is the distance along the fibre, T_0 the $1/e$ temporal half-width of the input pulse, L the length of the fibre and A_{eff} the effective mode area

in the fibre. The nonlinear response and pressure of the gas are given by n_2 and $p(z)$ respectively. $P(z)$ is the peak power along the fibre, given by $P(z) = \eta P_0 e^{-\alpha z}$, where P_0 is the peak incident power, η and α the coupling efficiency and the attenuation coefficient respectively (see also Section 2.1.5.1 and 2.1.5.2).

In the case of a differentially pumped hollow fibre, the pressure along the fibre can be written as [133]:

$$p(z) = \sqrt{p_0^2 + \frac{z}{L}(p_L^2 - p_0^2)}, \tag{3.2}$$

where p_0 and p_L are the pressures at the entrance and exit respectively. If $p_0 \ll p_L$, the average pressure along the fibre is $(2/3)p_L$.

3.2.1 Hollow Core Fibre: Optical Setup

The experimental setup is shown in Fig. 3.9. As mentioned in subsection 2.1.5, the maximum energy throughput is obtained, when the laser propagates in the EH_{11} fundamental hybrid mode of the fibre. In order to couple into this mode and achieve maximum coupling efficiency, the focal spot has to be carefully matched to the size of the fibre mode. Here, the output of the CPA laser is coupled into the hollow fibre using 1.5 m focal length anti-reflection coated lens. A small amount of the beam is picked off by a 3% beamsplitter. This then passes through an anti-reflective (AR) coated window, is re-collimated and then used to monitor the slow CEP drift as described in subsubsection 3.1.2.2. The residual reflection of the AR-window is used to monitor the focal position and correct for slow-term pointing drifts of the CPA output, to ensure stable coupling over extended periods of time. The hollow fibre sits in a supporting glass capillary with

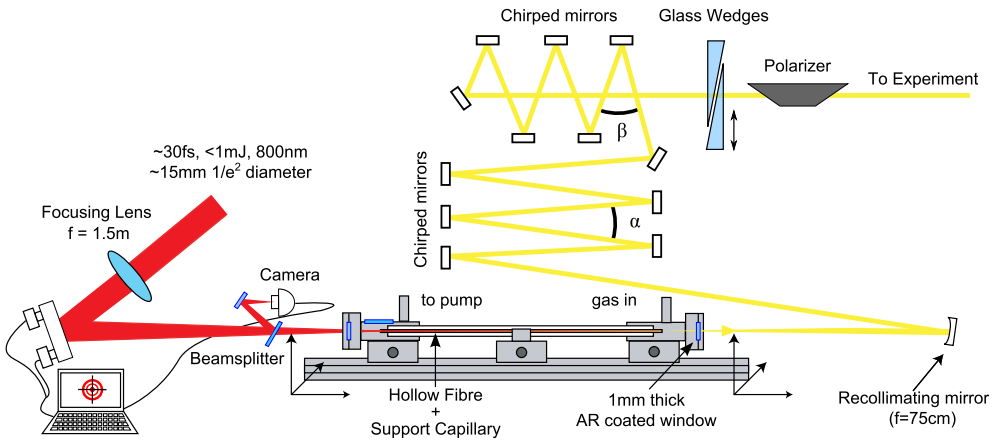


Figure 3.9: Schematic of the differentially pumped hollow fibre setup. The CPA output is coupled into the hollow fibre and then re-compressed with chirped mirror pairs afterwards. The fibre entrance is under vacuum and the gas is let into the fibre exit. A CCD camera measures the locus of the focus and controls the focusing mirror to compensate for slow term drifts.

an outer diameter of 6 mm. Tubes are attached to both ends of the support capillary using standard O-ring seals to be able to fill the fibre with gas. The beam enters and exits the fibre setup through 1 mm AR coated low dispersion windows. The beam is then re-collimated and compressed with broadband chirped mirrors. An ultra-broadband compression stage, uses 10 bounces from double-angle technology chirped mirrors (PC52, Ultrafast Innovations) with $\alpha = 5°$ and $\beta = 20°$, providing a very flat phase over a spectral bandwidth of 550-1050 nm, supporting sub-4 fs laser pulses [9]. The GDD introduced by these mirrors is shown in Figure 3.10.

3.2.2 Spectral Broadening

The main goal of using a hollow fibre is the generation of a broadband spectral continuum. The broadening in the fibre can be tuned with the choice of gas,

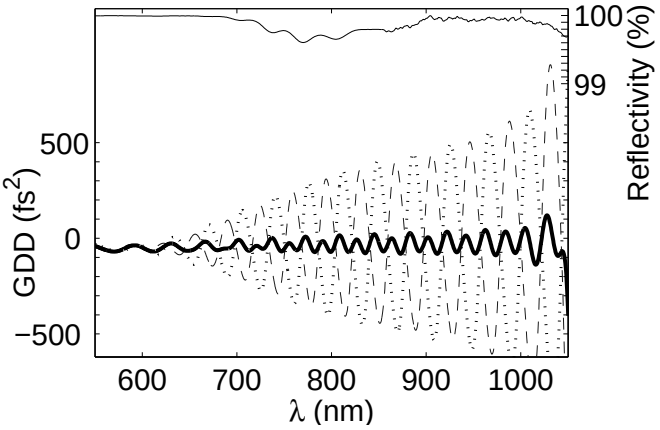


Figure 3.10: Group delay dispersion and reflectivity for the Ultrafast Innovation double-angle technology chirped mirrors. Average GDD (thick solid line), GDD for AOI of 5° (dotted line), GDD for AOI of 20° (dashed line)

the intensity along the fibre and the gas pressure in the hollow fibre. It is therefore possible to obtain transform limited pulses over a range from 4-30 fs by merely tuning the gas pressure in the hollow fibre. In Figure 3.11 the spectra and the transform limited pulse duration are shown for a range of neon pressures in a 1 m long fibre with an inner diameter of 250 µm. The broadening is shown for the differentially pumped and the statically filled conditions.

The input power into the fibre is 560 mW. The overall transmission for the differentially pumped condition stays constant over the whole pressure range and is 56%, leading to an output power of ~ 310 mW. In the statically filled case, the transmission slightly decreases from 54% at 1.2 bar to 51% at 3.0 bar. The broadening of the two cases cannot be directly compared with the pressure. As discussed earlier, the average pressure in the differentially pumped case, $\langle p \rangle_{\mathrm{diff}}$, along the fibre is $(2/3)p_{\mathrm{static}}$. When taking this into account, the transform limited pulse durations match each other very well.

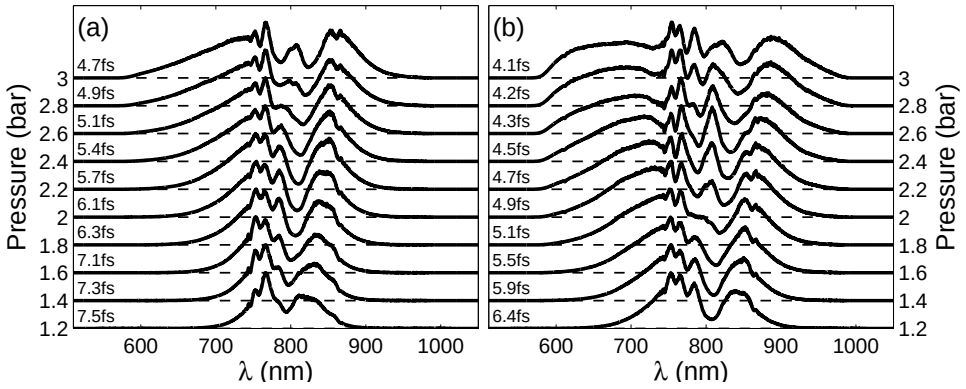


Figure 3.11: Pulse broadening in a 1 m long neon filled hollow fibre for the differentially pumped (a) and the statically filled case (b) over a range of pressures. The transform limited pulse duration is noted on the left side of each spectrum

3.2.3 Conclusion

In this section I have described the optical setup of the hollow fibre used to broaden and compress our drive laser pulses. Two different conditions, differentially pumped and statically filled fibres, have been discussed and their spectral broadening has been shown. In future, with a more energetic drive laser, it is important to be able to put more energy through the fibre. First tests with a circularly polarised input beam in addition to the differentially pumped setup have been obtained with a 3 mJ drive laser at Laboratoire d'Optique Appliqué (LOA) in Palaiseau, France. Circularly polarised input reduces the Kerr nonlinearities as well as the ionisation at the fibre entrance [135]. In addition, chirped input pulses and a larger diameter hollow fibre can be used to further increase the energy throughput [131].

Chapter 4

Characterisation of High-Intensity Sub-4 fs Laser Pulses

In this chapter I describe the complete characterisation of the sub-4 fs CEP-stabilised pulses generated in the hollow fibre setup as discussed in the previous section. Firstly, a frequency resolved optical gating (FROG) setup in a single-shot geometry is described. The difficulties arising from dealing with the large bandwidths generated in the hollow fibre are discussed and ways to overcome them are presented.

Secondly the pulse is characterised using spatially encoded arrangement spectral phase interferometry for direct electric-field reconstruction applying filters for the ancilla preparation (SEA-F-SPIDER). This is used to measure the pulse duration over the extent of the laser beam giving insight on the spatially varying pulse duration.

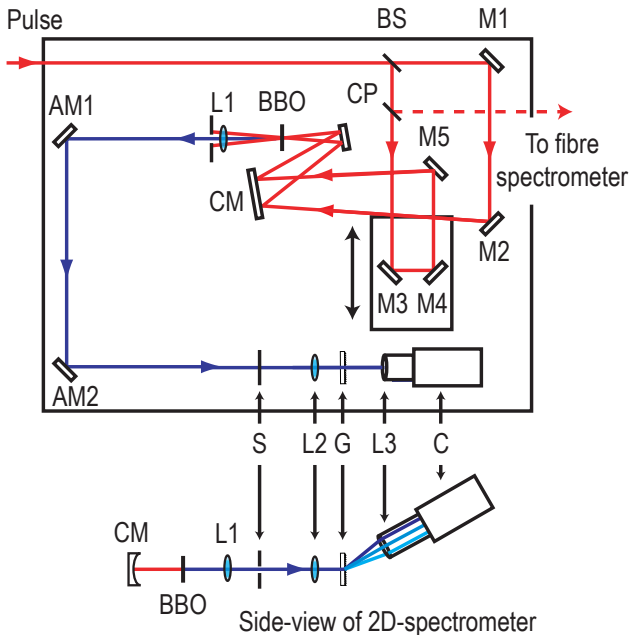


Figure 4.1: The optical setup of the FROG used for the characterisation of few-cycle pulses. BS: beamsplitter, M1-5: low dispersive silver mirrors, CP: dispersion compensating fused silica plate, CM: cylindrical mirror, BBO:beta-barium borate crystal, L1-3: positive lenses, S: slit, AM1-2: UV enhanced aluminium mirror, G: grating, C: UV sensitive camera.

4.1 Characterization of Ultrashort Pulses Using Frequency Resolved Optical Gating

Here, I discuss the Frequency Resolved Optical Gating (FROG) setup used to characterise the ultrashort pulses. I will first describe the optical setup with emphasis on the low dispersion components. In the next section I will give details about the temporal and spectral calibration methods. I will then point out the difficulties of a FROG measurement in the few-cycle regime. The crystal phase-matching and spectral response issues are analysed and the spectral-marginal correction is explained in more detail.

4.1.1 Optical Setup For a Single-Shot FROG

A single-shot second-harmonic FROG was set up to characterise the few-cycle pulse [74, 76]. The optical setup is shown in Figure 4.1. The test pulse enters the FROG and is split into two with a 50:50 beam splitter (BS). The reflected arm passes through a glass compensating plate (CP) with the same material dispersion as the beamsplitter. A translation stage is used to delay the two replicas with respect to each other. For signal enhancement, the two beams are focused by a cylindrical mirror (CM). This produces a line focus at the second harmonic crystal (BBO). The crystal plane is then re-imaged with a 7 cm focal length lens (L1) onto the entrance slit (S) of the two-dimensional spectrometer. The two dimensional spectrometer consists of two lenses (L2, L3) that re-image the slit onto a grating (G) and the grating onto a camera (C). The 480×640 pixel camera (Pike F-032B, AVT GmbH) used in the spectrometer has a dynamic range of 12 bits and is sensitive in the ultraviolet. It is interfaced with a PC and the FROG trace as well as the temporal marginal can be monitored online.

4.1.1.1 FROG Calibration

A precise pulse characterisation using a FROG requires careful calibration. The temporal axis has to be calibrated as well as the spectral axis. Additionally the spectral response of the whole setup, including the phase-matching bandwidth, the reflectivity of the mirrors as well as the spectral response of the detector, needs to be known to obtain a reliable measurement.

Temporal Calibration In a single shot FROG, the temporal calibration is achieved by recording FROG traces over a range of delays. According to Equation 2.42, by delaying the two pulses, the FROG trace centre is moved

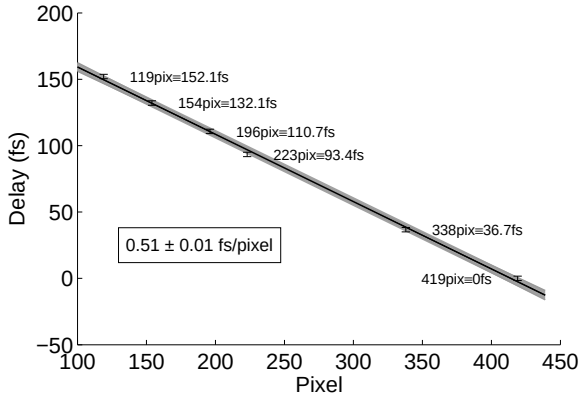


Figure 4.2: A typical temporal calibration for the FROG setup. The shaded outline represent the error of the linear fit.

spatially. The corresponding delay can be found by calculating the temporal delay for each displacement of the delay stage. The result is then fitted to a linear function as shown in Figure 4.2. The delay for our setup is measured to be 0.51 fs/pixel, leading to an overall delay window of 245 fs for our detector with 480 pixels in the delay dimension.

Spectral Calibration The spectral calibration of the 2-dimensional spectrometer is done with a Hg(Ar) spectral calibration lamp (6035 Hg(Ar), Newport). This gas-discharge lamp emits narrow lines from the excitation of mercury and argon vapour, which are related to the atomic structure of the gases. These lines are then read out and fitted to a linear function as shown in Figure 4.3

Calibration Testing One way to test the calibration and alignment of a FROG can be done by taking two traces, where the only difference between the two is the insertion of a piece of glass with a known thickness into the beam. The phases for both traces are then retrieved with the FROG algo-

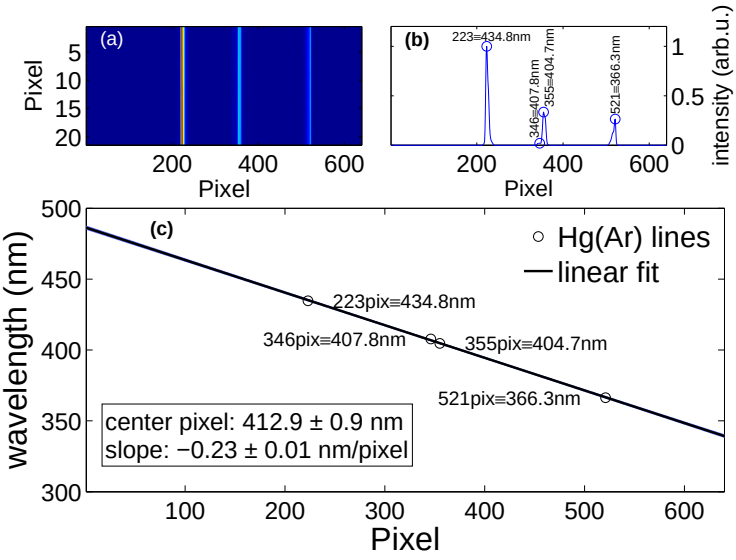


Figure 4.3: A typical spectral calibration for the FROG setup. (a) A cropped image recorded with the spectral lines of the calibration lamp. (b) Line-out in the spectral dimension with the pixel values for the maxima. (c) the linear fit of the wavelength to pixel relation.

rithm. The phase that is introduced by the glass can be accurately calculated and, if the FROG is setup correctly, should match the difference of the retrieved phases.

The phase difference and the calculated phase for a 2.5 mm piece of fused silica are plotted in Figure 4.4 and are in very good agreement with each other.

4.1.2 Dispersion Management

All the optical components before the second harmonic crystal are carefully chosen to limit dispersion effects on the measured pulse. The silver mirrors (M1-5) have a carefully designed protection layer with a very low dispersion (100767, Layertec). The reflectivity of these mirrors is 97.5 ± 0.5% over

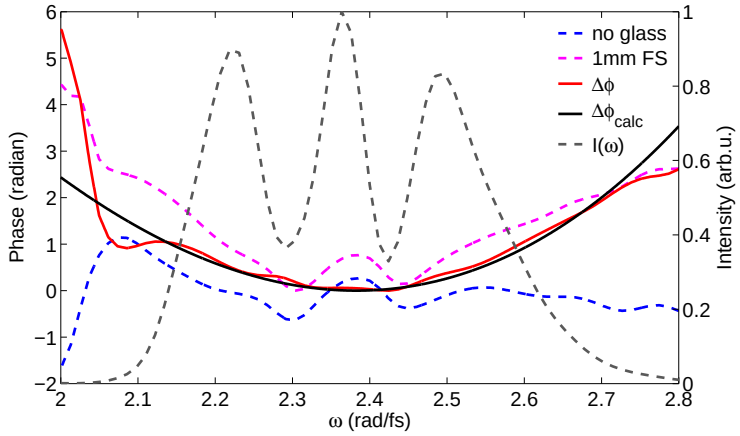


Figure 4.4: FROG calibration testing. The spectrum (black dashed) and phase for the FROG trace with no glass (blue dashed) and the trace with 1 mm of fused silica (magenta dashed). The phase difference is plotted (red) and compared to the calculated phase (black).

the range of 600– 1000 nm and the GDD in this range varies linearly from 1.5 fs^2 to -2 fs^2 (see Figure 4.5). The beam splitter (103250, Layertec) is made up of a 0.46 µm piece of fused silica with a partially reflecting coating on the front surface and an anti-reflective coating on the back. When used with s-polarised light it splits the beam evenly and the overall group delay dispersion from 550 nm to 1100 nm is nearly flat (-1.5 fs^2 - 1 fs^2) for both the reflected and the transmitted beam. This ensures that the two pulses after the beamsplitter are equal in phase and amplitude. Transmission and dispersion curves for the beamsplitter are shown in Figure 4.6.

An uncoated piece of fused silica with the same thickness as the beamsplitter is placed in the reflected beam to ensure the same overall dispersion in both beams. The reflection of the plate is used to monitor the spectrum of the testpulse and is later used to correct for the wavelength dependent response of the instrument.

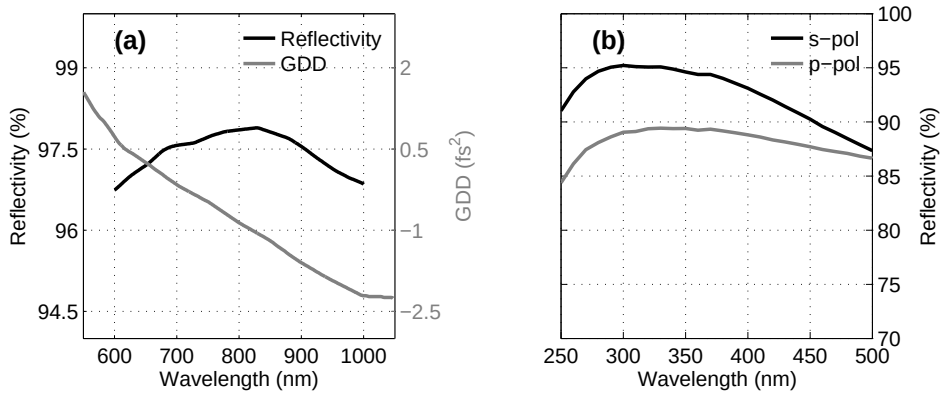


Figure 4.5: **(a)** Reflection and dispersion curves for the low dispersive silver mirrors. **(b)** Reflection curves of the aluminium mirrors used in the FROG setup. Data supplied by Layertec.

The cylindrical mirror is made from a negative cylindrical lens with a radius of curvature of $R = -51.7\,\mathrm{cm}$ (LK1002L1, Thorlabs). I coated the lens in-house with a thin layer of silver ($\sim 250\,\mathrm{nm}$) to get a focusing reflective optic. I chose not to use a protective layer to eliminate dispersive effects that arise from passing through one such layer. As a result the coating slowly

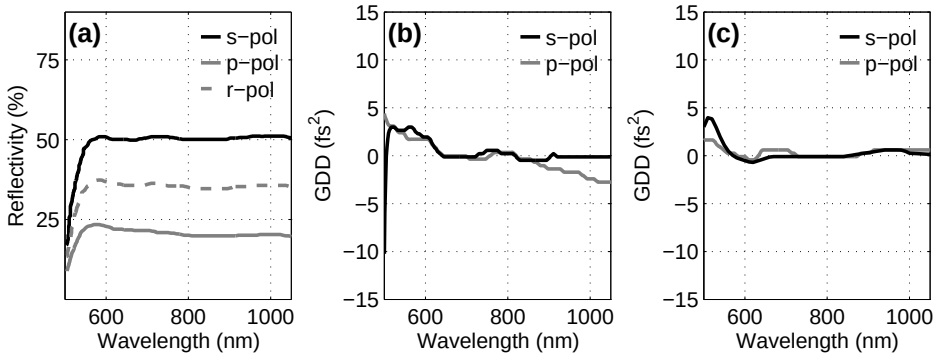


Figure 4.6: Dispersion and reflection properties of the FROG beamsplitter: reflection (a) and dispersion curves for the transmitted (b) and reflected (c) beam. Data supplied by Layertec.

degenerates, leading to lower reflection and the focusing optic has to be re-coated regularly.

The second harmonic (SHG) crystal is so thin that dispersion effects do not play a role. The role of thickness and phase-matching is discussed in the next section. After the SHG crystal, dispersion is not relevant, as the temporal measurement is converted into a spatial and spectral measurement. The spectral response on the other hand is now important, as changes in the spectral amplitude lead to changes in the retrieved pulse shape. The use of aluminium mirrors ensures efficient and almost flat reflectivity in the UV compared to silver mirrors whose reflectivity drops sharply below 400 nm.

In order to characterise the pulse duration at the target plane the optical path to the target has to be matched with the optical path to the nonlinear crystal. This has to be done very carefully for few-cycle pulses. A 3.5 fs pulse gets stretched to 5 fs by only going through 100 µm of fused silica or 17 cm of air. For an accurate measurement of the pulse duration at the target, the difference in optical path has to be smaller than these values.

4.1.3 FROG Phase-matching Bandwidth

The nonlinear crystal used for the measurement of few-cycle pulses in a FROG setup has to have a very broad bandwidth, in order to generate efficient second harmonic intensity over the whole fundamental spectrum. The second harmonic efficiency can be calculated by using Equations 2.25 and 2.27. This shows that a large phase-matching bandwidth can be achieved by using a very thin crystal, so that the influence of the phase-mismatch can be minimised.

Figure 4.7 shows a typical spectrum generated in our hollow-core fibre as well as the second-harmonic efficiency for two different crystals. The 10 µm

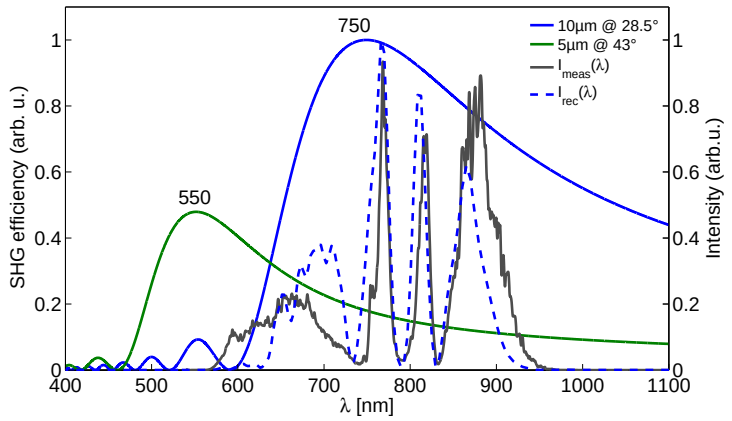


Figure 4.7: The second harmonic efficiency calculated for two BBO crystals (green and blue) and a typical output spectrum of our hollow-core fibre optimised for the maximum spectral broadening (grey) as well as the spectrum of a FROG retrieval (blue dashed). The wavelength with maximial efficiency is stated on both phase-matching curves. For more information refer to the text.

crystal cut at 28.5° (blue) was used for a chirped mirror set covering a bandwidth of 650-950 nm. It can be clearly seen that the low wavelength portion of the spectrum is poorly phase-matched. The 5 µm BBO crystal cut at 28.5° is currently used in the FROG setup and covers the whole bandwidth of our double-angle technology chirped mirrors (550-1050 nm) shown in Figure 3.10. The blue dashed line shows the spectrum of a FROG retrieval with the 10 µm crystal. It shows a well reconstructed spectrum in the region of efficient phase-matching, but cannot retrieve the spectrum in the low wavelength region. This problem is circumvented by using a thinner crystal cut at a slightly different angle in order to phase-match at a higher frequency and with a broader bandwidth.

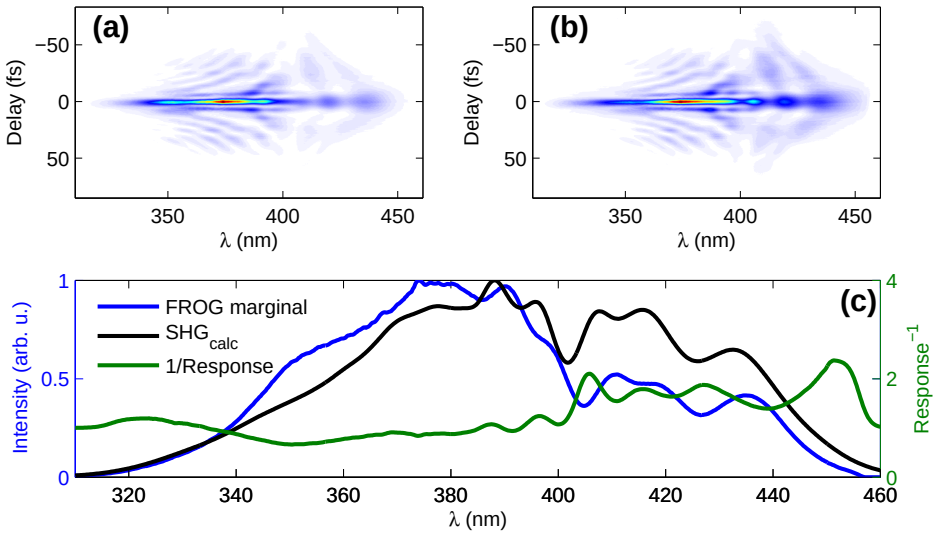


Figure 4.8: Marginal correction of a FROG trace. (a) The original recorded FROG trace. (b) The spectrally corrected FROG trace. (c) The marginal from the original trace (blue), the calculated second harmonic (black) and the correction factor, i.e. the reciprocal of the response function.

4.1.4 FROG Marginals

There are two FROG marginals referring to the sum over each of the dimensions of the 2D trace. The sum over the spectral domain leads to the temporal marginal, which, in the case of a SHG FROG, is equivalent to the single shot autocorrelation. It is therefore a very useful tool to monitor the pulse shape online and optimise dispersion to achieve the shortest pulse duration.

The second marginal, the sum over the temporal dimension, is also a useful and is used to correct for spectral response variations in a FROG setup. Bandwidth limitations are not only arising from the phase-matching bandwidth discussed in the previous section. Additionally, the transmission of the UV lens, the reflection of the aluminium mirror and the spectral response

of the 2D spectrometer all affect the spectral shape of the FROG trace. As discussed in subsubsection 2.1.8.2 these distortions can be corrected for by looking at the spectral marginal and comparing it to the second harmonic calculated from the fundamental spectrum [78, 79].

The second harmonic signal is calculated by convolution of the fundamental spectrum with itself [77]. The overall response can then readily be evaluated by dividing the spectral marginal by the calculated spectrum. This is then used to correct the FROG trace by dividing each spectral slice by this function. Figure 4.8 shows the correction factors with the marginal and calculated second harmonic as well as an original and the corresponding corrected trace.

4.1.5 FROG Results

The pulse duration out of a hollow-fibre pulse compressor was measured using the FROG described above. The fibre was statically filled with 2.4 bar of neon to obtain a spectrum with a bandwidth, $\Delta\lambda_{1/e^2} = 290\,\text{nm}$, able to support 5.2 fs. It is then compressed by 10 bounces off chirped mirrors and dispersion can be finely tuned by a pair of wedges (OA124, Femtolasers GmbH). The pulse then enters the single-shot FROG setup and a trace is measured. The traces are the average of twenty images, each taken with an integration time of 36 ms to increase singal to noise, but in principle can be taken as single-shot data. For background correction, one image was recorded with the pulse delayed such that there was no temporal overlap at the crystal and no second harmonic was generated. That background image was subtracted from the FROG trace and the spectral response was corrected by comparing the marginal with the calculated second harmonic, as discussed in the previous section. The fundamental spectrum was measured with a commercially avail-

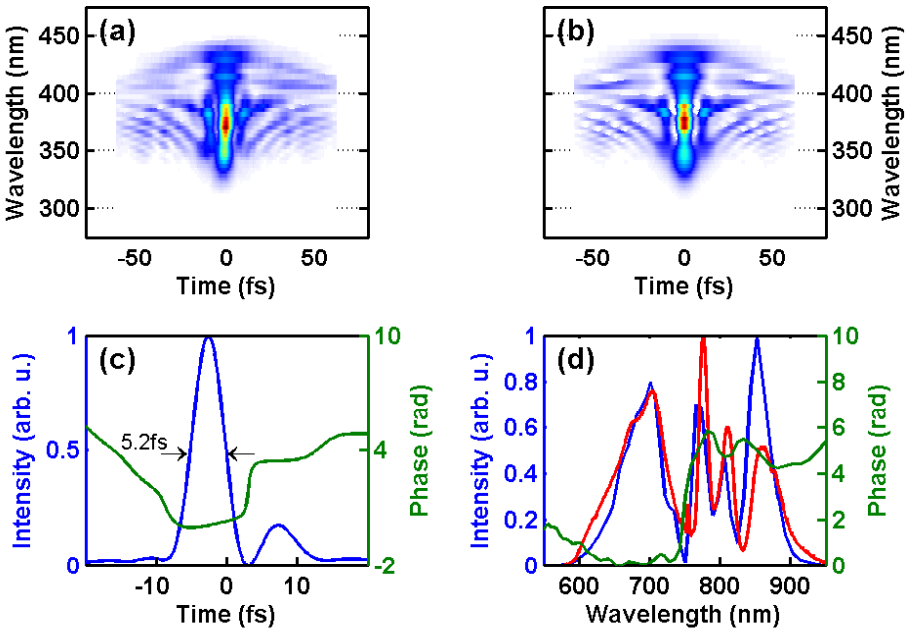


Figure 4.9: FROG results. (a) The measured FROG trace after spectral corrections. (b) The retrieved FROG trace. (c) The temporal amplitude (blue) and phase (green), showing a duration of 5.2 fs at full-width half-maximum. (d) The retrieved spectral amplitude (blue) and phase (red) as well as the directly measured spectrum of the fundamental (red).

able one dimensional spectrometer (USB2000, Ocean Optics). The spectrum is the average of 500 laser shots.

A commercially available FROG retrieval software (FROG3, Femtosoft Technologies) was used to retrieve the temporal and spectral amplitude and phase. The FROG error for the retrieval was $G = 0.0099$, where the FROG error, G, is defined as [77]:

$$G = \sqrt{\frac{1}{N^2}\sum_{i,j=1}^{N}\left|I_{\mathrm{FROG}}(\omega_i,\tau_j) - \mu I^{(k)}_{\mathrm{FROG}}(\omega_i,\tau_j)\right|^2}. \tag{4.1}$$

The FROG error is a computed rms average across the entire trace, where

N is the number of pixels used, I_{FROG} and $I_{\mathrm{FROG}}^{(k)}$ are the recorded and the k^{th} reconstructed trace. The parameter μ is chosen to minimize G to ensure a scaling of the trace that is not corrupted by noise.

The retrieved trace shows a pulse duration of 5.2 fs at full-width half-maximum, corresponding to the Fourier-transform limit supported by the spectrum. The FWHM duration is the most common measure in the ultrafast community. Nevertheless, for a structured pulse as is measured here, it is beneficial to quote other characteristics in order describe the pulse. Pulse contrast, the existence of a post and/or pre-pulse as well as a full graph showing the temporal intensity (see Figure 4.9 (c)) give valuable insight on the structure of the pulse. In the measurement presented here, a small post-pulse with a peak intensity and overall energy of less than 20% can be seen.

The main limitation of the FROG is the spectral bandwidth of the spectrometer. It can measure 310-560 nm, limited by the grating dispersion and the size of the Charge-Coupled Device (CCD) detector.

4.1.6 Conclusion

In this chapter I have described a FROG setup suited to measure few-cycle pulses down to 5 fs. The temporal and spectral calibrations have been discussed as well as the spectral corrections from the comparison of the marginal with the calculated second harmonic from the fundamental spectrum. The calibration has been tested by comparison of two traces with and without a piece of glass of known thickness. A pulse, covering the entire spectral bandwidth of the 2D spectrometer, has been measured and retrieved. It shows a flat phase over the main pulse with a small post-pulse on the order of 20% of the main pulse.

To increase the spectral bandwidth of the apparatus, a different grating,

that is less dispersive can be used. Alternatively a camera with more pixels can be used to record the traces.

4.2 Spatially Resolved Characterisation of Sub-4fs Laser Pulses Using SEA-F-SPIDER

The laser pulse generated in a hollow-core fibre has a two-dimensional structure due to the intensity dependent broadening factor in the self-phase modulation process (refer to Equation 2.28). It is therefore of interest to characterise the pulses temporal structure spatially. Unlike the FROG method described in section 4.1, here we use spectral phase interferometry for direct electric field reconstruction in a spatially encoded arrangement (SEA-SPIDER) [136, 137].

4.2.1 The SEA-SPIDER Setup

The setup used to characterise the pulses from the hollow fibre is shown in Figure 4.10. The pulses from the CPA system are broadened in a hollow fibre (HCF) and compressed by a chirped mirror setup (CMs) before entering the SEA-F-SPIDER. The first beamsplitter (BS1) reflects a small portion (6%) of the beam, the testpulse, and the rest of the pulse is used to prepare the two ancillae beams. Their polarisation is rotated by a $\lambda/2$-waveplate before they get split up by a 50:50 beamsplitter (BS2). Each of them then passes a narrow transmission window filter ($F_{A,B}$, MaxLine, Semrock) resulting in two beams with slightly shifted wavelengths as depicted in the inset on the bottom right. The transmission wavelength of beam A is set to a constant value, $\lambda_A = 807.4\,\text{nm}$. The wavelength of beam B, and therefore the spec-

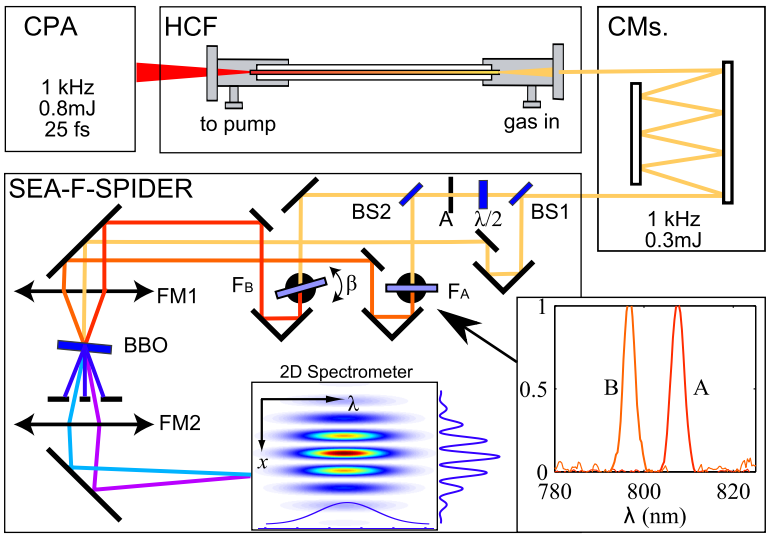


Figure 4.10: SEA-F-SPIDER setup: CPA: chirped pulse amplification system, HCF: hollow-core fibre, CMs: chirped mirrors, BS1/2: beamsplitter, $\lambda/2$: halfwave-plate, A: aperture, $F_{A,B}$: colour filters, FM1/2: focusing mirror, BBO: nonlinear crystal. Bottom right: Transmission spectra of the narrowband filters $F_{A,B}$.

tral shear $\Omega = \omega_A - \omega_B$, can be automatically adjusted by rotating the filter with a small servo-motor (S3003, Futaba). All beams are then focused with a 30 cm focal length spherical mirror (FM1) onto nonlinear crystal (BBO). The BBO crystal (L=20µm, $\theta = 43°$, Crystech Inc.) is cut for type-II phase-matching with a sufficient phase-matching bandwidth (450 nm to > 2.5 µm). To ensure a homogeneous up-conversion intensity across the focus of the testpulse, the ancillae beams pass through an adjustable iris (A) to ensure a larger focal spot size. A spatial filter (SF) blocks all the unwanted beams, the fundamental second harmonic from the individual beams, whereas the up-converted sum-frequency beams are re-imaged onto the entrance slit of a two-dimensional spectrometer with a 10 cm focal length spherical mirror

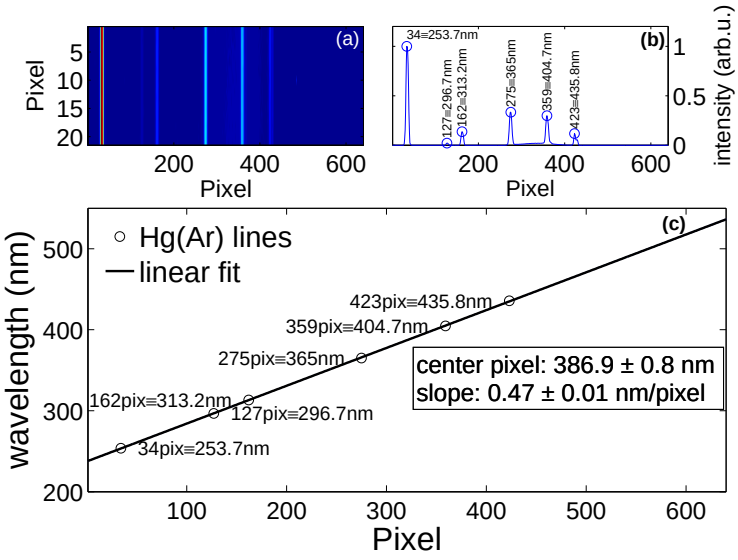


Figure 4.11: A typical spectral calibration for our SPIDER setup. (a) A cropped image with spectral lines of the calibration lamp. (b) Lineout in the spectral dimension with the pixel values for the maxima. (c) The linear fit to the wavelength to pixel relation.

(FM2).

The SPIDER traces are recorded by a broadband astigmatism-free imaging spectrometer [138] consisting of a 150 l/mm pitched grating (Edmund Optics) and a UV sensitive 640 × 480 pixel, 12 bit CCD camera (Pike F-032B, AVT GmbH). The SPIDER interferograms are recorded in the first order of the grating and the residual IR light is blocked in the imaging plane.

4.2.1.1 Calibration

The calibration of a SPIDER is different to the calibration of a FROG. There is no time axis that needs to be calibrated and the spectral response is not

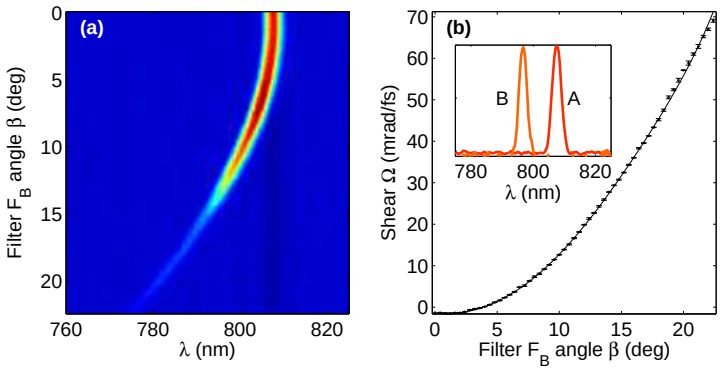


Figure 4.12: Shear calibration. (a): The transmission spectrum of filter F_B is recorded as a function of the filter angle β. (b) The resulting spectral shear as a function of the angle. Solid line: polynomial fit. Inset: Transmission of the filters.

important, as long as the signal to noise is not affected by it. There are two parameters that need to be calibrated, the wavelength axis of the spectrum and the spectral shear between the two ancillae beams.

Spectral Calibration The spectral calibration of the 2-dimensional spectrometer in the SPIDER setup is done as described in section 4.1.1.1. A mercury argon calibration lamp (6035 Hg(Ar), Newport) emits sharp lines at known wavelengths. These lines are recorded by the spectrometer setup and are used to calibrate the wavelength axis by fitting a linear function to is, as shown in Figure 4.11.

Spectral Shear Calibration In this setup, filters are used for ancilla preparation rather than a strongly chirped pulse [83]. The calibration of the spectral shear, Ω, and the upconversion frequency, ω_{up}, can be done by simply blocking the testpulse and removing the spatial filter. The ancillae beams then enter the spectrometer and can be recorded directly as shown in the

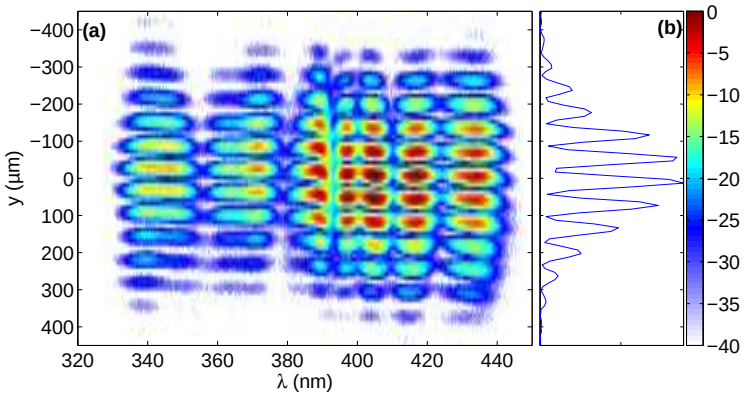


Figure 4.13: (a): Example SEA-F-SPIDER trace of a pulse after propagating through a 1 m differentially pumped hollow-core fibre filled with 1.0 bar of argon for a shear of $\Omega = 24\,\mathrm{mrad/fs}$ on a 40 dB color scale. (b): Spatial lineout at 404 nm showing the spatial fringes. Adapted from [9].

inset of Figure 4.10. The spectral shear is found by cross-correlating the spectrum from ancilla B with the spectrum from ancilla A. This can either be monitored online during a SPIDER measurement or calibrated beforehand by measuring the transmission of filter F_B as a function of angle. A measurement of the spectral shear over the rotation of F_B is shown in Figure 4.12. The filter is rotated with a stepper motor, while filter F_A stays fixed in this measurement with the transmission centred at 807.4 nm or 2.333 rad/fs. We repeated the angle scan multiple times and get a standard deviation of 0.8%, mainly due to the backlash in the gearbox of the stepper-motor.

4.2.2 SPIDER Trace

The trace of a SEA-SPIDER is given by the following equations. Consider a pulse with a field:

$$E(y,t) = \int_{-\infty}^{+\infty} A(y,\omega)\, \exp\left[i\phi(y,\omega) - i\omega\, t\right] dt, \tag{4.2}$$

where $A(y,\omega)$ and $\phi(y,\omega)$ are the spectral amplitude and phase, respectively, and y is the transverse spatial coordinate. The SEA-SPIDER trace is then given by [9]:

$$\begin{aligned} S(y,\omega) =& |E(y,\omega)|^2 + |E(y,\omega-\Omega)|^2 + \\ & 2|E(y,\omega)|\,|E(y,\omega-\Omega)| \times \\ & \cos\left[\phi(y,\omega) - \phi(y,\omega-\Omega) + \Delta k y\right], \end{aligned} \tag{4.3}$$

where Ω is the spectral shear and Δk is the difference of the wavevectors arising from the angle between the two signal beams. The complete temporal field $E(y,t)$ can be reconstructed from $S(y,\omega)$ for every spatial position y_i, leading to a spatially resolved, single shot characterisation of the pulse. Note that this is not the same as a spatio-temporal measurement, since the absolute phase between different spatial coordinates, y_1 and y_2, remains unknown. For a spatio-temporal measurement, a separate measurement is necessary [136]. An example of a SEA-F-SPIDER trace is shown in Figure 4.13.

4.2.3 Experimental Results

We have characterised a few-cycle pulse that was generated from our CPA + hollow fibre system described in section 3.1. The 25 fs pulse gets broadened in the 1 m long differentially pumped hollow-core fibre that is filled with 1 bar of argon at the exit of the fibre. The pulse is then compressed by 10 bounces on double-angle technology chirped mirrors before entering the SEA-F-SPIDER setup.

We record two SPIDER traces, the first one for calibration with $\Omega = 0$ and the second one with a shear of $\Omega = 24\,\mathrm{mrad/fs}$. Each of the final images is the mean of 25 images that were taken with an exposure of 20 ms (equivalent to a 20 shots). The pulse can then be reconstructed by retrieving the

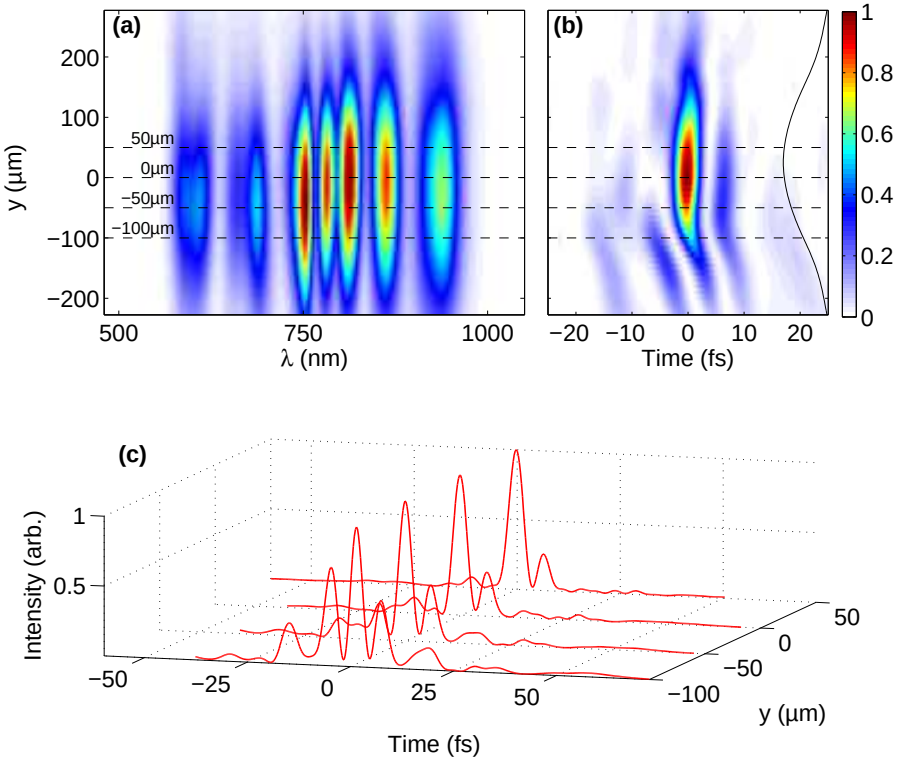


Figure 4.14: Spatially resolved reconstruction of a pulse out of a hollow-core fibre compressed with chirped mirrors. (a): Spatially resolved spectrum. (b): Reconstructed temporal intensity. Line-out on the right: spatial profile in y-direction (here: vertical). (c): Temporal line-outs at positions indicated by the dashed lines in (a) and (b).

phase, $\theta(y, \omega)$, of the interferogram recorded with our CCD. The phase can be written as:

$$\theta(y, \omega) = \phi(y, \omega) + \phi(y, \omega - \Omega) + \Delta k\ y. \tag{4.4}$$

The phase-gradient $\theta(y, \omega)$ can be reconstructed from the trace by using a 2D Fourier-filtering routine and the spectral phase at every position y_i, $\phi(y_i, \omega)$, of the pulse can be reconstructed after subtracting the phase from the calibration shear, $\theta_0(y, \omega)$, for $\Omega = 0$. From this, the temporal electric field,

$E(y_i, t)$, and intensity, $I(y_i, t)$, at every individual spatial position can be calculated.

Figure 4.14 shows a two dimensional pulse reconstruction derived from our laser system. The 2D spectrum is shown in Figure 4.14 (a). The centre wavelength is shifted to $\lambda_0 = 772\,\text{nm}$ in the self-phase modulation process. Figure 4.14 (b) shows the temporal intensity for all spatial slices. The beam shows a homogeneous temporal profile in the pulse centre. It is less homogeneous in the wings of the pulse, showing multiple pulses in the region $y < -120\,\mu\text{m}$. This is outside the FWHM and less than 10% of the energy is in this area. As a measure of the homogeneity, the standard deviation of the duration, τ_{FWHM}, is 0.6% over the spatial FWHM. Figure 4.14 (c) shows the intensity lineouts for $y_i = (50, 0, -50, -100)\,\mu\text{m}$.

Fifty-two percent of the total pulse energy spread over time and space is confined within a sub-4 fs window.

The linear phase, i.e. the pulse arrival time, between the different spatial slices cannot be retrieved with SPIDER and therefore the delay between each slice is unknown. In Figure 4.14 (b) and (c) $t = 0$ was set to the first moment of the temporal lineout.

The reconstruction of a single slice through at $-50\,\mu\text{m}$ is shown in Figure 4.15. The shaded blue and red lines represent the standard deviation of the 25 images recorded, showing the stability of the pulses. The standard deviation is only large in areas with very low signal and stays within 1% in the main part of the pulse and spectrum.

4.2.4 Conclusion

In this section I have shown the spatially resolved measurement of a sub-4 fs pulse from a single-shot SEA-F-SPIDER. We have measured a 3.5 fs pulse

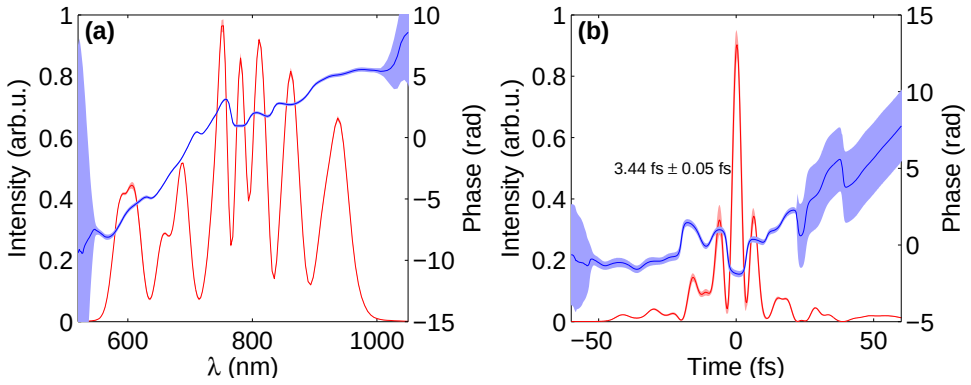


Figure 4.15: 1D SPIDER reconstruction at −50 µm. (a): Spectrum and spectral phase. (b): Temporal intensity and phase. Solid lines are the average of 25 traces and the shaded area represents the standard deviation.

with an energy of 250 µJ. This is a very useful tool in identifying spatial dependencies in the generation and optimisation of few-cycle laser pulses.

Chapter 5

Attosecond Streaking

In this chapter I will discuss the generation and characterisation of attosecond pulses. First concentrating on the generation of attosecond pulses via high harmonic generation and how these harmonics are characterised and spectrally shaped for single attosecond pulses. I will then describe the apparatus used to measure photoelectrons in the present of an IR streaking field. This allows us to measure an attosecond streaking spectrogram [115] and characterise the single attosecond pulses using a FROG-CRAB algorithm [73].

The generation and characterisation of a single attosecond pulse is an extremely difficult task and only a relatively small number of groups are able to do so. The group headed by Prof. Krausz at the MPQ in Garching were the first to demonstrate a single attosecond pulse [3] and have recently characterised the shortest optical pulse up to now with a duration of 80 as [4]. In this chapter, I describe the generation of single attosecond pulses using the same principle (see also subsection 2.2.3). A phase-stabilised few-cycle laser pulse in combination with spectral filtering restricts the photon burst to a single half-cycle, creating a continuum in the HHG spectrum that can be used to generate an isolated attosecond pulse [3–5, 110, 115, 139–141].

There are also other methods used to generate single attosecond pulses. One method is polarisation gating, where a time dependent ellipticity restricts the XUV burst to only one half-cycle of the driving laser. Using this method, Sansone *et al.* produced a single attosecond pulse with a duration of 130 as centred at a photon energy of 36 eV [112]. A variant of polarisation gating, double optical gating [113] and generalised double optical gating [114], have recently generated single attosecond pulses from multi-cycle laser fields. Here, a a small portion of the second harmonic of the driving laser field is used to overcome ionisation saturation at the leading edge of the laser pulse [114, 122, 142, 143].

5.1 Attosecond Source

In this section I will first briefly describe the few-cycle laser pulse used to generate the harmonics. I will then describe the high harmonic generation in more detail. Thirdly, the gas target and the spectrometer used to measure the XUV spectrum are discussed in more detail.

5.1.1 Few-cycle Laser Source

In our setup, we are using amplitude gating with spectral filtering to generate single attosecond pulses (SAP) [5, 139]. In order to generate high harmonics that originate from only one half-cycle within the laser pulse, a CEP stabilised few-cycle pulse is used. For this experiment, we are using the phase stabilised few-cycle laser pulses from the hollow-fibre setup discussed in section 3.2. For maximum spectral bandwidth, the fibre was not differentially pumped but statically filled with 3.0 bar of neon, resulting in a spectrum supporting sub-5-fs pulses (see Figure 5.1). The fibre output is re-collimated using a 75 cm

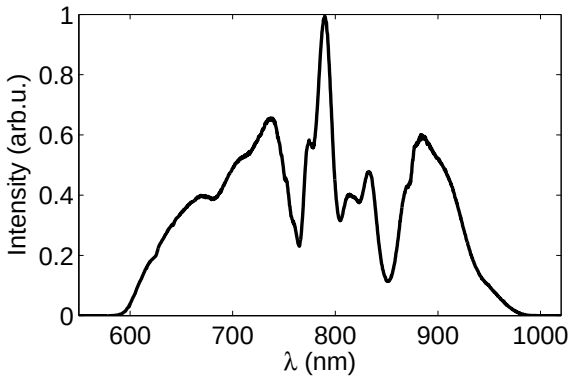


Figure 5.1: The IR spectrum before entering the HHG chamber.

focal length mirror, leading to a beam diameter of 6 mm measured at the $1/e^2$-position. Ten bounces on chirped mirrors are used to compress the pulse and motorized anti-reflective (AR) coated fused silica wedges are used to finely tune the dispersion. Additionally, the wedges can be used to set the CEP at the interaction region. This allows us to tune the pulse duration at the same time as setting the CEP to a value most suited for the generation of SAPs. To change the CEP from a sin- to a cosine-pulse, the beam has to pass an extra 25 µm of fused silica. This does not significantly alter the pulse duration – a 4.5 fs pulse gets stretched less than 5% in 25 µm of fused silica. An ultra-broadband polariser (OA513, Femtolasers GmbH) cleans up the polarisation of the laser pulse before it enters the high harmonic generation chamber.

5.1.2 High Harmonic Generation Chamber and Target

The beamline used for the streaking experiment is shown in Figure 5.2. The high harmonics are generated in the first vacuum chamber. The few-cycle IR pulse enters the chamber through a 400 µm thick AR coated window. To limit astigmatism a turning mirror reflects the beam at a small angle ($\sim 3°$)

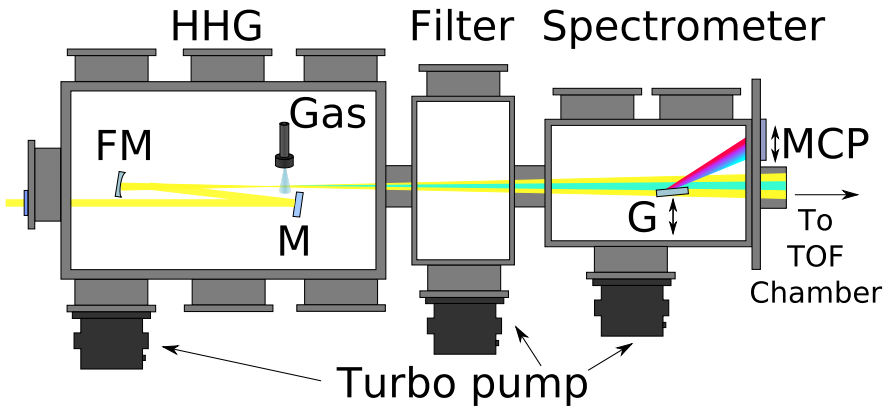


Figure 5.2: High harmonics beamline. The beam enters the HHG chamber and is focused under the gas jet (Gas). The fundamental and the harmonics propagate colinear through the filter chamber and enter the spectrometer. The grating disperses the beam spectrally and focuses it onto the imaging MCP. The grating and the MCP can be moved out of the beam such that the beam can enter the time-of-flight chamber (TOF). FM: focusing mirror, M:steering mirror.

onto an $f = 50\,\text{cm}$ focal length mirror. The gas is delivered at the focus using a pulsed kHz gas jet that is synchronised with laser. The gas jet is shown in Figure 5.3. A poppet sealed with a rubber o-ring is opened and closed by a piezo-electric disc. This releases gas from a reservoir into a small target region. The piezo is driven with a square wave with a pulse height of $\sim 120\,\text{V}$ and a width of $250\,\mu\text{s}$. The interaction region is 1.2 mm long and has a $500\,\mu\text{m}$ hole where the laser passes through.

Before entering the spectrometer, the beam traverses another chamber, the filter chamber. This chamber is used for differentially pumping ensuring that the spectrometer chamber is under low pressure so that the detector is not damaged ($< 10^{-5}\,\text{mbar}$). There is also a thin (200 nm) aluminium filter used for spectral calibration mounted on a motorised stage in that chamber.

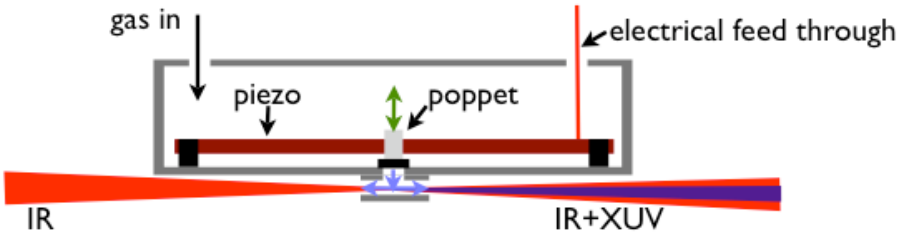


Figure 5.3: A schematic of the pulsed gas jet. The poppet is moved by the piezo disc and releases gas from the reservoir into the target area. Taken from [144]

The spot size at the focal position is measured to be 80 µm. With an energy of 250 µJ and a pulse duration of 5 fs this is equivalent to an intensity of 4×10^{14} W/cm^2, generating cut-off harmonics in neon with an energy of 95 eV.

5.1.3 XUV Spectrometer

The high harmonics are detected using a flat-field spectrometer. This allows us to obtain spatial as well as spectral information about the XUV-beam. The flat-field spectrometer consists of an XUV-grating and a micro-channel plate (MCP) coupled to a phosphor screen. The grating has a variable groove-spacing of around 1200 lines/mm and spectrally focuses the harmonics on a plane rather than a circle [145]. This allows us to change the wavelength range of the spectrometer by sliding the detector in the vertical direction from 20-200 eV, as can be seen in Figure 5.4.

The phosphor screen (P47) is imaged onto a 14 bit cooled CCD camera (CoolView FDI, Photonic Science). The MCP is made of two thin plates (∼1 mm) of conductive glass capillaries fused together at a small angle (∼ 8°). A large voltage (≈1 kV) is applied across each of the plates such that

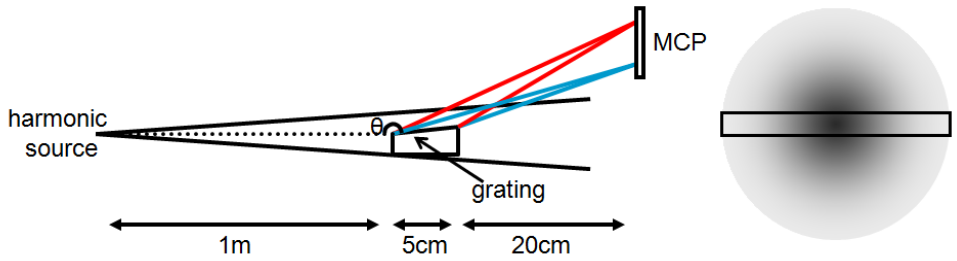


Figure 5.4: Flat-field spectrometer. Left: harmonic beam incident on the grating with 3° angle of incidence. Right: projection of the harmonic beam onto the grating. Most of the largely diverging harmonics (e.g. from the long trajectories) miss the grating and are not detected.

every channel acts as a photo-multiplier tube intensifying electrons that were created by XUV photons [146]. The phosphorescent screen then converts the electrons into visible light, $\sim 420\,\mathrm{nm}$ for P47, that is recorded with the CCD camera.

The spectrometer is calibrated by recording an image with a thin aluminium filter in the beam path. Aluminium shows a steep drop in transmission at the L-edge at $72.7 \pm 0.1\,\mathrm{eV}$, shown in Figure 5.5 [147]. In combination with the grating equation, this allows for a spectral calibration of the spectrometer.

5.1.4 High Harmonic Spectra

The high harmonics used in our setup to produce single attosecond pulses are generated in neon. The gas jet is backed with 1.2 bar of neon and a voltage is applied to the piezo gas jet such that the backing pressure in the HHG chamber is below $5 \times 10^{-3}\,\mathrm{mbar}$. This ensures a pressure in the spectrometer chamber below $10^{-5}\,\mathrm{mbar}$. The voltage across the two MCP plates and the phosphor screen is set to 2.0 kV and 1.6 kV, respectively.

The spectra are then recorded with the CCD camera. Usually images are taken with an exposure time of 40 ms and 50 images are then averaged for each spectrum. The cut-off position is tuned by slightly aperturing the beam with an iris in front of the chamber to fall into the reflection bandwidth of our MoSi mirror (92 eV with a bandwidth of 8.6 eV), which is discussed in more detail in the next section.

The harmonics are optimised by moving the z-position of the gas jet into the position with the highest yield on axis. The pulse duration is tuned with the glass wedges by looking at the cut-off position. Fine-tuning of the pulse duration is achieved by locking the CEP and scanning the wedge position. This is shown in Figure 5.6. By moving the wedges over a large range (~ 5 mm) both the CEP and the pulse duration are scanned at the same time. This allows us to set the CEP to a cosine-pulse by looking at both the maximum energy and a continuous cut-off energy region. When the spectrum

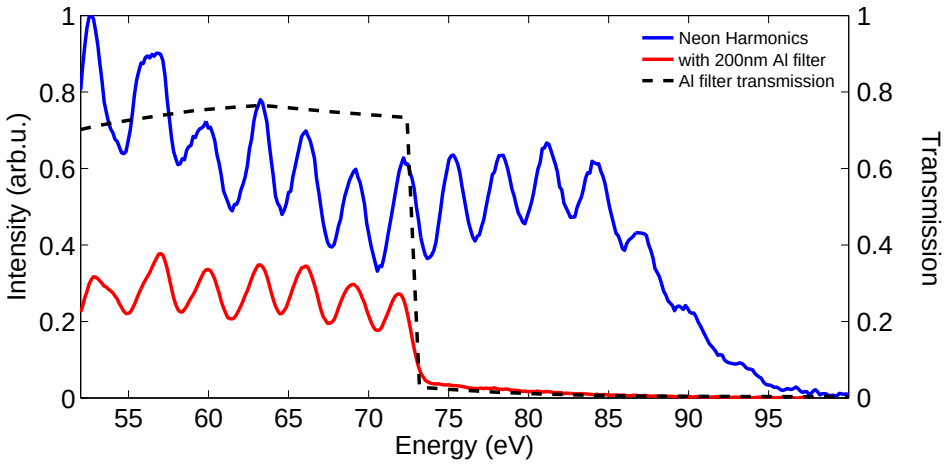


Figure 5.5: Spectral calibration for the flat-field spectrometer. Neon harmonics without a filter (red) and with a 200 nm thick aluminium filter (red) as well as the transmission of the aluminium filter (dashed black).

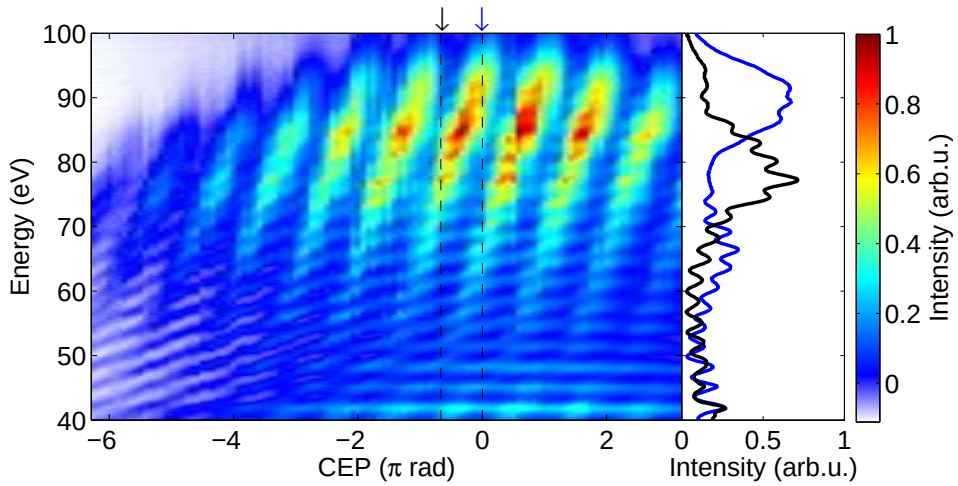


Figure 5.6: Left: CEP scan of the high harmonics. The CEP is changed by moving a thin glass wedge. Right: Spectral lineouts for the positions indicated with the arrows.

at the cut-off is continuous, the contribution to the harmonic spectra only come from one half-cycle of the laser, ensuring a single attosecond pulse. The spectral lineouts for a sine- and a cosine-pulse are plotted in Figure 5.6. From the difference in the cutoff position an estimate of the pulse duration can be made. For very short pulses, an in-situ direct measurement is extremely difficult. From the cutoff law for high harmonics (Equation 2.59) one can calculate the relative maximum intensities of the two cases:

$$I_{\mathrm{rel,cep}} = \frac{E_{\mathrm{cutoff}}(\phi = \pi) - I_{\mathrm{p}}}{E_{\mathrm{cutoff}}(\phi = 0) - I_{\mathrm{p}}} = 0.9 \pm 0.05, ; \tag{5.1}$$

where $I_P = 21.56\,\mathrm{eV}$ is the ionisation potential of neon, $E_{\mathrm{cutoff}}(\phi = \pi) = 89\,\mathrm{eV}$ and $E_{\mathrm{cutoff}}(\phi = 0) = 96$ eV The relative intensity between the cosine- and sine-pulse are related to the pulse duration. Assuming a Gaussian-shaped pulse centred around $\lambda = 780\,\mathrm{nm}$ this leads to a FWHM pulse duration of $3.4 \pm 1.9\,\mathrm{fs}$ which is shorter than the transform limit of the spectrum of 4.5 fs, but well within the error. This is a rough measurement, as the cut-off

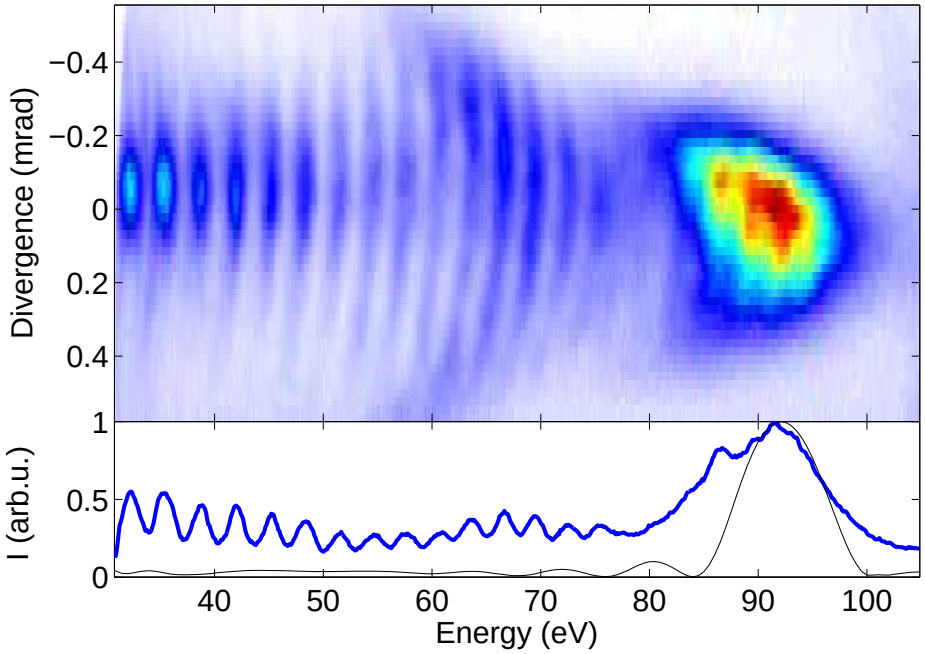


Figure 5.7: High harmonic spectrum for a cosine-pulse. Top: the spatially and spectrally resolved high high harmonics. Bottom: spectral lineout and MoSi mirror reflectivity. The reflectivity is scaled to the maximum reflectivity ($R_{max} = 31\%$).

positions are not well defined and a slight change in the relative intensities leads to a large difference in pulse durations.

The spatially and spectrally resolved image of the harmonics is shown in Figure 5.7. It shows a continuous cutoff around the reflectivity of the MoSi mirror. One can also see the second cutoff region around 75-80 eV. This is the cut-off from the next highest half-cycle [69]. This, too, allows us to give an estimate of the pulse duration. Following Equation 5.1, the relative intensity is given by:

$$I_{\mathrm{rel,HCO}} = \frac{E_{\mathrm{cutoff,HCO}} - I_{\mathrm{p}}}{E_{\mathrm{cutoff,max}} - I_{\mathrm{p}}} = 0.72 \pm 0.1, \tag{5.2}$$

where $E_{\mathrm{cutoff,HCO}} = 75\,\mathrm{eV}$ and $E_{\mathrm{cutoff,max}} = 96\,\mathrm{eV}$. This has to be compared

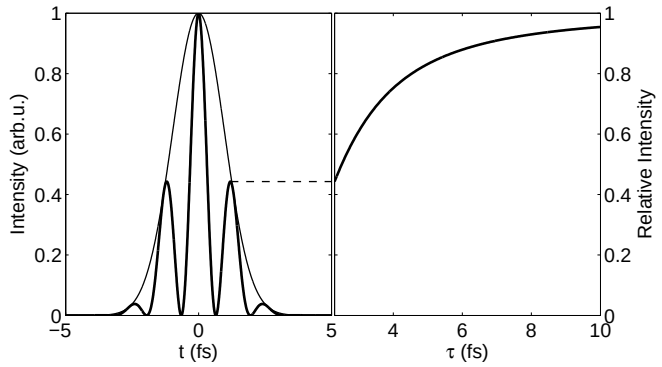


Figure 5.8: Left: Instantaneous intensity of a cosine-pulse with a FWHM pulse duration of 2.3 fs centred at $\lambda = 780$ nm. **Right:** Relative intensity of the side-peaks with respect to the main peak for a cosine-pulse as a function of pulse duration.

to the relative intensity of the main peak with the side peaks, as is shown in Figure 5.8, leading to an estimated FWHM pulse duration of 3.7 ± 1.0 fs (again assuming a Gaussian pulse shape). Both of these estimates are in agreement with each other but slightly shorter than the transform limited pulse duration supported by the IR spectrum. They cannot replace the pulse measurements discussed in the previous chapter, but are intended to be a quick way of checking the duration at the interaction region.

5.2 Time Of Flight Measurement

In this section I will describe the experimental setup used to measure the energy of the streaked photoelectrons for the attosecond streaking measurement. I will first describe the chamber with the experimental setup and its most important components. I will then give a brief description of the time-of-flight electron spectrometer, its resolution in the energy range of interest and the calibration method used.

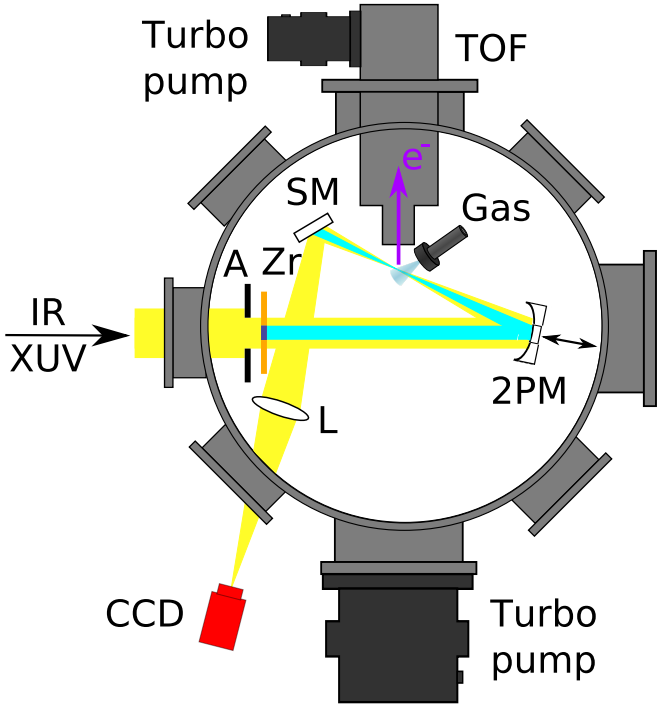


Figure 5.9: Time of flight chamber. The IR and XUV collinearly enter the chamber. An iris (A) and thin zirconium filter (Zr) adjust the IR intensity and separate the two colours. A two-part mirror (2PM) focuses the IR and XUV into the gas target (Gas). The inner part of the 2PM is movable to adjust the delay between the beams. The focal position is then re-imaged with a silver mirror (SM) and a lens (L) onto a CCD camera.

5.2.1 Time Of Flight Chamber

The main components are described briefly before more details are given. The chamber is shown in Figure 5.9. The IR and XUV collinearly enter the chamber. A motorised aperture is used to control the intensity of the IR streaking field at the interaction region. The beams then go through a two-part filter with a thin zirconium foil in the centre. The zirconium blocks the central part of the IR and spectrally filters the XUV beam. A molybdenum-silicon (MoSi) coated inner part of a two-part mirror (2PM) is mounted on

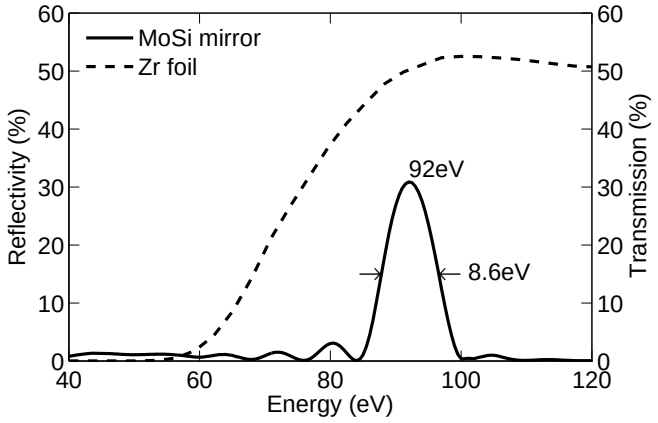


Figure 5.10: Transmission and reflectivity curves for a 200 nm thick Zr foil and a MoSi mirror.

a piezo translation stage and focuses the XUV into the gas target. The IR is focused by the outer part of the two-part mirror.

Two-part zirconium filter The split 2-part filter consists of an 4 mm diameter, 200 nm thin Zr foil mounted in the centre of a 25.4 mm diameter, 7.5 µm thick Kapton foil, which is held by an aluminium ring. The transmission of the Zr foil is shown in Figure 5.10, it blocks the IR and the low order harmonics, while transmitting energies above 70 eV. The Kapton blocks the XUV while transmitting the IR with negligible effect on the IR pulse duration.

Two-part mirror The two part mirror is manufactured from a single quartz substrate with a focal length of $f = 12.5$ cm. both, the inner part and outer part were coated with ten molybdenum-silicon layers by NTT-AT nanofabrication. The inner part has a diameter of 4 mm and the outer part has an outer diameter of 25 mm and an inner diameter of 5 mm.

The reflectivity of the MoSi mirror is shown in Figure 5.10. The peak reflectivity is 31% at 92 eV and it has a bandwidth of 8.6 eV (FWHM).

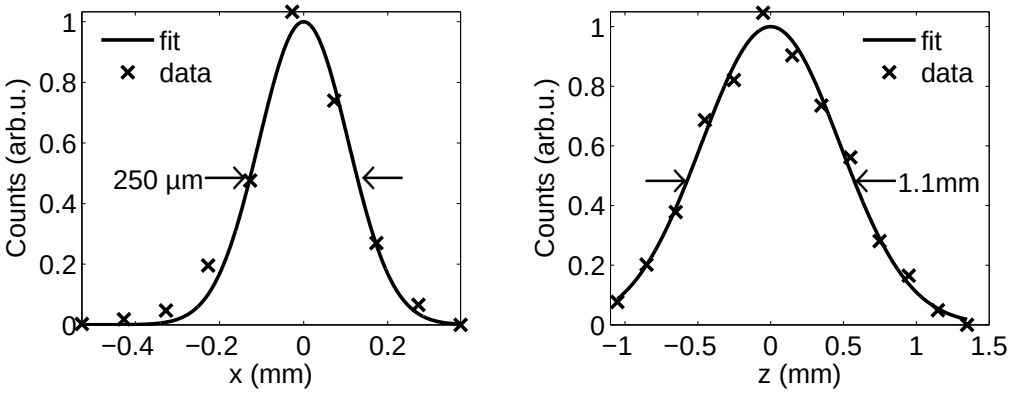


Figure 5.11: Electron count as a function of the needle position in the x- and z-direction (perpendicular to and along the beam). The x-scan was taken at the z-position with the maximum count-rate.

The inner part is mounted on a very stable piezo nano-positioner with capacitive feedback control (P-753, PI GmbH). The overall range is 12 µm ($\equiv$ 80 fs time range) with a repeatability of ± 1 nm ($\equiv \pm 7$ as).

Gas target The effusive gas target is made of a 50 mm long stainless steel syringe needle with an inner diameter of 110 µm that is mounted on an xyz-translation stage to position it accurately at the laser and XUV focus. The needle is backed by $\approx$ 1 bar of neon, leading to a background pressure in the main chamber of 2.5×10^{-4} mbar. We estimate the particle density under the needle to be $10^8 - 10^{10}$ mm^{-3} [148]. The needle is grounded to avoid charge build up. A scan of the electron counts as a function of the needle position along the beam path and perpendicular to the beam is shown in Figure 5.11.

Temporal and spatial overlap The foci of the inner and the outer part of the 2PM are re-imaged onto a CCD camera outside the chamber to ensure spatial and temporal overlap. The spatial overlap is achieved by moving the

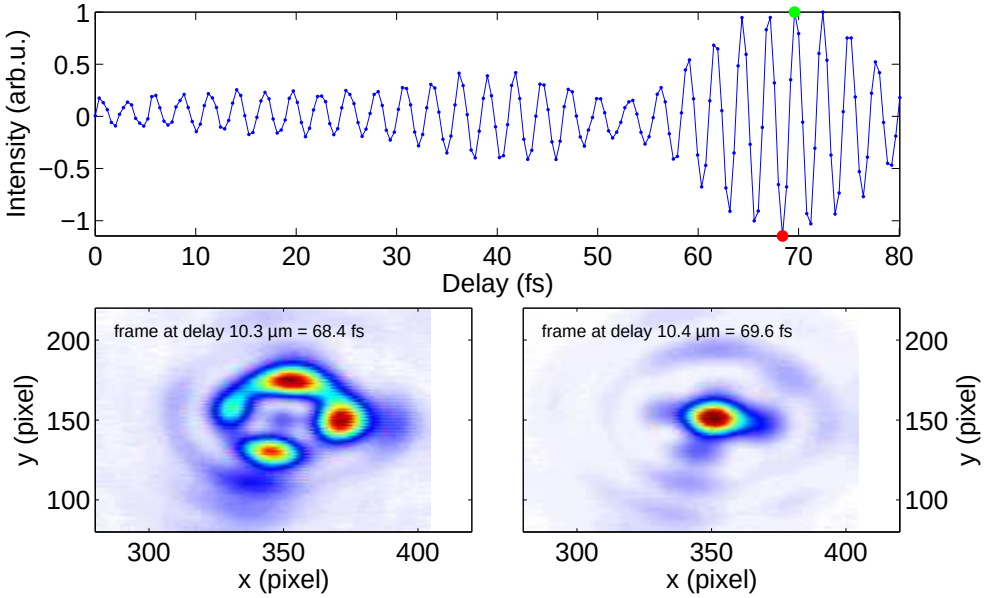


Figure 5.12: Temporal and spatial overlap measurement: Top: Integrated signal of a 7x7 pixel area around the focus as a function of delay. Right (Left): Full image at a delay indicated by the green (red) dot in the top figure. Note that there is an arbitrary delay offset.

outer part of the 2-part mirror with respect to the inner part. The position of the inner focus is recorded with the outer part blocked by the aperture. With the two-part Zr filter blocking the inner part, the position of the outer focus is moved with two actuators (PICOMOTOR™, Newport) to coincide with the inner focus.

Temporal overlap is also achieved by moving the outer part mirror using all three positioning screws. The temporal overlap is then checked by a delay scan between the inner and the outer part. The camera records images while the inner part is delayed with respect to the outer. The signal at the focus on the camera is then the first order auto-correlation, $S(\tau)$, given by:

$$S(\tau) = \int |E(t) + E(t-\tau)|^2 \, \mathrm{d}t, \tag{5.3}$$

where τ is the delay between the two beams. A delay scan is shown in Figure 5.12. Note that there is an arbitrary delay offset due to the initial offset of the inner with respect to the outer part of the two-part mirror. The temporal overlap can be seen at $\sim 69\,\mathrm{fs}$, which is not in the centre of the delay stage range. However, this overlap is measured with the two-part Zr outside the beam path. When the two-part Zr filter is in the beam path, the IR is delayed with respect to the XUV that is passing the filter. This is due to the additional optical path in the Kapton foil, while the Zr foil has a refractive index close to unity for the XUV. This shifts the temporal overlap between the XUV and the IR by $\sim 20\,\mathrm{fs}$ when using the Zr foil for an attosecond streaking measurement. Thus the temporal overlap is approximately in the centre of the delay scan range when the filter is in for attosecond streaking measurements.

5.2.2 Time-Of-Flight Electron Spectrometer

The time-of-flight electron spectrometer (TOF) is used to measure the time of flight of the photo-electrons produced by the XUV beam. It is a similar design as the TOF designed and discussed by Hemmers *et al.* [148].

The electrons get detected with a micro-channel plate (MCP) which produces an average signal pulse of 10 mV amplitude with a FWHM of 3 ns for each electron impact. This signal is amplified with a high bandwidth $\times 10$ amplifier (T1800B, FAST Comtec GmbH) and recorded with a time to digital converter (TDC) card (P7889, FAST Comtec GmbH) that has a resolution of 100 ps. The TOF has an electrostatic lens system at the entrance that can increase the energy resolution for high energy electrons ($\sim$keV) by applying a negative voltage. For the purpose of measuring electrons from our streaking setup, the electron energy is much lower ($\sim 70\,\mathrm{eV}$) and therefore no negative

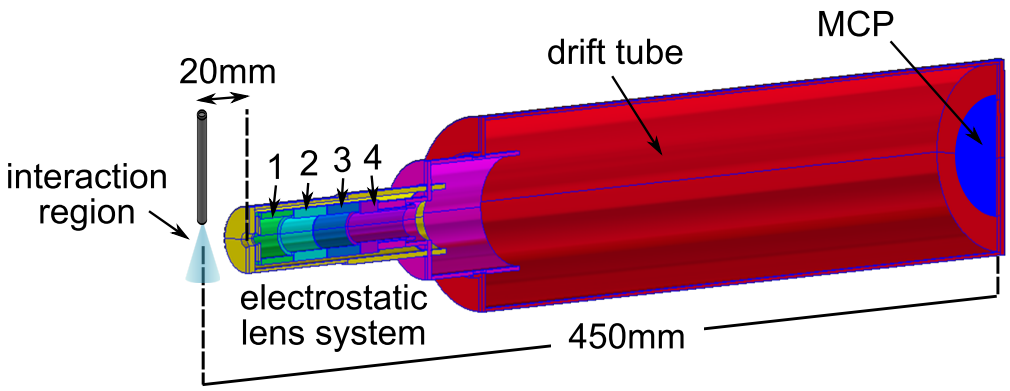


Figure 5.13: Schematic of the time-of-flight electron spectrometer. The electrostatic lens system is made of four different ring elements labelled 1-4. The drift tube is set to the same potential as the fourth element. The detector (MCP) is positioned 450 mm from the interaction region and the entrance of the TOF is 20 mm away. Note: The TOF drawing is to scale (exported from SIMION).

Table 5.1: The relative potentials of the electrostatic lens system, where V is the voltage applied to the drift tube.

V_1/V	V_2/V	V_3/V	V_4/V
0.8	0.915	0.97	1

voltage has to be applied to increase the energy resolution. On the contrary, we often apply a positive voltage to extract electrons from a larger solid angle and thereby increase the electron counts per laser shot.

The electrostatic lens system consists of four ring elements as can be seen in Figure 5.13. The relative potentials applied to them are fixed. The ratios are shown in Table 5.1.

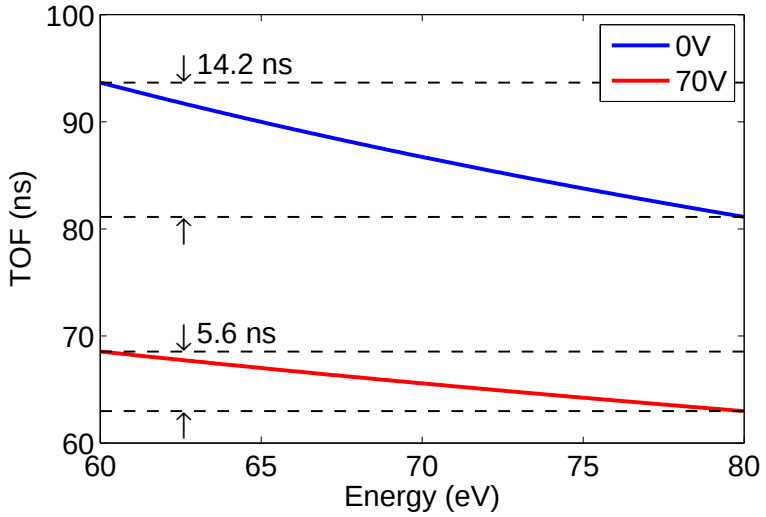


Figure 5.14: The time of flight for electrons as a function of their initial kinetic energy for two different voltages applied to the electrostatic lens system $V = 0\,\mathrm{V}$ and $V = 70\,\mathrm{V}$.

I have done simulations of the energy resolution, acceptance angle and energy calibration of our TOF with a commercially available software (SIMION®, SIS Inc.) for different voltages. All of the experimental data shown in this chapter was taken with an applied voltages of $V = 0, 30$ or $70\,\mathrm{V}$, chosen mainly depending on the electron count-rate and stability of the CEP lock. The advantage of using a non-zero applied voltage is the increase of the full acceptance angle from 4.6° to 7.6° (5.8°) for $V = 70\,\mathrm{V}$ ($V = 30\,\mathrm{V}$). This corresponds to increasing the solid angle from $2\pi(1 - \cos(4.6°)) = 20 \times 10^{-3}$ to 55×10^{-3} (32×10^{-3}) equivalent to an increase of electrons at the detector by 2.7 (1.6) times.

This comes at the expense of losing energy resolution. Due to the acceleration of the electrons in the applied electric field, the time of flight is decreased and compressed. This is shown in Figure 5.14, where I have plotted

the time of flight for $V = 0\,\mathrm{V}$ and $V = 70\,\mathrm{V}$.

One can see when comparing electrons with an initial kinetic energy of 60 and 80 eV that they show a difference of time of flight of 14.2 ns when no voltage is applied and 5.6 ns when 70 V is applied to the electrostatic lens system. Due to the finite resolution of the TDC card (100 ps), this leads to a better signal to noise as more electrons per time bin are recorded. But, as mentioned above, it also decreases the energy resolution. Simion calculations show, that the resolution for 70 eV electrons decreases from $\Delta E/E(0\,\mathrm{V}) = 0.4\%$ to $\Delta E/E(70\,\mathrm{V}) = 1.1\%$, all of which are sufficient for a reliable attosecond pulse retrieval [149].

5.2.2.1 TOF calibration

In order to calibrate the TOF spectrometer the length of the path from the interaction region to the MCP has to be known as well as the birth time of the electrons, t_0. In our setup the start signal for the TDC card is derived from a photodiode that monitors the CPA laser. To get the absolute time zero XUV photons scattered off the needle target are used. These travel at the speed of light and are therefore about two orders of magnitude faster than electrons with a kinetic energy of $\sim 100\,\mathrm{eV}$. The photon peak is therefore a distinct peak before the electron arrival time and can, after adding the flight time of the photons, be used as t_0.

The length of the TOF is calibrated, by acquiring an ATI spectrum with a long pulse. A long pulse ensures, that the ATI peaks are well defined [90]. We by-passed the hollow-fibre setup and used the 30 fs laser beam to generate ATI peaks from argon. A spectral measurement of the laser beam defines the central laser wavelength and therefore the energy spacing of the ATI peaks. The length of the TOF is then chosen such that the calculated energy spacing

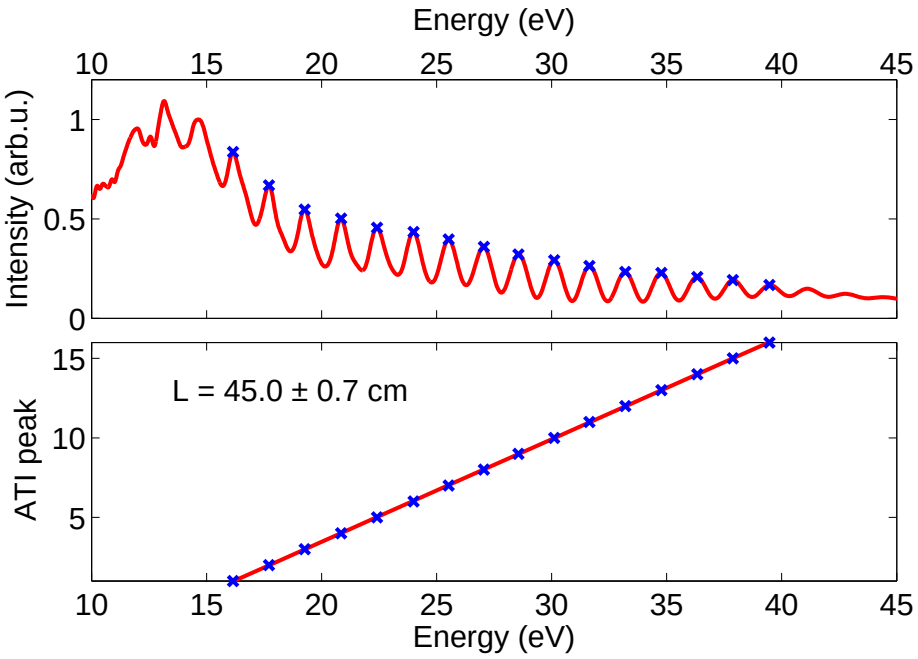


Figure 5.15: TOF length calibration. Top: ATI spectrum from a 30 fs pulse centred around $\lambda = 797.8$ nm. Bottom: Linear fit to the energy separation of the ATI peaks. The energy spacing is $\Delta E = 1.55 \pm 0.02$ eV corresponding to central wavelength of the driving field, $\lambda = 797.8$ nm.

of the ATI peaks equals photon energy corresponding to the centre of the laser spectrum. The ATI spectrum and a linear fit of the peak number as a function of the energy is shown in Figure 5.15.

When the length of the TOF is known, the spectrometer can be calibrated for different voltages applied to the electrostatic lens system. This is done, as shown in Figure 5.14, by running Simion calculations for the different voltages, which gives a mapping for the time of flight as a function of energy.

The spectral response of the TOF over a bandwidth of (60-80) eV was checked for $V = 30$ V and $V = 70$ V and was found to be flat with less than 1% difference over the whole bandwidth. Note that the XUV photo-

ionisation cross-section in neon for that bandwidth varies by more than 1% ($5 \pm 0.2\,\mathrm{Mb}$) and the measured spectra are not corrected for that [150].

5.3 Attosecond Streaking

In this section I will show the full characterisation of a single attosecond pulse (SAP). I will first describe a method to optimise the contrast of the SAP by scanning the CEP [141]. Then the streaking measurement of a single attosecond pulse using the amplitude gating technique [3, 5, 110] is presented and the FROG-CRAB retrieval algorithm [73] is discussed briefly.

5.3.1 Pulse Contrast Optimisation

The generation of a single attosecond pulse (SAP), using the amplitude gating technique [3, 5, 110] is dependent on the CEP of the driving laser field as discussed in subsection 2.2.3. The pulse contrast C_{SAP}, defined as the ratio of the main pulse intensity and the satellite pulse(s) intensity, can be measured by obtaining the photoelectron energy as a function of the CEP of the driving field [141]. The key idea of the method is the different momentum kick the main and the satellite pulse will receive from the electric field. The momentum kick is proportional to the vector potential of the streaking field [5]. Since the attosecond pulses are generated every half-cycle, they will experience a momentum kick in opposite directions. This is illustrated in Figure 5.16.

In our setup shown, as is shown in Figure 5.9, this measurement is done by closing the aperture at the TOF chamber entrance such that only the inner part of the two-part mirror is illuminated. The two-part zirconium filter is taken out of the beam path so that both the IR and the XUV fall on

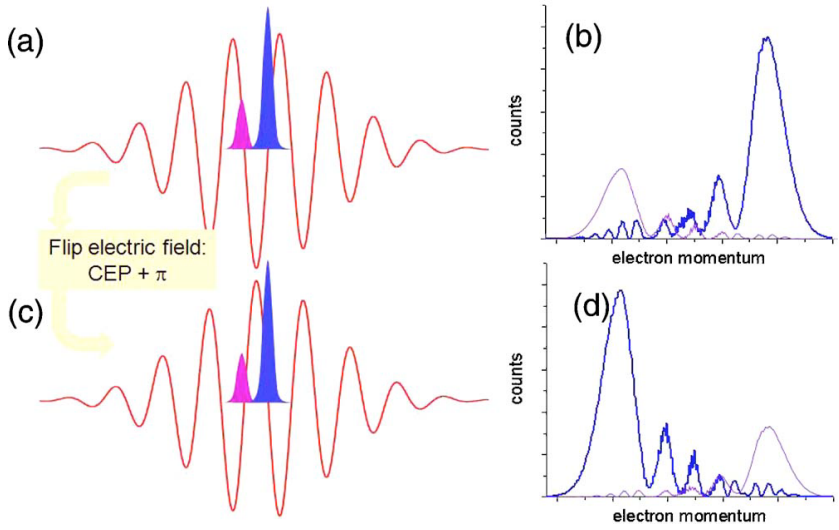


Figure 5.16: Illustration of the pulse contrast measurement. (a) Attosecond pulse and a small satellite are generated with a $-\cos$-pulse. (b): The photoelectrons of the main pulse receive a positive momentum kick, while the electrons from the satellite receive a negative momentum kick. (c) When changing the CEP by π, this situation is reversed, clearly shown in the electron spectrum (d). Taken from [141]

the inner part of the mirror. The electron spectrum at the focus position is recorded with the time-of-flight electron spectrometer (TOF) as the CEP is varied.

A streaking CEP-scan is shown in Figure 5.17. The low energy electrons are obscured by the low signal to noise ratio as they arrive over a larger time-span and therefore there are less electrons per time-bin. A pulse contrast measurement can still be done by only looking at the higher energy electrons, i.e. the ones that get a positive momentum kick.

The integrated streaked electron signal is defined as:

$$I(\phi) = \int_{E>E_0}^{\infty} E_{e^-}(\phi) \mathrm{d}E, \tag{5.4}$$

where ϕ is the CEP, E_0 the maximum unstreaked photoelectron energy and

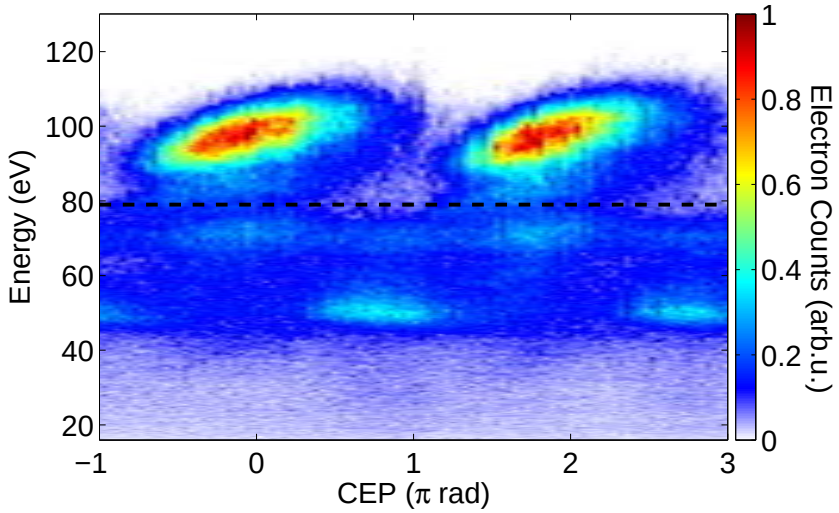


Figure 5.17: Experimental streaking CEP-scan. The lower energy electrons are obscured by the low signal to noise ratio. The electron counts are given in arbitrary units due to the rescaling factor when converting from time-of-flight to energy. The dotted line indicates the energy separation used for the pulse contrast measurement. Refer to text for more detail.

$E_{e^-}(\phi)$ the electron spectrum at a given CEP. Calculating the integrated streaked electron signal for a given CEP, $I(\text{CEP})$, and for a CEP shifted by π, $I(\text{CEP}+\pi)$, the contrast, C_{SAP}, is then given by dividing the larger integral by the smaller one [141]. The pulse contrast calculated for the streaking CEP-scan from Figure 5.17 is shown in Figure 5.18. The CEP-scan was re-sampled onto a CEP axis with an equidistant step-size of $0.04/\pi$ rad, close to the step-size of the measurement ($\sim 0.04/\pi$ rad), to calculate $I(\text{CEP})$ and $I(\text{CEP}+\pi)$. The maximum pulse contrast measured was $C_{\text{SAP}} = 5 \pm 0.2$, which is about twice as high as the pulse contrast measured by Pfeifer *et al.* [141]. This is owing to the shorter pulse duration used in our setup compared to the 7 fs pulse used by Pfeifer. A shorter pulse duration increases the the pulse contrast due to the larger difference of the IR-intensity of the main peak with

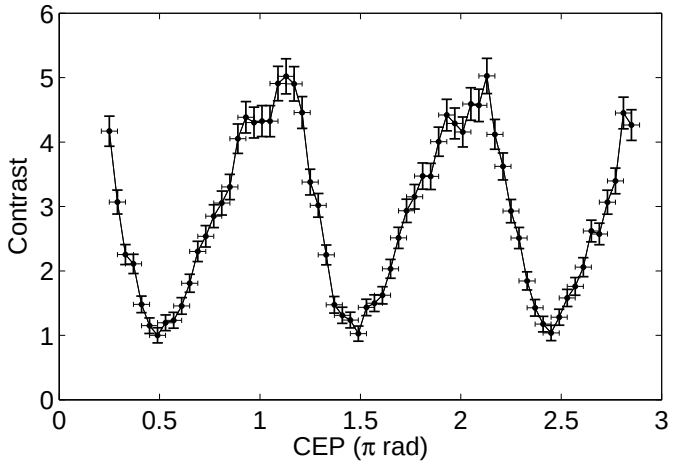


Figure 5.18: Attosecond pulse contrast analysis from the streaking CEP-scan from Figure 5.17. The maximum pulse contrast is 5.0 ± 0.2 at relative CEP values of $\phi = -1, 2$. The vertical error bars are from counting statistics and the horizontal errorbars are from CEP jitter and re-sampling errors (refer to text).

respect to the other peaks [141].

5.3.2 Attosecond Streaking

Our streaking measurement was done in the TOF chamber described earlier in this chapter with a similar experimental setup to the one at the Max Planck Institute in Garching [5, 139]. For the measurement, the CEP was set to the value determined with a streaking CEP-scan as discussed in the previous section. An unstreaked photolectron spectrum from neon gas, shown in Figure 5.19, was taken with the zirconium filter blocking the inner part of the IR and the controllable aperture at the entrance closed to block the outer part of the IR beam. The electron count in the energy region from (60-90) eV was around 500 counts/second, equivalent to one electron every

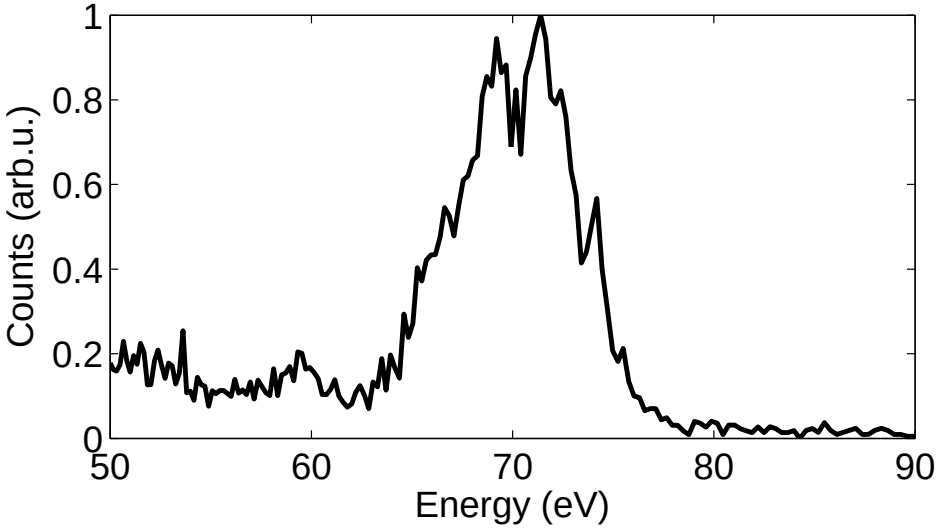


Figure 5.19: Unstreaked photoelectron spectrum from neon gas ionised with the XUV beam after the two-part mirror.

other shot. The spectrum of the ionising XUV beam is shown in Figure 5.7.

The electrons are centred around an energy of $E_{\text{e}^-} = 71\,\text{eV}$ with a FWHM of $\Delta E_{\text{e}^-} = 8\,\text{eV}$. The photon energy can be found by adding the ionisation potential of neon, $I_\text{p} = 21.56\,\text{eV}$, and leads to $E_\text{XUV} = 92\,\text{eV}$, which corresponds to maximum reflection as shown in Figure 5.10. The transform limited temporal duration supported by the photon spectrum is $\Delta t_\text{FTL} = 248\,\text{as}$.

For the XUV-IR delay scan, the aperture was slightly opened to set the IR streaking intensity to $\sim 1 \times 10^{12}\,\text{W/cm}^2$. An electron spectrum was recorded while the delay between the XUV and the IR-field was scanned. The delay step-size was set to 0.1 fs, equivalent to moving the inner part of the two-part mirror by 15 nm.

The raw streaking spectrogram is shown in Figure 5.20, where the only post-processing done was the energy conversion. The electron spectra at each delay point were averaged over 30 000 laser shots and a voltage of $V =$

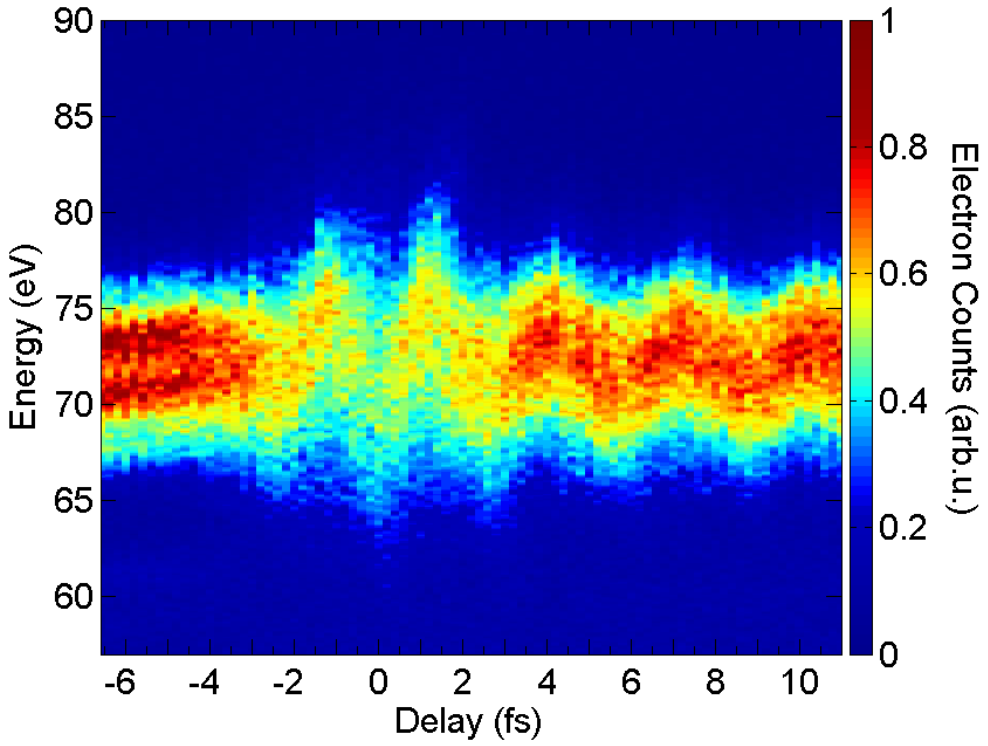


Figure 5.20: Experimentally obtained streaking spectrogram from our few-cycle laser pulse. The photoelectrons are generated by single photon XUV ionisation in neon. The delay step-size was set to 100 as.

30 V was applied to the electrostatic lens system leading to a count-rate of $\sim$ 500 Hz. The measurement of the whole spectrogram takes approximately one hour.

The characterisation of the XUV pulses was done using the FROG-CRAB technique [73] based on the FROG characterisation of ultrashort pulses [75] as discussed in subsubsection 2.2.3.2. The streaking spectrogram can be

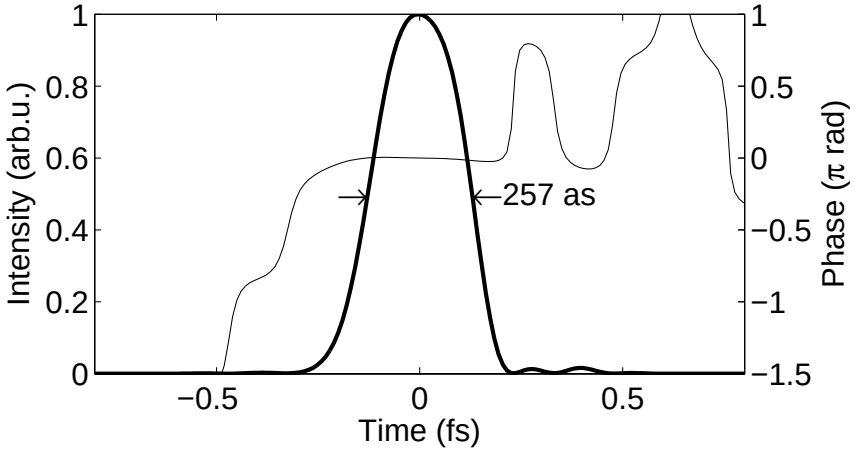


Figure 5.21: Retrieved temporal profile (thick line) and phase (thin line) of the attosecond pulse. The FWHM pulse duration is 257 as, only slightly longer than the Fourier transform limit, which is 248 as for the spectrum shown in Figure 5.19.

written as [118]:

$$S(\mathbf{p},\tau) = \left| \int_{-\infty}^{\infty} \mathrm{d}t \; \exp(i\phi(t)) \; \mathbf{d_p} \, \mathbf{E}_{\mathrm{XUV}}(t-\tau) \exp\left[i(W+I_\mathrm{p})t\right] \right|^2 , \tag{5.5}$$

$$\phi(t) = -\int_{t}^{\infty} \mathrm{d}t' \left(\mathbf{p}\cdot\mathbf{A}(t') + \mathbf{A}^2(t')/2\right), \tag{5.6}$$

where $W = \mathbf{p}\cdot\mathbf{A}(t) + \mathbf{A}^2(t)/2$ is the instantaneous energy and $\mathbf{A}(t)$ the vector potential, related to the electric field by $\mathbf{E}_\mathrm{L}(t) = \partial\mathbf{A}/\partial t$.

As mentioned earlier (subsubsection 2.2.3.2), a FROG-CRAB retrieval algorithm based on the generalised projection algorithm [151] can be used to fully characterise the XUV field, where the XUV field, $\mathbf{E}_{\mathrm{XUV}}$, is gated by $G(t) = \mathbf{d_p}\exp[i\phi(t)]$ [73].

The results of the FROG-CRAB retrieval are shown in Figure 5.21 and Figure 5.22. A single attosecond pulse with a temporal width at the half maximum of $\Delta t_{\mathrm{XUV}} = 257\,\mathrm{as}$ was retrieved, only slightly longer than the Fourier transform limit, which is $\Delta t_{\mathrm{FTL}} = 248\,\mathrm{as}$ for the spectrum shown in

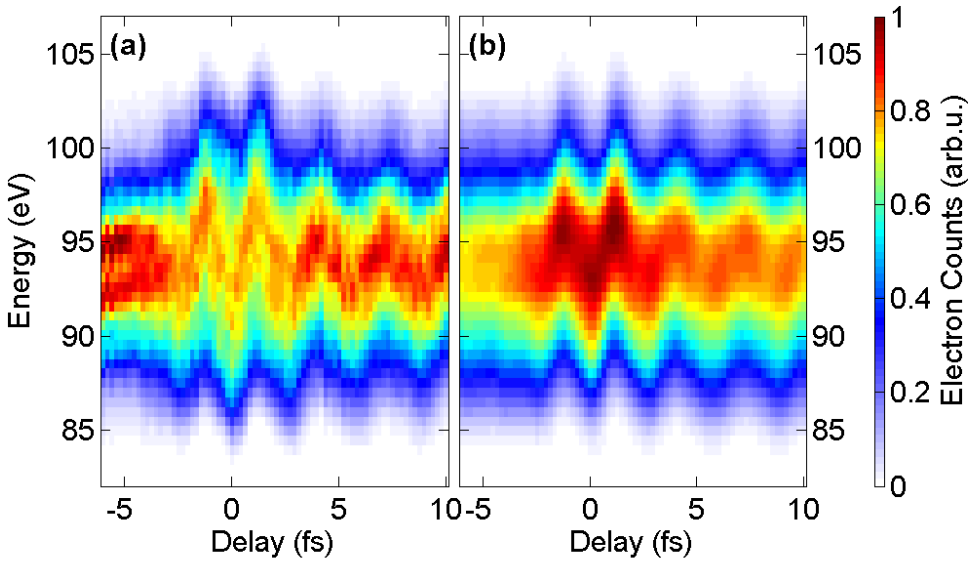


Figure 5.22: FROG-CRAB retrieval of the attosecond pulse. (a) Measured streaking spectrogram. (b) Retrieved spectrogram. The frog error from the retrieval is less than 5%. The retrieved temporal structure is shown in Figure 5.21 and shows duration of $\Delta t_{\mathrm{XUV}} = 257\,\mathrm{as}$.

Figure 5.19, mainly limited by the MoSi bandwidth. The FROG error is less than 5% (see also Equation 4.1). This error does not correspond to an error of the retrieved temporal duration, but is only an indication how well the algorithm converges. There has been one publication on how to retrieve an error from a FROG retrieval [152], but this method is not well established and and has hardly been used in the ultrafast community. Therefore no error for the temporal duration is given here.

For the retrieval, the trace was background corrected and Fourier filtered. The background, predominantly from low energy ATI photoelectrons, was subtracted by cropping the electron spectrum at each delay around the centre electron energy with a variable width. Each delay was then Fourier filtered to smooth the trace. Figure 5.23 shows the resulting electron spectrum for

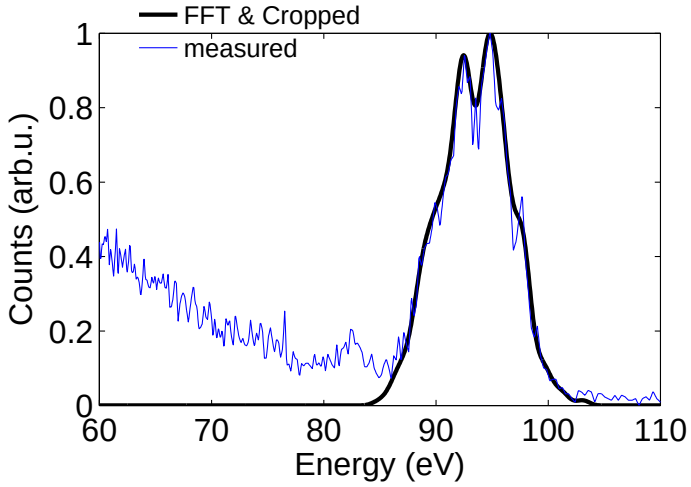


Figure 5.23: Fourier filtering and background correction of the electron spectra. The measured spectrum with the ATI background emergin at the low energy end (blue line) and the cropped and Fourier filtered spectrum used for the reconstruction (black line).

one delay. For the FROG algorithm, the trace was re-sampled onto a square 78×78 grid. The ionisation potential of neon ($I_\mathrm{p} = 21.56\,\mathrm{eV}$) was also added to yield the photon energies.

5.4 Conclusion

In this chapter I have presented the first measurement of a single attosecond pulse in the UK. I briefly described the few-cycle laser pulses used for high harmonic generation. The experimental apparatus used to generate and characterise the high harmonics has been described. Two independent estimates for the pulse duration have been presented by comparing the cut-off of the high harmonics with the cut-off for a pulse with the CEP shifted by π and the cut-off from the lower intensity half-cycle cutoff.

In the next section, the time of flight electron spectrometer was described

as well as the the spectral filtering used to generate single attosecond pulses. This was achieved by a zirconium filter and a multilayer MoSi-mirror that lead to a continuous photon spectrum centred around 92 eV with a width of ~ 8 eV.

In the final section I presented a method to characterise the pulse contrast with a streaking CEP-scan. This was used to set the CEP of the driving laser in order to obtain a single attosecond pulse. A streaking spectrogram was recorded and analysed showing a single attosecond pulse with a duration of $\Delta t_{\mathrm{XUV}} = 257$ as, which is close to the Fourier limit of $\Delta t_{\mathrm{FTL}} = 248$ as.

Chapter 6

Multi-Colour HHG

In this chapter I will describe high harmonic generation in an orthogonally polarised two-colour field using a mid-IR laser (1300 nm). I will first give a brief introduction to multi-colour HHG and the challenges of using longer wavelength drive lasers. I will then describe the two-colour setup used for our experiment and discuss the experimental results. To investigate the underlying physics, theoretical calculations using a SFA and a quantum orbit (QO) model were performed and the main results are discussed here.

6.1 Brief Introduction to Two-Colour HHG and Cut-off Extension

In this section I will give a brief introduction to high harmonic generation with two-colour fields, mainly focusing on orthogonally polarised ω+2ω-fields.

I will also shortly describe the use of longer wavelengths to extend the cut-off energy of the high harmonics.

6.1.1 Two-colour HHG

The first multi-colour HHG scheme employed used a two-colour field from a glass-based laser (1053 nm) and its second harmonic (526 nm) [153]. In contrast to single-field HHG, not only odd but also even harmonics of the stron ω-field (1053 nm) were produced. This comes as result of symmetry breaking with respect to the single-colour field. The field does not repeat itself every half-cycle but only every full-cycle with the second harmonic present. In the photon picture, this can be explained by sum or difference frequency mixing. An even harmonic occurs, when $2n$ fundamental photons and one second harmonic photon are absorbed, which is still an allowed dipole transition [153].

This has immediate implications in the generation of attosecond pulse-trains (APT). Instead of generating an attosecond pulse every half-cycle, the symmetry breaking reduces this periodicity by a factor of two [154]. It has also been shown, that by varying the phase between the two fields, the spectral properties of the attosecond pulse train can be controlled [155]. In addition to the spectral properties, varying the phase between the two-colour fields can also temporally shape APTs. Zheng *et.al.* have used a two-colour scheme to compensate the intrinsic negative chirp arising from the energy to time mapping in HHG [156].

The use of two-colour fields together with ellipticity gating techniques [112], referred to as double-optical gating (DOG), can also be used to generate single attosecond pulses (SAPs) from multi-cycle fields [113, 122, 142, 143]. Here the second-harmonic field alters the combined field in such a way that ionization from the leading edge of the pulse is limited. Therefore longer pulses can be used for SAP generation before ionization depletion effects occur [113].

Two-colour fields have also been used to gain new insights into atomic

and molecular imaging by exploiting the different return angle of the classical electron trajectories in such a setup [157, 158].

Using a weak orthogonally polarised second harmonic field in high harmonic generation has been shown to be a simple way to enhance the harmonic flux [12, 159, 160]. Kim *et al.* report an enhancement of two orders of magnitude in the harmonic yield when using a two-colour (800 and 400 nm) orthogonally polarised field.

The enhancement is explained by the formation of a quasilinear field when the relative phase between the fields is set to $\phi = \pi/2$ [12]. This is in contradiction to the results presented in this chapter, where the theoretical calculations show that the highest yield is obtained, when $\phi = 0$ [13].

6.1.2 Extension of the Cut-Off Energy

It is of interest to extend the cut-off of high harmonics to be able to deliver HHG sources that reach photon energies that up to now are only generated in large synchrotrons. Generating high-energy photons ($\sim$keV) with a table top laser in conjunction with an HHG system will open up these sources to a broad scientific community. Higher energies can lead to shorter attosecond pulses [4, 161] as a result of the shorter wavelength. Additionally, the reduction of the wavelength [162] leads to higher resolution in orbital imaging [163].

One way of extending the cut-off is by using a longer driving wavelength (see Equations 2.53 and 2.59) [164]. Unfortunately, the use of longer wavelength also dramatically decreases the efficiency of the high harmonic process. A scaling of the efficiency with $\lambda^{-5.5\pm1}$ has been predicted theoretically [165–167]. Recent measurements have revealed an even worse scaling law of $\lambda^{-6.5\pm1}$ [168].

The decrease in efficiency is mainly attributed to the spreading of the continuum electron wave packet which reduces the overlap with the ground state. The excursion time of the electron scales linearly with the wavelength (see subsubsection 2.2.2.2), but the broadening leads to a recombination probability scaling with the third power of the excursion time [102].

One of the aims of the experiment described in this chapter was to show that high harmonics generated with a mid-infrared laser beam can be enhanced by combining it with a weak second harmonic and thereby counteract the unfavourable wavelength scaling.

6.2 Experimental Setup and Results

The experiment was done at the Central Laser Facility of the Rutherford Appleton Laboratory in Didcot, UK. We used the Artemis laser, which is a Ti:sapphire CPA system (Red Dragon, KMLabs Inc.) delivering 6 mJ pulses with a duration of 30 fs centred at 780 nm with a repetition rate of 1 kHz.

This laser was used to pump an optical parametric amplifier (OPA - HE TOPAS, Light Conversion). The pulse duration was detuned to 80 fs to maximise the output of the OPA system. The OPA produced 40 fs pulses centred at 1300 nm with an energy of 950 µJ. The pulse duration was determined by second harmonic intensity autocorrelation measurement.

High harmonic generation was achieved by focusing the beam with a 30 cm lens into a gas target. The gas was delivered by a continuous flow gas-jet, formed by expansion of 2 bar of gas through a 100 µm nozzle diameter. The position of the target with respect to the foci was set by maximising the harmonic signal from the fundamental field alone.

The second harmonic beam was generated in a 300 µm thick type I beta-

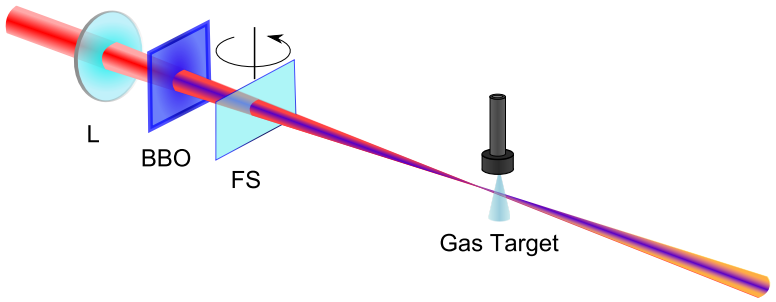


Figure 6.1: Two-colour high harmonic setup. The laser beam is focused with a 30 cm focal length lens (L) into the gas target. The nonlinear crystal (BBO) is positioned 2 cm after the lens. The phase between the two orthogonally polarised fields is altered with a rotatable thin fused-silica plate (FS) which is positioned ∼5 cm after the crystal. Adapted from [13]

barium borate crystal (BBO) with 20% conversion efficiency. It was positioned after the lens to eliminate temporal walk-off due to dispersion in the glass. A 270 µm thick fused-silica plate was mounted on a rotation stage and placed right after the crystal. This allowed us to continuously vary the phase between the IR and its second harmonic as the phase they acquire during the propagation in a dispersive medium is proportional to the wavelength-dependent refractive index. A schematic of the experimental setup can be seen in Figure 6.1.

The laser intensity at the interaction region was estimated to be 10^{14} W/cm^2 for the fundamental beam (1300 nm) by matching to the energy of the cut-off harmonics from the 1300 nm beam alone, which was recorded by tilting the nonlinear crystal away from the phase-matching condition. Assuming the same pulse duration and spot size for the second harmonic, the intensity of the 2ω-field is estimated to be 2×10^{13} W/cm^2.

The high harmonics were spectrally dispersed by a flat-field grating (1200 lines/mm) and collected by a micro channel plate (MCP) coupled to a phos-

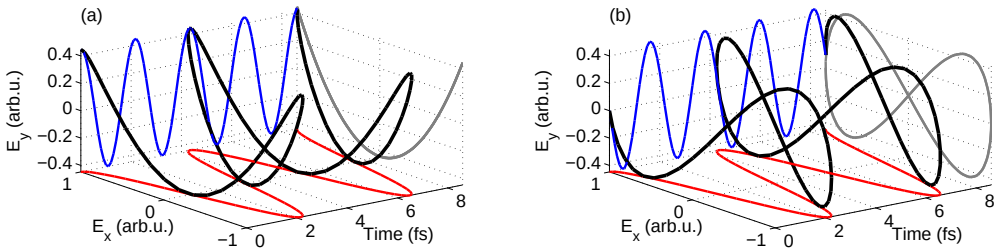


Figure 6.2: The ω- and 2ω-field and the resulting two-colour fields (black) for (a): $\phi = 0$ and (b): $\phi = \pi/2$ where the field strength of the 2ω-field is 0.4 times as strong as the fundamental field.

phor screen. The images on the back of the phosphor screen were recorded by a CCD camera. Each image was integrated for 20 ms (20 shots) and 200 of these images were averaged for each spectrum.

The two-colour field can be written as [13]:

$$\mathbf{E}(t) = \mathbf{e_x} f_\omega(t) cos(\omega t) + \mathbf{e_y} f_{2\omega}(t) cos(2\omega t + \phi), \tag{6.1}$$

where $f_\omega(t)$ and $f_{2\omega}(t)$ are envelope functions and ϕ is the phase difference between the two fields. The resulting fields for $\phi = 0$ and $\phi = \pi/2$ are shown in Figure 6.2 to illustrate the difference in shape of the resulting electric field and therefore the different electric fields the electron experiences in the continuum.

The high harmonics generated by the two-colour field in argon are shown in Figure 6.3. We observed an enhancement of the harmonic yield in the orthogonally polarised two-colour field of more than one order of magnitude with respect to the monochromatic field. Kim *et al.* [12] reported an enhancement of two orders of magnitude in their experiment, but a direct comparison cannot be made due to the different experimental regimes. They used a 820 nm - 410 nm-field with a duration 27 fs pulse in a different focusing

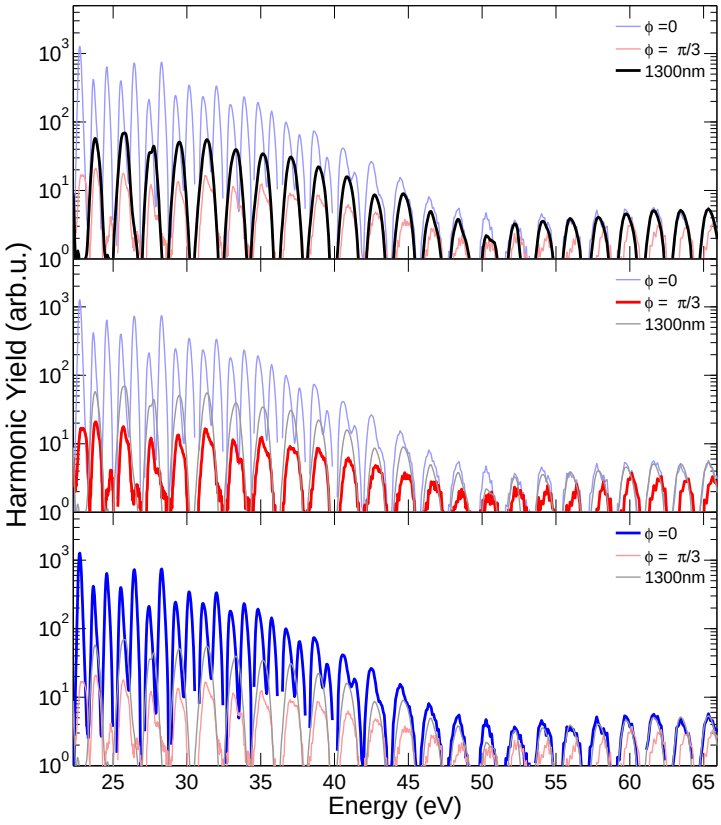


Figure 6.3: Experimental harmonic spectra generated with an orthogonally polarised two-colour field. Top: The fundamental alone (top). Middle: ω+2ω-field with the minimum harmonic yield. Bottom: ω+2ω-field with the maximum harmonic yield. (For better comparison, the other spectra are shown with a thin line in each plot.)

geometry.

The harmonic signal scanned over the delay between the two fields is shown in Figure 6.4. The modulation of the signal with respect to ϕ shows a π-periodicity, where 2π corresponds to the full-cycle of the second harmonic field. This shows, that the modulation is due to the combination of the fundamental with its second harmonic. A modulation depth of up to two

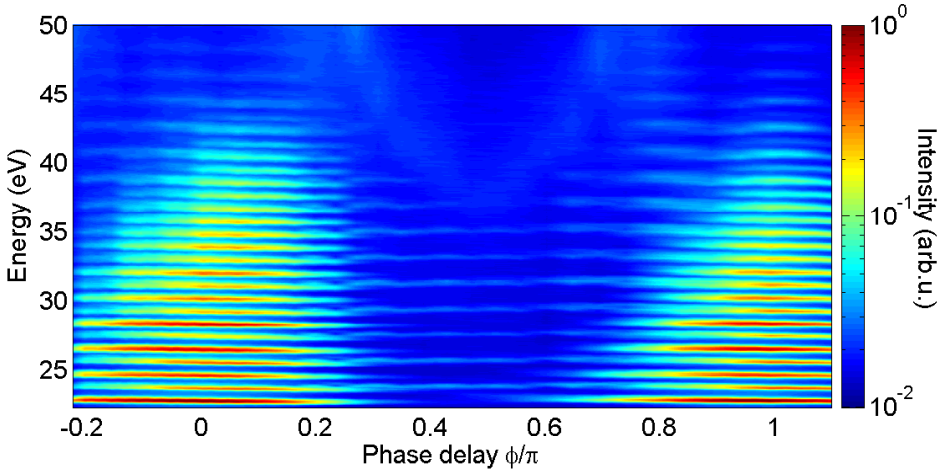


Figure 6.4: High harmonic yield as a function of the phase delay between the two-colour fields on a logarithmic colour scale.

orders of magnitude is observed. As was observed in earlier experiments [12, 160] the even harmonics (with respect to the fundamental field) are brighter than the odd harmonics in the case of orthogonally polarised fields and they show the deepest modulation.

6.3 Theoretical Description

To clarify the underlying mechanisms involved in in the modulation, we have developed a quantum orbit model (QO) [169] and checked its consistency with a strong-field approximation model (SFA) [102]. The use of a mid-IR wavelength ensured that we are in a regime where the SFA is valid and where multi-photon effects are negligible. Since we are interested in the physics behind the modulation, it is advantageous to use the QO model rather than solve the time-dependent Schrödinger equation here, because it is physically more transparent.

For the quantum orbit approach, we have to solve the system of equations

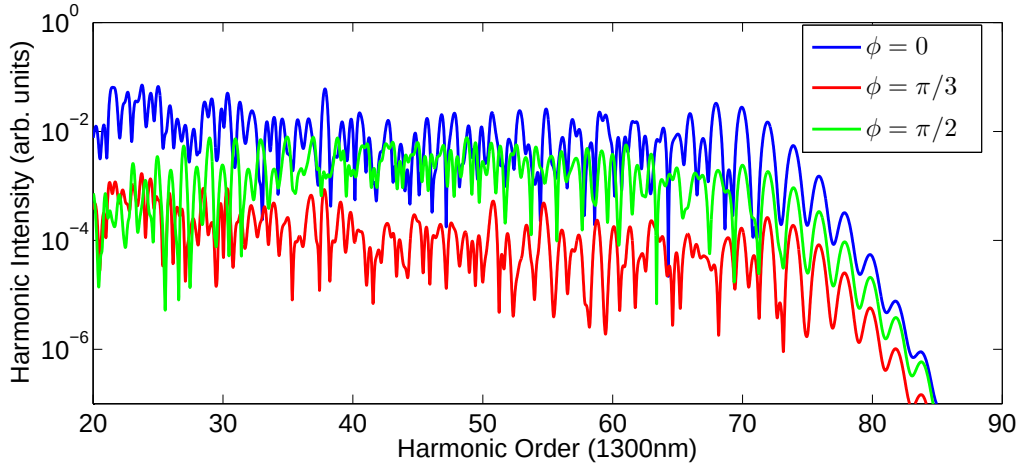


Figure 6.5: Comparison of two-colour harmonic spectra calculated with SFA for different phases between the fields for a driving intensity of $1.5 \times 10^{14}\,\mathrm{Wcm}^{-2}$. [13]

that render the action of the system, $S(\mathbf{p}, t, t')$, stationary with respect to $\mathbf{p}$, t and t'. Here, $\mathbf{p}$ is the birth momentum, t' the ionisation and t the recollision time. The time-dependent dipole moment can than be approximated, for a zero-range potential, to be:

$$d(t) = \sum_i C_i(\omega, t_i, t_i')\, e^{-iS(\mathbf{p},t,t')}, \tag{6.2}$$

where i runs over the ionisation events, in this case one short trajectory per half-cycle of the fundamental. By doing so, the dipole moment is split into two parts. A slowly evolving part, $C_i(\omega, t_i, t_i')$, describing wave-packet spreading and the recombination dipole-matrix element and $e^{-iS(\mathbf{p},t,t')}$ a fast oscillating exponential.

Both, the SFA and the QO calculations reproduce the π-periodicity. The modulation depth of the signal predicted from the calculations is two orders of magnitude and therefore agree well with the experimental modulation (two orders of magnitude between 22-30 eV and 1-1.5 orders of magnitude between

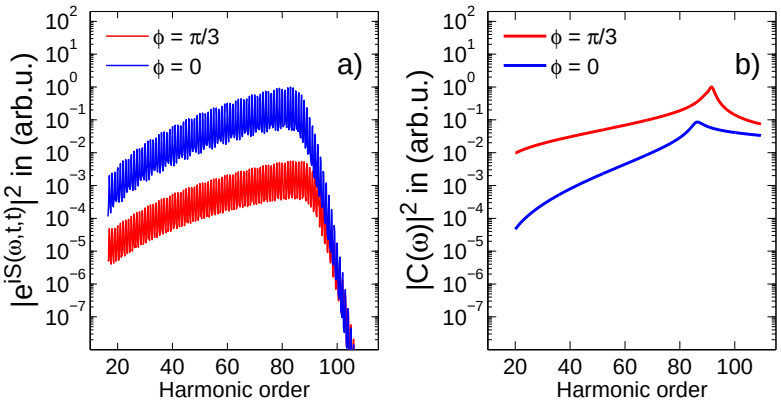


Figure 6.6: Quantum orbit calculation for high harmonic yield in an orthogonally-polarised two-colour field. (a) Only the fast oscillating exponential and (b) only the slow term. [13]

30-45 eV). The maximal harmonic yield is found to be at $\phi = n\pi$, where $n = 0, \pm 1, \pm 2, \cdots$ with a lower yield for $\phi = \pi/2$ and the lowest signal at $\phi = \pi/3$.

In the quantum orbit calculations, the two terms in the summation of Equation 6.2 can be evaluated separately. The modulus squared of the oscillating exponential, plotted in Figure 6.6(a), shows a difference of several orders of magnitude for the two cases, $\phi = 0$ and $\phi = \pi/3$. This difference outweighs the larger wave-packet spreading of the $\phi = 0$ case, depicted in Figure 6.6(b). This shows, that the dominant term, contributing to the shape of the spectrum is determined by the difference in the action of the two cases and is not due to wave-packet spreading. In other words, the modulation is a result of the two-dimensional steering of the electron in the two-colour field. The transverse momentum component (in the 2ω-direction) at the time of recollision is low for $\phi = 0$ and higher for $\phi = \pi/3$. This leads to a higher probability for high harmonic emission in the former case and prevents recollision in the latter case.

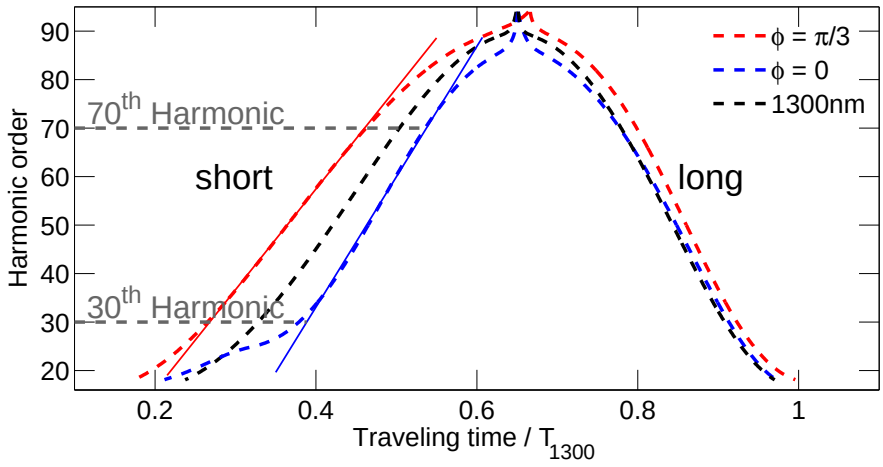


Figure 6.7: Harmonics order as a function of travelling time for $\phi = 0$ (blue), $\phi = \pi/3$ and for the single colour case (black dashed). [13]

Additional classical calculations have been performed to compare the time the electron spends in the continuum. As can be seen in Figure 6.7, the short trajectory electrons travelling in the orthogonally polarized field with a relative phase of $\phi = \pi/3$ spend less time in the continuum than in the $\phi = 0$ and single colour case. This is consistent with the wave-packet spreading discussed in the previous paragraph. It can also be seen that the atto-chirp, i.e. the energy to time mapping of the harmonic emission, for these trajectories can be altered with the phase. This can be used to alter the pulse duration of attosecond pulses [156].

6.4 Conclusion

In conclusion we have generated high harmonics in an orthogonally polarised two-colour field using a mid IR field (1300 nm) and its second harmonic (650 nm) We have observed an enhancement of more than one order of magnitude in comparison with the single colour case. This is very useful method

for efficiently generating high harmonics with mid-infrared driving lasers and overcoming the disadvantageous wavelength scaling of the high harmonic yield. It is straightforward to implement and does not significantly add to the complexity of high-harmonic experiments.

We also show a strong dependence on the relative phase of the two-fields with a modulation depth of two-orders of magnitude. The maximum yield is observed for $\phi = n\pi$, where $n = 0, \pm 1, \cdots$. This is reproduced with our SFA and quantum orbit calculations. By separating the contributions to harmonic spectra in the quantum orbit approach, we showed that the dominant contribution comes from the effect of the field history upon the action term and therefore from the steering of the trajectory in the continuum. In addition, we show, that by varying the phase between the fundamental and second harmonic, the atto-chirp can be varied over a broad part of the spectrum.

Chapter 7

Summary and Conclusion

The work presented in this thesis describes the generation and application of a wave-form stabilised few-cycle laser source. This source was fully characterized in space and time and used to generate high harmonics and ultimately single attosecond pulses. The attosecond pulses have been measured and fully characterised with an atomic streaking camera.

In addition high harmonics have been generated in an ω-2ω-field with a mid-IR fundamental beam (1300 nm). This has shown to enhance the harmonic yield with respect to the single colour field.

In this conclusion I will review each experimental chapter to give the reader a brief summary of the main experimental work and an outlook to future developments.

7.1 Chapter 3 and 4: Generation and Characterisation of Few-cycle Laser Pulses

I have described a commercial CEP stabilised CPA laser system producing 30 fs pulses with an energy of 750 µJ centred at $\lambda = 800$ nm. The CEP can

be stabilised over several hours with a standard deviation of below 100 mrad. This pulse has been spectrally broadened in a hollow fibre setup to achieve spectra spanning a bandwidth from 550 to 950 nm, equivalent to a sub-4 fs Fourier transform limited duration.

These pulses have then been characterised using a FROG setup optimised for few-cycle pulse characterisation. In addition, a SEA-F-SPIDER has been used to spatially and temporally characterise the output of the hollow fibre, measuring a pulse duration of 3.5 fs, one of the shortest IR pules in the world.

An upgrade of the main laser is planned for the near future increasing the output energy and/or the repetition rate of the system. Increasing the energy output will require further development of the hollow fibre pulse compression setup. A different scheme, using a differentially pumped fibre with a larger input diameter and possibly a gas with a higher ionisation potential can allow for higher input and transmission energies. Recent experiments from our group in collaboration with Laboratoire d'Optique Appliqué (LOA) in Palaiseau, France, show that the use of differentially pumped fibre in conjunction with circularly polarised light is a promising route to increase the energy transmission of hollow fibres.

In conclusion, I have described a system that delivers phase-stabilised sub-4 fs optical pulses derived from a commercially available CPA laser system.

7.2 Chapter 5: Attosecond Streaking

In Chapter 5 I have described how phase-stabilised few-cycle laser pulses are used to generate harmonics from a single half-cycle with a continuous spectrum suitable for single attosecond pulse production around 92 eV.

I have shown a method to estimate the pulse duration of the driving laser

at the gas target, since a precise measurement at the target is not suitable.

The pulse contrast of the attosecond pulse has been measured by a streaking CEP scan and the single attosecond pulse was characterised from an atomic streaking camera measurement. The temporal profile was analysed with a FROG-CRAB algorithm and the pulse duration was measured to be $\Delta t_{\mathrm{XUV}} \approx 260\,\mathrm{as}$.

In the recent months, a new ultra high vacuum chamber was added to our beamline. This will allow us to use the single attosecond pulses to investigate ultrafast electron dynamics on surfaces.

7.3 Chapter 6: Multi-Colour HHG

In this chapter, I described the high harmonic generation from an orthogonally polarised two-colour field ($\lambda_0 = 1300\,\mathrm{nm}$ and $\lambda_2 = 650\,\mathrm{nm}$). An enhancement of one order of magnitude with respect to the single colour field has been shown for one particular relative phase between the two fields. A modulation of two orders of magnitude of the harmonic yield as a function of the phase between the two fields has been measured.

This was investigated further with a theoretical model based on a quantum orbit SFA model. This model predicted, that the highest (lowest) yield is for a relative phase of $\phi = 0$ ($\phi = \pi/3$). Using a quantum orbit model allowed us to separate the effects of wave packet spreading from the steering of the electron in the continuum, predicting that the enhancement is due to trajectory steering and not wave packet spreading.

A similar experiment, using $\lambda_0 = 800\,\mathrm{nm}$ has already been set up at Imperial College. First experiments show that an orthogonal two-colour field can be used to select either short or long trajectories. This has implications

on HHG spectroscopy as it permits one to compare HHG from two different emission times by merely changing the phase between a two-colour field. In attosecond pulse generation, this method can be used to change the emission time of an attosecond pulse with respect to the fundamental field.

Bibliography

[1] SCHOTT AG, "Optical glass - data sheets," Jan 2011.

[2] M. Ammosov, N. Delone, and V. Krainov, "Tunnel ionization of complex atoms and of atomic ions in an alternating electromagnetic field," *Sov.Phys. - JETP*, vol. 64, pp. 1191–1194, Dec. 1986.

[3] M. Hentschel, R. Kienberger, C. Spielmann, G. A. Reider, N. Milosevic, T. Brabec, P. Corkum, U. Heinzmann, M. Drescher, and F. Krausz, "Attosecond metrology," *Nature*, vol. 414, pp. 509–513, Nov. 2001.

[4] E. Goulielmakis, M. Schultze, M. Hofstetter, V. S. Yakovlev, J. Gagnon, M. Uiberacker, A. L. Aquila, E. M. Gullikson, D. T. Attwood, R. Kienberger, F. Krausz, and U. Kleineberg, "Single-Cycle nonlinear optics," *Science*, vol. 320, pp. 1614–1617, June 2008.

[5] R. Kienberger, E. Goulielmakis, M. Uiberacker, A. Baltuska, V. Yakovlev, F. Bammer, A. Scrinzi, T. Westerwalbesloh, U. Kleineberg, U. Heinzmann, M. Drescher, and F. Krausz, "Atomic transient recorder," *Nature*, vol. 427, pp. 817–821, Feb. 2004.

[6] M. Schultze, M. Fiess, N. Karpowicz, J. Gagnon, M. Korbman, M. Hofstetter, S. Neppl, A. L. Cavalieri, Y. Komninos, T. Mercouris, C. A. Nicolaides, R. Pazourek, S. Nagele, J. Feist, J. Burgdorfer, A. M. Azzeer, R. Ernstorfer, R. Kienberger, U. Kleineberg, E. Goulielmakis, F. Krausz, and V. S. Yakovlev, "Delay in photoemission," *Science*, vol. 328, pp. 1658–1662, June 2010.

[7] M. Ferray, A. L'Huillier, X. F. LI, L. A. Lompre, G. Mainfray, and C. Manus, "Multiple-harmonic conversion of 1064 nm radiation in rare gases," *Journal of Physics B: Atomic, Molecular and Optical Physics*, vol. 21, no. 3, p. L31, 1988.

[8] G. Farkas and C. Tóth, "Proposal for attosecond light pulse generation using laser induced multiple-harmonic conversion processes in rare gases," *Physics Letters A*, vol. 168, p. 447450, Sept. 1992.

[9] T. Witting, F. Frank, C. A. Arrell, W. A. Okell, J. P. Marangos, and J. W. G. Tisch, "Characterization of high-intensity sub-4-fs laser pulses using spatially encoded spectral shearing interferometry," *Optics Letters*, vol. 36, pp. 1680–1682, May 2011.

[10] K. J. Schafer, B. Yang, L. F. DiMauro, and K. C. Kulander, "Above threshold ionization beyond the high harmonic cutoff," *Physical Review Letters*, vol. 70, p. 1599, Mar. 1993.

[11] P. B. Corkum, "Plasma perspective on strong field multiphoton ionization," *Physical Review Letters*, vol. 71, no. 13, p. 1994, 1993.

[12] I. J. Kim, C. M. Kim, H. T. Kim, G. H. Lee, Y. S. Lee, J. Y. Park, D. J. Cho, and C. H. Nam, "Highly efficient High-Harmonic generation in an orthogonally polarized Two-Color laser field," *Physical Review Letters*, vol. 94, p. 243901, June 2005.

[13] L. Brugnera, F. Frank, D. J. Hoffmann, R. Torres, T. Siegel, J. G. Underwood, E. Springate, C. Froud, E. I. C. Turcu, J. W. G. Tisch, and J. P. Marangos, "Enhancement of high harmonics generated by field steering of electrons in a two-color orthogonally polarized laser field," *Optics Letters*, vol. 35, pp. 3994–3996, Dec. 2010.

[14] C. Rulliere, *Femtosecond Laser Pulses: Principles and Experiments*. Springer, 2nd ed., Oct. 1998.

[15] U. Morgner, F. X. Kärtner, S. H. Cho, Y. Chen, H. A. Haus, J. G. Fujimoto, E. P. Ippen, V. Scheuer, G. Angelow, and T. Tschudi, "Sub-two-cycle pulses from a Kerr-lens mode-locked Ti:sapphire laser," *Optics Letters*, vol. 24, pp. 411–413, Mar. 1999.

[16] F. J. McClung and R. W. Hellwarth, "Giant optical pulsations from ruby," *Journal of Applied Physics*, vol. 33, no. 3, p. 828, 1962.

[17] A. J. DeMaria, "Self mode-locking of lasers with saturable absorbers," *Applied Physics Letters*, vol. 8, no. 7, p. 174, 1966.

[18] P. F. Moulton, "Spectroscopic and laser characteristics of Ti:Al2O3," *Journal of the Optical Society of America B*, vol. 3, pp. 125–133, Jan. 1986.

[19] Y. Ishida, N. Sarukura, and H. Nakano, "Conference: Ultrafast phenomena vii," in *California*, OSA, 1990.

[20] D. E. Spence, P. N. Kean, and W. Sibbett, "60-fsec pulse generation from a self-mode-locked Ti:sapphire laser," *Optics Letters*, vol. 16, pp. 42–44, Jan. 1991.

[21] J. Degnan, "Optimization of passively q-switched lasers," *Quantum Electronics, IEEE Journal of*, vol. 31, no. 11, pp. 1890–1901, 1995.

[22] U. Keller, "Recent developments in compact ultrafast lasers," *Nature*, vol. 424, no. 6950, pp. 831–838, 2003.

[23] P. W. Milonni and J. H. Eberly, *Lasers*. Wiley-Interscience, 1 ed., Oct. 1988.

[24] A. E. Siegman, *Lasers*. University Science Books, Jan. 1986.

[25] H. Eklund, A. Roos, and S. T. Eng, "Rotation of laser beam polarization in acousto-optic devices," *Optical and Quantum Electronics*, vol. 7, no. 2, pp. 73–79, 1975.

[26] U. Keller, K. Weingarten, F. Kartner, D. Kopf, B. Braun, I. Jung, R. Fluck, C. Honninger, N. Matuschek, and J. A. der Au, "Semiconductor saturable absorber mirrors (SESAM's) for femtosecond to nanosecond pulse generation in solid-state lasers," *Selected Topics in Quantum Electronics, IEEE Journal of*, vol. 2, no. 3, pp. 435–453, 1996.

[27] F. Salin, J. Squier, and M. Pich?, "Mode locking of Ti:AI2O3 lasers and self-focusing: a gaussian approximation," *Optics Letters*, vol. 16, pp. 1674–1676, Nov. 1991.

[28] G. Cerullo, S. D. Silvestri, V. Magni, and L. Pallaro, "Resonators for Kerr-lens mode-locked femtosecond Ti:sapphire lasers," *Optics Letters*, vol. 19, pp. 807–809, June 1994.

[29] G. Cerullo, S. D. Silvestri, and V. Magni, "Self-starting Kerr-lens mode locking of a Ti:sapphire laser," *Optics Letters*, vol. 19, pp. 1040–1042, July 1994.

[30] H. Haus, J. Fujimoto, and E. Ippen, "Analytic theory of additive pulse and kerr lens mode locking," *Quantum Electronics, IEEE Journal of*, vol. 28, no. 10, pp. 2086–2096, 1992.

[31] J. Herrmann, "Theory of Kerr-lens mode locking: role of self-focusing and radially varying gain," *Journal of the Optical Society of America B*, vol. 11, pp. 498–512, Mar. 1994.

[32] R. W. Boyd, *Nonlinear Optics*. Academic Press, 3 ed., May 2008.

[33] P. A. Franken, A. E. Hill, C. W. Peters, and G. Weinreich, "Generation of optical harmonics," *Physical Review Letters*, vol. 7, no. 4, p. 118, 1961.

[34] I. Jovanovic, C. Brown, B. Wattellier, N. Nielsen, W. Molander, B. Stuart, D. Pennington, and C. P. J. Barty, "Precision short-pulse damage test station utilizing optical parametric chirped-pulse amplification," *Review of Scientific Instruments*, vol. 75, no. 12, p. 5193, 2004.

[35] H. Nakatsuka, D. Grischkowsky, and A. C. Balant, "Nonlinear Picosecond-Pulse propagation through optical fibers with positive group velocity dispersion," *Physical Review Letters*, vol. 47, no. 13, p. 910, 1981.

[36] W. J. Tomlinson, R. H. Stolen, and C. V. Shank, "Compression of optical pulses chirped by self-phase modulation in fibers," *Journal of the Optical Society of America B*, vol. 1, pp. 139–149, Apr. 1984.

[37] J. K. Ranka, R. S. Windeler, and A. J. Stentz, "Optical properties of high-delta air silica microstructure optical fibers," *Optics Letters*, vol. 25, pp. 796–798, June 2000.

[38] P. Russell, "Photonic crystal fibers," *Science*, vol. 299, no. 5605, p. 358362, 2003.

[39] J. Robinson, C. Haworth, H. Teng, R. Smith, J. Marangos, and J. Tisch, "The generation of intense, transform-limited laser pulses with tunable duration from 6 to 30 fs in a differentially pumped hollow fibre," *Applied Physics B: Lasers and Optics*, vol. 85, pp. 525–529, Dec. 2006.

[40] E. A. J. Marcatili and R. A. Schmeltzer, "Hollow metallic and dielectric waveguides for long distance optical transmission and lasers," *Bell System Technical Journal*, vol. 43, pp. 1783–1809, July 1964.

[41] M. Nisoli, S. D. Silvestri, and O. Svelto, "Generation of high energy 10 fs pulses by a new pulse compression technique," *Applied Physics Letters*, vol. 68, pp. 2793–2795, May 1996.

[42] A. Rundquist, C. G. Durfee, Z. Chang, C. Herne, S. Backus, M. M. Murnane, and H. C. Kapteyn, "Phase-Matched generation of coherent soft x-rays," *Science*, vol. 280, pp. 1412 –1415, May 1998.

[43] M. Miyagi, K. Harada, and S. Kawakami, "Wave propagation and attenuation in the general class of circular hollow waveguides with uniform curvature," *IEEE Transactions on Microwave Theory and Techniques*, vol. 32, pp. 513– 521, May 1984.

[44] D. R. Hall, E. K. Gorton, and R. M. Jenkins, "10µm propagation losses in hollow dielectric waveguides," *Journal of Applied Physics*, vol. 48, no. 3, p. 1212, 1977.

[45] T. Brabec, *Strong Field Laser Physics*. Springer, Oct. 2008.

[46] G. P. G. P. . Agrawal, *Nonlinear Fiber Optics*. Burlington, MA ; London: Academic Press, 2007. Pages: xvi, 529 p General Note: Previous ed.: 2001 Sound rec number: 9780123695161 90000 Edition: 4th ed Physical descrip: xvi, 529 p. : ill. : 24 cm General Note: Previous ed.: 2001 Bibliography note: Includes bibliographical references and index LC Subject heading: Fiber optics LC Subject heading: Nonlinear optics.

[47] M. Nisoli, S. Stagira, S. D. Silvestri, O. Svelto, S. Sartania, Z. Cheng, M. Lenzner, C. Spielmann, and F. Krausz, "A novel-high energy pulse compression system: generation of multigigawatt sub-5-fs pulses," *Applied Physics B: Lasers and Optics*, vol. 65, no. 2, p. 189196, 1997.

[48] E. Neumann, *Single Mode Fibers I: Fundamentals*. Springer-Verlag, Oct. 1988.

[49] M. Nisoli, S. Stagira, S. D. Silvestri, O. Svelto, S. Sartania, Z. Cheng, G. Tempea, C. Spielmann, and F. Krausz, "Toward a terawatt-scale sub-10-fs laser technology," *Selected Topics in Quantum Electronics, IEEE Journal of*, vol. 4, no. 2, pp. 414–420, 1998.

[50] D. Strickland and G. Mourou, "Compression of amplified chirped optical pulses," *Optics Communications*, vol. 56, pp. 219–221, Dec. 1985.

[51] R. Szipöcs, K. Ferencz, C. Spielmann, and F. Krausz, "Chirped multilayer coatings for broadband dispersion control in femtosecond lasers," *Optics Letters*, vol. 19, pp. 201–203, Feb. 1994.

[52] E. Treacy, "Optical pulse compression with diffraction gratings," *Quantum Electronics, IEEE Journal of*, vol. 5, no. 9, pp. 454–458, 1969.

[53] O. E. Martinez, "Grating and prism compressors in the case of finite beam size," *Journal of the Optical Society of America B*, vol. 3, pp. 929–934, July 1986.

[54] R. L. Fork, O. E. Martinez, and J. P. Gordon, "Negative dispersion using pairs of prisms," *Optics Letters*, vol. 9, pp. 150–152, May 1984.

[55] J. P. Gordon and R. L. Fork, "Optical resonator with negative dispersion," *Optics Letters*, vol. 9, no. 5, pp. 153–155, 1984.

[56] F. X. Kärtner, N. Matuschek, T. Schibli, U. Keller, H. A. Haus, C. Heine, R. Morf, V. Scheuer, M. Tilsch, and T. Tschudi, "Design and fabrication of double-chirped mirrors," *Optics Letters*, vol. 22, pp. 831–833, June 1997.

[57] S. T. Cundiff and J. Ye, "Colloquium: Femtosecond optical frequency combs," *Reviews of Modern Physics*, vol. 75, p. 325, Mar. 2003.

[58] L. Xu, C. Spielmann, A. Poppe, T. Brabec, F. Krausz, and T. W. H?nsch, "Route to phase control of ultrashort light pulses," *Optics Letters*, vol. 21, pp. 2008–2010, Dec. 1996.

[59] H. Telle, G. Steinmeyer, A. Dunlop, J. Stenger, D. Sutter, and U. Keller, "Carrier-envelope offset phase control: A novel concept for absolute optical frequency measurement and ultrashort pulse generation," *Applied Physics B: Lasers and Optics*, vol. 69, no. 4, pp. 327–332, 1999.

[60] J. K. Ranka, R. S. Windeler, and A. J. Stentz, "Visible continuum generation in air-silica microstructure optical fibers with anomalous dispersion at 800 nm," *Optics Letters*, vol. 25, pp. 25–27, Jan. 2000.

[61] J. M. Dudley, G. Genty, and S. Coen, "Supercontinuum generation in photonic crystal fiber," *Reviews of Modern Physics*, vol. 78, p. 1135, Oct. 2006.

[62] D. J. Jones, S. A. Diddams, J. K. Ranka, A. Stentz, R. S. Windeler, J. L. Hall, and S. T. Cundiff, "Carrier-Envelope phase control of femtosecond Mode-Locked lasers and direct optical frequency synthesis," *Science*, vol. 288, pp. 635 –639, Apr. 2000.

[63] A. Apolonski, A. Poppe, G. Tempea, C. Spielmann, T. Udem, R. Holzwarth, T. W. Hänsch, and F. Krausz, "Controlling the phase evolution of Few-Cycle light pulses," *Physical Review Letters*, vol. 85, p. 740, July 2000.

[64] G. G. Paulus, F. Grasbon, H. Walther, P. Villoresi, M. Nisoli, S. Stagira, E. Priori, and S. D. Silvestri, "Absolute-phase phenomena in photoionization with few-cycle laser pulses," *Nature*, vol. 414, pp. 182–184, Nov. 2001.

[65] G. G. Paulus, F. Lindner, H. Walther, A. Baltuscaronka, E. Goulielmakis, M. Lezius, and F. Krausz, "Measurement of the phase of Few-Cycle laser pulses," *Physical Review Letters*, vol. 91, p. 253004, Dec. 2003.

[66] T. Wittmann, B. Horvath, W. Helml, M. G. Schatzel, X. Gu, A. L. Cavalieri, G. G. Paulus, and R. Kienberger, "Single-shot carrier-envelope phase measurement of few-cycle laser pulses," *Nat Phys*, vol. 5, pp. 357–362, May 2009.

[67] A. Apolonski, P. Dombi, G. G. Paulus, M. Kakehata, R. Holzwarth, T. Udem, C. Lemell, K. Torizuka, J. Burgdörfer, T. W. Hänsch, and F. Krausz, "Observation of Light-Phase-Sensitive photoemission from a metal," *Physical Review Letters*, vol. 92, p. 073902, Feb. 2004.

[68] M. Kreß, T. Loffler, M. D. Thomson, R. Dorner, H. Gimpel, K. Zrost, T. Ergler, R. Moshammer, U. Morgner, J. Ullrich, and H. G. Roskos, "Determination of the carrier-envelope phase of few-cycle laser pulses with terahertz-emission spectroscopy," *Nat Phys*, vol. 2, pp. 327–331, May 2006.

[69] C. A. Haworth, L. E. Chipperfield, J. S. Robinson, P. L. Knight, J. P. Marangos, and J. W. G. Tisch, "Half-cycle cutoffs in harmonic spectra and robust carrier-envelope phase retrieval," *Nat Phys*, vol. 3, pp. 52–57, Jan. 2007.

[70] J. S. Robinson, *The generation and application of intense, few-cycle laser pulses.* PhD thesis, Imperial College London, London, July 2006.

[71] J. A. Armstrong, "Measuremente of picosecond laser pulse widths," *Applied Physics Letters*, vol. 10, no. 1, p. 16, 1967.

[72] K. W. DeLong, R. Trebino, and D. J. Kane, "Comparison of ultrashort-pulse frequency-resolved-optical-gating traces for three common beam geometries," *J. Opt. Soc. Am. B*, vol. 11, no. 9, p. 15951608, 1994.

[73] Y. Mairesse and F. Quéré, "Frequency-resolved optical gating for complete reconstruction of attosecond bursts," *Physical Review A*, vol. 71, p. 011401, Jan. 2005.

[74] D. Kane and R. Trebino, "Characterization of arbitrary femtosecond pulses using frequency-resolved optical gating," *Quantum Electronics, IEEE Journal of*, vol. 29, no. 2, pp. 571–579, 1993.

[75] R. Trebino and D. J. Kane, "Using phase retrieval to measure the intensity and phase of ultrashort pulses: frequency-resolved optical gating," *Journal of the Optical Society of America A*, vol. 10, pp. 1101–1111, May 1993.

[76] K. W. DeLong, R. Trebino, J. Hunter, and W. E. White, "Frequency-resolved optical gating with the use of second-harmonic generation," *Journal of the Optical Society of America B*, vol. 11, pp. 2206–2215, Nov. 1994.

[77] R. Trebino, *Frequency-Resolved Optical Gating: The Measurement of Ultrashort Laser Pulses.* Springer, 1 ed., Aug. 2002.

[78] A. Baltuska, M. S. Pshenichnikov, and D. A. Wiersma, "Amplitude and phase characterization of 4.5-fs pulses by frequency-resolved optical gating," *Optics Letters*, vol. 23, no. 18, pp. 1474–1476, 1998.

[79] A. Baltuska, M. Pshenichnikov, and D. Wiersma, "Second-harmonic generation frequency-resolved optical gating in the single-cycle regime," *Quantum Electronics, IEEE Journal of*, vol. 35, no. 4, pp. 459–478, 1999.

[80] C. Iaconis and I. Walmsley, "Spectral phase interferometry for direct electric-field reconstruction of ultrashort optical pulses," *Optics Letters*, vol. 23, pp. 792–794, May 1998.

[81] M. Takeda, H. Ina, and S. Kobayashi, "Fourier-transform method of fringe-pattern analysis for computer-based topography and interferometry," *Journal of the Optical Society of America*, vol. 72, pp. 156–160, Jan. 1982.

[82] W. Kornelis, J. Biegert, J. W. G. Tisch, M. Nisoli, G. Sansone, C. Vozzi, S. D. Silvestri, and U. Keller, "Single-shot kilohertz characterization of ultrashort pulses by spectral phase interferometry for direct electric-field reconstruction," *Optics Letters*, vol. 28, pp. 281–283, Feb. 2003.

[83] T. Witting, D. R. Austin, and I. A. Walmsley, "Improved ancilla preparation in spectral shearing interferometry for accurate ultrafast pulse characterization," *Optics Letters*, vol. 34, pp. 881–883, Apr. 2009.

[84] D. R. Austin, T. Witting, and I. A. Walmsley, "High precision self-referenced phase retrieval of complex pulses with multiple-shearing spectral interferometry," *Journal of the Optical Society of America B*, vol. 26, no. 9, pp. 1818–1830, 2009.

[85] L. V. Keldysh, "Ionizations in the field of a strong electromagnetic wave," *Sov.Phys. - JETP*, vol. 20, p. 1307–1314, 1965.

[86] M. Protopapas, C. H. Keitel, and P. L. Knight, "Atomic physics with super-high intensity lasers," *Reports on Progress in Physics*, vol. 60, no. 4, pp. 389–486, 1997.

[87] G. G. Paulus, W. Nicklich, H. Xu, P. Lambropoulos, and H. Walther, "Plateau in above threshold ionization spectra," *Physical Review Letters*, vol. 72, p. 2851, May 1994.

[88] G. G. Paulus, W. Becker, W. Nicklich, and H. Walther, "Rescattering effects in above-threshold ionization: a classical model," *Journal of Physics B: Atomic, Molecular and Optical Physics*, vol. 27, pp. L703–L708, Nov. 1994.

[89] P. Kruit, J. Kimman, H. G. Muller, and M. J. van der Wiel, "Electron spectra from multiphoton ionization of xenon at 1064, 532, and 355 nm," *Physical Review A*, vol. 28, p. 248, July 1983.

[90] F. Grasbon, G. G. Paulus, H. Walther, P. Villoresi, G. Sansone, S. Stagira, M. Nisoli, and S. D. Silvestri, "Above-Threshold ionization at the Few-Cycle limit," *Physical Review Letters*, vol. 91, p. 173003, Oct. 2003.

[91] G. L. Yudin and M. Y. Ivanov, "Nonadiabatic tunnel ionization: Looking inside a laser cycle," *Physical Review A*, vol. 64, p. 013409, June 2001.

[92] M. Y. Ivanov, M. Spanner, and O. Smirnova, "Anatomy of strong field ionization," *Journal of Modern Optics*, vol. 52, no. 2, pp. 165 – 184, 2005.

[93] Y. Liang, S. Augst, S. L. Chin, Y. Beaudoin, and M. Chaker, "High harmonic generation in atomic and diatomic molecular gases using intense picosecond laser pulses-a comparison," *Journal of Physics B: Atomic, Molecular and Optical Physics*, vol. 27, no. 20, p. 5119, 1994.

[94] D. J. Fraser, M. H. R. Hutchinson, J. P. Marangos, Y. L. Shao, J. W. G. Tisch, and M. Castillejo, "High harmonic generation in butane and butadiene," *Journal of Physics B: Atomic, Molecular and Optical Physics*, vol. 28, no. 23, p. L739, 1995.

[95] N. Hay, M. Castillejo, R. de Nalda, E. Springate, K. J. Mendham, and J. P. Marangos, "High-order harmonic generation in cyclic organic molecules," *Physical Review A*, vol. 61, p. 053810, Apr. 2000.

[96] C. Vozzi, F. Calegari, E. Benedetti, J. Caumes, G. Sansone, S. Stagira, M. Nisoli, R. Torres, E. Heesel, N. Kajumba, J. P. Marangos, C. Altucci, and R. Velotta, "Controlling Two-Center interference in molecular high harmonic generation," *Physical Review Letters*, vol. 95, p. 153902, Oct. 2005.

[97] T. D. Donnelly, T. Ditmire, K. Neuman, M. D. Perry, and R. W. Falcone, "High-Order harmonic generation in atom clusters," *Physical Review Letters*, vol. 76, p. 2472, Apr. 1996.

[98] J. W. G. Tisch, T. Ditmire, D. J. Fraser, N. Hay, M. B. Mason, E. Springate, J. P. Marangos, and M. H. R. Hutchinson, "Investigation of high-harmonic generation from xenon atom clusters," *Journal of Physics B: Atomic, Molecular and Optical Physics*, vol. 30, no. 20, p. L709, 1997.

[99] J. Reintjes, C. Y. She, R. C. Eckardt, N. E. Karangelen, R. A. Andrews, and R. C. Elton, "Seventh harmonic conversion of mode-locked laser pulses to 38.0 nm," *Applied Physics Letters*, vol. 30, no. 9, p. 480, 1977.

[100] M. Grozeva, D. Metchkov, V. Mitev, L. Pavlov, and K. Stamenov, "Direct ninth harmonic conversion of picosecond laser pulses," *Optics Communications*, vol. 23, pp. 77–79, Oct. 1977.

[101] A. McPherson, G. Gibson, H. Jara, U. Johann, T. S. Luk, I. A. McIntyre, K. Boyer, and C. K. Rhodes, "Studies of multiphoton production of vacuum-ultraviolet radiation in the rare gases," *Journal of the Optical Society of America B*, vol. 4, pp. 595–601, Apr. 1987.

[102] M. Lewenstein, P. Balcou, M. Y. Ivanov, A. L'Huillier, and P. B. Corkum, "Theory of high-harmonic generation by low-frequency laser fields," *Physical Review A*, vol. 49, p. 2117, Mar. 1994.

[103] E. Skopalová, *The interaction of intense few-cycle laser pulses with nanoscale targets*. PhD thesis, Imperial College London, Mar. 2011.

[104] R. Murray, *Tunnel Ionization in Strong Fields in atoms and molecules and its applications*. PhD, University of Waterloo, 2011.

[105] P. Balcou, P. Sali'eres, A. L'Huillier, and M. Lewenstein, "Generalized phase-matching conditions for high harmonics: The role of field-gradient forces," *Physical Review A*, vol. 55, p. 3204, Apr. 1997.

[106] L. Chipperfield, P. Knight, J. Tisch, and J. Marangos, "Tracking individual electron trajectories in a high harmonic spectrum," *Optics Communications*, vol. 264, pp. 494–501, Aug. 2006.

[107] M. B. Gaarde, J. L. Tate, and K. J. Schafer, "Macroscopic aspects of attosecond pulse generation," *Journal of Physics B: Atomic, Molecular and Optical Physics*, vol. 41, no. 13, p. 132001, 2008.

[108] M. Murakami, J. Mauritsson, and M. B. Gaarde, "Frequency-chirp rates of harmonics driven by a few-cycle pulse," *Physical Review A*, vol. 72, no. 2, p. 023413, 2005.

[109] P. M. Paul, E. S. Toma, P. Breger, G. Mullot, F. Auge, P. Balcou, H. G. Muller, and P. Agostini, "Observation of a train of attosecond pulses from high harmonic generation," *Science*, vol. 292, no. 5522, p. 16891692, 2001.

[110] E. Goulielmakis, V. S. Yakovlev, A. L. Cavalieri, M. Uiberacker, V. Pervak, A. Apolonski, R. Kienberger, U. Kleineberg, and F. Krausz, "Attosecond control and measurement: Lightwave electronics," *Science*, vol. 317, pp. 769–775, Aug. 2007.

[111] P. B. Corkum, N. H. Burnett, and M. Y. Ivanov, "Subfemtosecond pulses," *Optics Letters*, vol. 19, pp. 1870–1872, Nov. 1994.

[112] G. Sansone, E. Benedetti, F. Calegari, C. Vozzi, L. Avaldi, R. Flammini, L. Poletto, P. Villoresi, C. Altucci, R. Velotta, S. Stagira, S. D. Silvestri, and M. Nisoli, "Isolated single-cycle attosecond pulses," *Science*, vol. 314, no. 5798, p. 443446, 2006.

[113] H. Mashiko, S. Gilbertson, C. Li, S. D. Khan, M. M. Shakya, E. Moon, and Z. Chang, "Double optical gating of High-Order harmonic generation with Carrier-Envelope phase stabilized lasers," *Physical Review Letters*, vol. 100, p. 103906, Mar. 2008.

[114] X. Feng, S. Gilbertson, H. Mashiko, H. Wang, S. D. Khan, M. Chini, Y. Wu, K. Zhao, and Z. Chang, "Generation of isolated attosecond pulses with 20 to 28 femtosecond lasers," *Physical Review Letters*, vol. 103, p. 183901, Oct. 2009.

[115] M. Drescher, M. Hentschel, R. Kienberger, G. Tempea, C. Spielmann, G. A. Reider, P. B. Corkum, and F. Krausz, "X-ray pulses approaching the attosecond frontier," *Science*, vol. 291, pp. 1923–1927, Mar. 2001.

[116] R. López-Martens, K. Varj, P. Johnsson, J. Mauritsson, Y. Mairesse, P. Salires, M. B. Gaarde, K. J. Schafer, A. Persson, S. Svanberg, C. Wahlstrm, and A. L'Huillier, "Amplitude and phase control of attosecond light pulses," *Physical Review Letters*, vol. 94, p. 033001, Jan. 2005.

[117] J. Itatani, F. F. Quéré, G. L. Yudin, M. Y. Ivanov, F. Krausz, and P. B. Corkum, "Attosecond streak camera," *Physical Review Letters*, vol. 88, p. 173903, Apr. 2002. Copyright (C) 2010 The American Physical Society; Please report any problems to prola@aps.org.

[118] F. Quéré, Y. Mairesse, and J. Itatani, "Temporal characterization of attosecond XUV fields," *Journal of Modern Optics*, vol. 52, no. 2, pp. 339 – 360, 2005.

[119] Y. Mairesse, A. de Bohan, L. J. Frasinski, H. Merdji, L. C. Dinu, P. Monchicourt, P. Breger, M. Kovacev, R. Taieb, B. Carre, H. G. Muller, P. Agostini, and P. Salieres, "Attosecond synchronization of high-harmonic soft x-rays," *Science*, vol. 302, p. 15401543, Nov. 2003.

[120] E. S. Toma and H. G. Muller, "Calculation of matrix elements for mixed extreme-ultraviolet-infrared two-photon above-threshold ionization of argon," *Journal of Physics B: Atomic, Molecular and Optical Physics*, vol. 35, no. 16, pp. 3435–3442, 2002.

[121] D. J. Bradley, A. J. F. Durrant, F. O'Neill, and B. Sutherland, "Picosecond pulses from mode-locked dye lasers," *Physics Letters A*, vol. 30, pp. 535–536, Dec. 1969.

[122] S. Gilbertson, Y. Wu, S. D. Khan, M. Chini, K. Zhao, X. Feng, and Z. Chang, "Isolated attosecond pulse generation using multicycle pulses directly from a laser amplifier," *Physical Review A*, vol. 81, p. 043810, Apr. 2010.

[123] A. Poppe, R. Holzwarth, A. Apolonski, G. Tempea, C. Spielmann, T. Hnsch, and F. Krausz, "Few-cycle optical waveform synthesis," *Applied Physics B: Lasers and Optics*, vol. 72, pp. 373–376, Feb. 2001.

[124] B. Proctor and F. Wise, "Quartz prism sequence for reduction of cubic phase in a mode-locked Ti:Al2O3 laser," *Optics Letters*, vol. 17, no. 18, pp. 1295–1297, 1992.

[125] F. Helbing, G. Steinmeyer, J. Stenger, H. Telle, and U. Keller, "Carrier-envelope-offset dynamics and stabilization of femtosecond pulses," *Applied Physics B: Lasers and Optics*, vol. 74, no. 9, pp. s35–s42, 2002.

[126] S. A. Planas, N. L. P. Mansur, C. H. B. Cruz, and H. L. Fragnito, "Spectral narrowing in the propagation of chirped pulses in single-mode fibers," *Optics Letters*, vol. 18, pp. 699–701, May 1993.

[127] A. L. Cavalieri, E. Goulielmakis, B. Horvath, W. Helml, M. Schultze, M. Fie, V. Pervak, L. Veisz, V. S. Yakovlev, M. Uiberacker, A. Apolonski, F. Krausz, and R. Kienberger, "Intense 1.5-cycle near infrared laser waveforms and their use for the generation of ultra-broadband soft-x-ray harmonic continua," *New Journal of Physics*, vol. 9, no. 7, pp. 242–242, 2007.

[128] F. Verluise, V. Laude, Z. Cheng, C. Spielmann, and P. Tournois, "Amplitude and phase control of ultrashort pulses by use of an acousto-optic programmable dispersive filter: pulse compression and shaping," *Optics Letters*, vol. 25, pp. 575–577, Apr. 2000.

[129] A. Baltuska, M. Uiberacker, E. Goulielmakis, R. Kienberger, V. Yakovlev, T. Udem, T. Hansch, and F. Krausz, "Phase-controlled amplification of few-cycle laser pulses," *Selected Topics in Quantum Electronics, IEEE Journal of*, vol. 9, no. 4, pp. 972–989, 2003.

[130] G. Steinmeyer, "New approaches to the generation and characterization of few-cycle laser pulses," *Habilitational, Inst. Quantum Electronics, Ultrafast Laser Physics, ETH Z*
"urich, Z
"urich, Switzerland, 2001.

[131] S. Bohman, A. Suda, T. Kanai, S. Yamaguchi, and K. Midorikawa, "Generation of 5.0 fs, 5.0 mJ pulses at 1?kHz using hollow-fiber pulse compression," *Optics Letters*, vol. 35, pp. 1887–1889, June 2010.

[132] S. Sartania, Z. Cheng, M. Lenzner, G. Tempea, C. Spielmann, F. Krausz, and K. Ferencz, "Generation of 0.1-TW 5-fs optical pulses at a 1-kHz repetition rate," *Optics Letters*, vol. 22, pp. 1562–1564, Oct. 1997.

[133] A. Suda, M. Hatayama, K. Nagasaka, and K. Midorikawa, "Generation of sub-10-fs, 5-mJ-optical pulses using a hollow fiber with a pressure gradient," *Applied Physics Letters*, vol. 86, no. 11, p. 111116, 2005.

[134] M. Nurhuda, A. Suda, K. Midorikawa, and H. Budiono, "Control of self-phase modulation and plasma-induced blueshifting of high-energy, ultrashort laser pulses in an argon-filled hollow fiber using conjugate pressure-gradient method," *Journal of the Optical Society of America B*, vol. 22, no. 8, pp. 1757–1762, 2005.

[135] X. Chen, A. Jullien, A. Malvache, L. Canova, A. Borot, A. Trisorio, C. G. Durfee, and R. Lopez-Martens, "Generation of 4.3 fs, 1 mJ laser pulses via compression of circularly polarized pulses in a gas-filled hollow-core fiber," *Optics Letters*, vol. 34, pp. 1588–1590, May 2009.

[136] C. Dorrer, E. Kosik, and I. Walmsley, "Spatio-temporal characterization of the electric field of ultrashort optical pulses using two-dimensional shearing interferometry," *Applied Physics B: Lasers and Optics*, vol. 74, no. 9, pp. s209–s217, 2002.

[137] E. M. Kosik, A. S. Radunsky, I. A. Walmsley, and C. Dorrer, "Interferometric technique for measuring broadband ultrashort pulsesat the sampling limit," *Optics Letters*, vol. 30, pp. 326–328, Feb. 2005.

[138] D. R. Austin, T. Witting, and I. A. Walmsley, "Broadband astigmatism-free Czerny-Turner imaging spectrometer using spherical mirrors," *Applied Optics*, vol. 48, pp. 3846–3853, July 2009.

[139] M. Schultze, E. Goulielmakis, M. Uiberacker, M. Hofstetter, J. Kim, D. Kim, F. Krausz, and U. Kleineberg, "Powerful 170-attosecond XUV pulses generated with few-cycle laser pulses and broadband multilayer optics," *New Journal of Physics*, vol. 9, no. 7, pp. 243–243, 2007.

[140] M. J. Abel, T. Pfeifer, P. M. Nagel, W. Boutu, M. J. Bell, C. P. Steiner, D. M. Neumark, and S. R. Leone, "Isolated attosecond pulses from ionization gating of high-harmonic emission," *Chemical Physics*, vol. 366, pp. 9–14, Dec. 2009.

[141] T. Pfeifer, M. J. Abel, P. M. Nagel, W. Boutu, M. J. Bell, Y. Liu, D. M. Neumark, and S. R. Leone, "Measurement and optimization of isolated attosecond pulse contrast," *Optics Letters*, vol. 34, pp. 1819–1821, June 2009.

[142] S. Gilbertson, X. Feng, S. Khan, M. Chini, H. Wang, H. Mashiko, and Z. Chang, "Direct measurement of an electric field in femtosecond Bessel-Gaussian beams," *Optics Letters*, vol. 34, no. 16, pp. 2390–2392, 2009.

[143] S. Gilbertson, S. D. Khan, Y. Wu, M. Chini, and Z. Chang, "Isolated attosecond pulse generation without the need to stabilize the Carrier-Envelope phase of driving lasers," *Physical Review Letters*, vol. 105, no. 9, p. 093902, 2010.

[144] C. Arrell, *Generation of few-cycle and attosecond pulses and their use in probing ultrafast dynamics in gases and surfaces.* PhD thesis, Imperial College London, Sept. 2010.

[145] T. Kita, T. Harada, N. Nakano, and H. Kuroda, "Mechanically ruled aberration-corrected concave gratings for a flat-field grazing-incidence spectrograph," *Applied Optics*, vol. 22, pp. 512–513, Feb. 1983.

[146] J. L. Wiza, "Microchannel plate detectors," *NUCL. INSTRUM. METHODS*, vol. 162, pp. 60—1, 1979.

[147] B. L. Henke, E. M. Gullikson, and J. C. Davis, "X-Ray interactions: Photoabsorption, scattering, transmission, and reflection at e = 50-30,000 eV, z = 1-92," *Atomic Data and Nuclear Data Tables*, vol. 54, pp. 181–342, July 1993.

[148] O. Hemmers, S. B. Whitfield, P. Glans, H. Wang, D. W. Lindle, R. Wehlitz, and I. A. Sellin, "High-resolution electron time-of-flight apparatus for the soft x-ray region," *Review of Scientific Instruments*, vol. 69, no. 11, p. 3809, 1998.

[149] E. Goulielmakis, M. Schultze, M. Hofstetter, V. S. Yakovlev, J. Gagnon, M. Uiberacker, A. L. Aquila, E. M. Gullikson, D. T. Attwood, R. Kienberger, F. Krausz, and U. Kleineberg, "Supporting online material for: Single-Cycle nonlinear optics," *Science*, vol. 320, pp. 1614–1617, June 2008.

[150] D. J. Kennedy and S. T. Manson, "Photoionization of the noble gases: Cross sections and angular distributions," *Physical Review A*, vol. 5, p. 227, Jan. 1972.

[151] D. J. Kane, G. Rodriguez, A. J. Taylor, and T. S. Clement, "Simultaneous measurement of two ultrashort laser pulses from a single spectrogram in a single shot," *Journal of the Optical Society of America B*, vol. 14, pp. 935–943, Apr. 1997.

[152] Z. Wang, E. Zeek, R. Trebino, and P. Kvam, "Determining error bars in measurements of ultrashort laser pulses," *Journal of the Optical Society of America B*, vol. 20, pp. 2400–2405, Nov. 2003.

[153] M. D. Perry and J. K. Crane, "High-order harmonic emission from mixed fields," *Physical Review A*, vol. 48, p. R4051, Dec. 1993.

[154] J. Mauritsson, P. Johnsson, E. Gustafsson, A. L'Huillier, K. J. Schafer, and M. B. Gaarde, "Attosecond pulse trains generated using two color laser fields," *Physical Review Letters*, vol. 97, pp. 013001–4, July 2006.

[155] E. Mansten, J. M. Dahlström, P. Johnsson, M. Swoboda, A. L'Huillier, and J. Mauritsson, "Spectral shaping of attosecond pulses using two-colour laser fields," *New Journal of Physics*, vol. 10, no. 8, p. 083041, 2008.

[156] Y. Zheng, Z. Zeng, P. Zou, L. Zhang, X. Li, P. Liu, R. Li, and Z. Xu, "Dynamic chirp control and pulse compression for attosecond High-Order harmonic emission," *Physical Review Letters*, vol. 103, p. 043904, July 2009.

[157] D. Shafir, Y. Mairesse, D. M. Villeneuve, P. B. Corkum, and N. Dudovich, "Atomic wavefunctions probed through strong-field light-matter interaction," *Nat Phys*, vol. 5, pp. 412–416, June 2009.

[158] H. Niikura, N. Dudovich, D. M. Villeneuve, and P. B. Corkum, "Mapping molecular orbital symmetry on High-Order harmonic generation spectrum using Two-Color laser fields," *Physical Review Letters*, vol. 105, p. 053003, July 2010.

[159] T. T. Liu, T. Kanai, T. Sekikawa, and S. Watanabe, "Significant enhancement of high-order harmonics below 10nm in a two-color laser field," *Physical Review A*, vol. 73, p. 063823, June 2006.

[160] I. J. Kim, G. H. Lee, S. B. Park, Y. S. Lee, T. K. Kim, C. H. Nam, T. Mocek, and K. Jakubczak, "Generation of submicrojoule high harmonics using a long gas jet in a two-color laser field," *Applied Physics Letters*, vol. 92, no. 2, p. 021125, 2008.

[161] H. Du, H. Wang, and B. Hu, "Isolated short attosecond pulse generated using a two-color laser and a high-order pulse," *Physical Review A*, vol. 81, p. 063813, June 2010.

[162] V. Le, A. Le, R. Xie, and C. D. Lin, "Theoretical analysis of dynamic chemical imaging with lasers using high-order harmonic generation," *Physical Review A*, vol. 76, p. 013414, July 2007.

[163] J. Itatani, J. Levesque, D. Zeidler, H. Niikura, H. Pepin, J. C. Kieffer, P. B. Corkum, and D. M. Villeneuve, "Tomographic imaging of molecular orbitals," *Nature*, vol. 432, no. 7019, p. 867–871, 2004.

[164] B. Shan and Z. Chang, "Dramatic extension of the high-order harmonic cutoff by using a long-wavelength driving field," *Physical Review A*, vol. 65, p. 011804, Dec. 2001.

[165] J. Tate, T. Auguste, H. G. Muller, P. Salières, P. Agostini, and L. F. DiMauro, "Scaling of Wave-Packet dynamics in an intense midinfrared field," *Physical Review Letters*, vol. 98, p. 013901, Jan. 2007.

[166] K. Schiessl, K. L. Ishikawa, E. Persson, and J. Burgdörfer, "Quantum path interference in the wavelength dependence of High-Harmonic generation," *Physical Review Letters*, vol. 99, p. 253903, Dec. 2007.

[167] M. V. Frolov, N. L. Manakov, and A. F. Starace, "Wavelength scaling of High-Harmonic yield: Threshold phenomena and bound state symmetry dependence," *Physical Review Letters*, vol. 100, p. 173001, May 2008.

[168] A. D. Shiner, C. Trallero-Herrero, N. Kajumba, H. Bandulet, D. Comtois, F. Légaré, M. Giguère, J. Kieffer, P. B. Corkum, and D. M. Villeneuve, "Wavelength scaling of high harmonic generation efficiency," *Physical Review Letters*, vol. 103, no. 7, p. 073902, 2009.

[169] D. B. Milosevic and W. Becker, "Role of long quantum orbits in high-order harmonic generation," *Physical Review A*, vol. 66, p. 063417, Dec. 2002.